# Temperature and Density Measurements at an Inductively RF Excited Hydrogen Plasma Discharge

Dissertation

submitted to the Fachbereich Physik der Universität Duisburg-Essen

in order to fulfil the requirements for the academic degree

doctor rerum naturalium (Dr. rer. nat.)

by

Mohammed Abdel-Rahman Abdel-Gaber Abdalla

born

on 26. June 1970

in El-Minia, Egypt

Day of insertion: 27. August 2004
First referee: Prof. Dr. H. F. Döbele
Second referee: Prof. Dr. V. Buck
Head of commision: Prof. Dr. L. Schäfer
Day of Promotion: 12. October 2004

Die vorliegende Arbeit entstand während meiner Tätigkeit als wissenschaftlicher Mitarbeiter der AG Prof. Dr. H. F. Döbele am Institut für Laser- und Plasmaphysik der Universität Duisburg-Essen.

To my father and my mother
To my wife and my kids

# Contents


**1 General introduction** **1**

1.1 Research areas of plasma . . . . . 1

1.1.1 Natural plasmas . . . . . 3

1.1.2 Technological plasmas . . . . . 3

1.2 Scope and overview of the present thesis . . . . . 5

**2 Concepts of RF-excited discharges** **9**

2.1 Introduction . . . . . 9

2.2 E-type or capacitively coupled RF-discharges . . . . . 11

2.2.1 Sheath formation in CCRF discharges . . . . . 12

2.3 H-type or inductively coupled RF-discharges . . . . . 14

2.3.1 Inductive sources geometries . . . . . 15

2.3.2 Electromagnetic theory of ICP discharges . . . . . 18

2.3.3 Heating mechanisms in inductively coupled plasma discharges 20

2.3.3.1 Joule (collisional) heating . . . . . 20

2.3.3.2 Collisionless heating . . . . . 21

**3 Diagnostic concepts of RF-excited discharges** **23**

3.1 An overview of different plasma diagnostic techniques . . . . . 23

3.1.1 Absorption spectroscopy . . . . . 23

3.1.2 Laser Thomson Scattering (LTS) . . . . . 25

3.2 The diagnostic methods applied . . . . . 26

3.2.1 Optical Emission Spectroscopy (OES) . . . . . 27

3.2.2 Interferometric method using Fabry-Perot Interferometer (FPI) 33

3.2.3 Langmuir Probe Diagnostics . . . . . 35

3.2.4 Two Photon Absorption Laser Induced Fluorescence (TALIF) 40

3.3 Spatial resolution based on Abel inversion . . . . . 43
3.3.1 Fourier method . . . . . 44

**4 Experimental set-up and implemented diagnostics 47**
4.1 Discharge chamber geometry . . . . . 47
4.2 Planar coil construction . . . . . 48
4.3 Power supply and coupling circuit . . . . . 49
4.4 Implemented diagnostics . . . . . 51
4.4.1 Optical Emission Spectroscopy Equipment . . . . . 51
4.4.2 Fabry-Perot Interferometer set-up . . . . . 53
4.4.3 The Smart Soft Langmuir Probe System . . . . . 54
4.4.4 TALIF set-up . . . . . 55

**5 Operation characteristics 57**
5.1 Introduction . . . . . 57
5.2 Transition from the capacitive to the inductive-mode . . . . . 57
5.3 Capacitive effects at high pressure . . . . . 64
5.4 Smart Probe measurements . . . . . 65
5.4.1 Electron density and temperature measurements . . . . . 66
5.4.2 Electron energy distribution function (EEDF) . . . . . 68
5.5 The hysteresis in the system . . . . . 69

**6 Measurements of properties of the neutrals 73**
6.1 Determination of Gas Temperature . . . . . 73
6.1.1 Gas temperature measurements based on rotational transition 74
6.1.1.1 Rotational temperatures determination from $3p\,^3\prod_u^- \rightarrow 2s\,^3\sum_g^+$ transitions of $H_2$ . . . . . 75
6.1.1.2 Time and axial dependencies of emission and rotational temperature . . . . . 78
6.1.1.3 Comparison with model . . . . . 82
6.1.1.4 Power and pressure dependencies on the rotational temperature . . . . . 87
6.1.2 Determination of the gas temperature by Fabry-Perot Interferometry . . . . . 88
6.1.3 Application to side-on measured Fulcher band intensities: 92

6.1.4 Radial gas temperature results . . . . . 92
6.2 Determination of the Degree of Dissociation . . . . . 96
6.2.1 Actinometry . . . . . 97
6.2.2 Direct actinometric method (classical method) . . . . . 98
6.2.3 Actinometry with consideration of dissociative excitation . 100
6.2.3.1 Probe method . . . . . 101
6.2.3.2 Advanced "two gas actinometry" . . . . . 102
6.2.4 Dissociation degree measurements . . . . . 106
6.2.5 Comparison with TALIF measurements . . . . . 114
6.2.6 Determination of electron temperature by OES . . . . . 116

**7 Summary and conclusions 121**

# Chapter 1

## General introduction

### 1.1 Research areas of plasma

Solids, liquids and gases are the first three states of matter. Plasmas are often referred to as the fourth state of matter. The word "plasma" was first used by Irving Langmuir in 1928 to describe the ionized gas in electric discharges. Plasma is by no means a human invention, it is the most abundant state in the universe. It is either a fully or partially ionized gas; the ionization degree can vary from 100% to very low values (e.g. $10^{-4}$ - $10^{-6}$) [1]. Plasmas emit light and contain complex mixtures of free electrons and heavy particles such as ions (positive or negative), neutral atoms and molecules, possibly found in excited electronic, vibrational, or rotational states. The plasma state is characterized by "quasi-neutrality" in which the negatively charged species density is well balanced by the density of the positively charged species.

According to equilibrium conditions plasmas can exist in local thermal equilibrium (LTE) in which the temperatures of all constituent species (electrons, ions, neutrals) are the same in localized areas in the plasma, such as in fusion experiments and in high pressure discharge plasmas. Plasmas can also exist in non-equilibrium states (non-LTE) such as in interstellar plasmas and low pressure discharge plasmas (with some exceptions). Of all charged particles present in non-equilibrium plasmas electrons with their characteristic parameters (density and temperature) play the most important role. As a result of their smaller mass compared to positive and negative ions they have much higher velocity and energy, hence much higher temperature $T_e$ than all other species in plasmas. Electrons

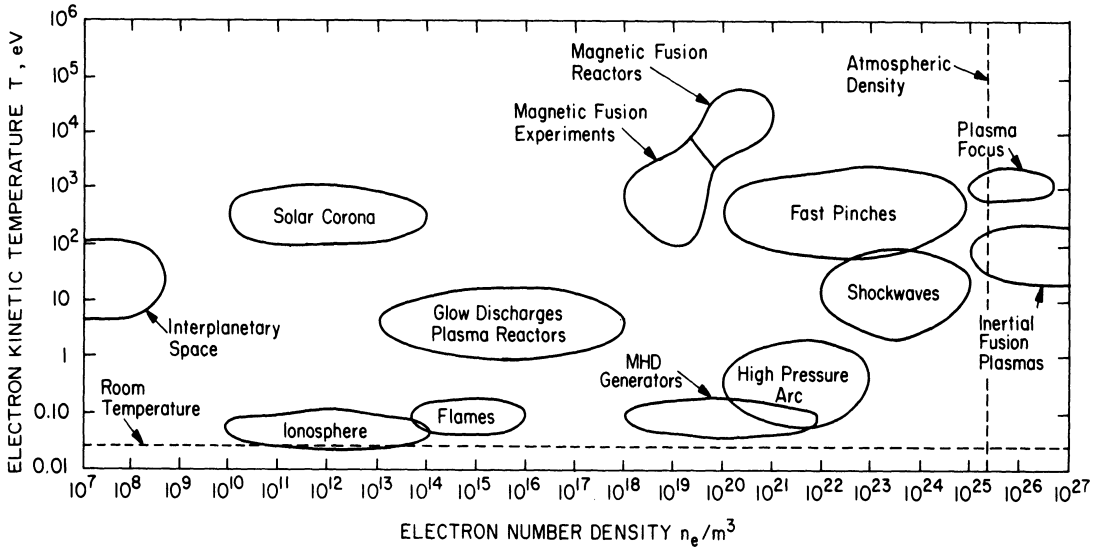


Figure 1.1: The dynamic range of $n_e$ and $T_e$ for typical plasmas.

loose their energy mainly in inelastic collisions, leading to excitation, dissociation and ionization. So the dissociation of feed gas molecules into radicals is mainly driven by the electrons which makes the electron energy distribution function a very important parameter in the discharge behaviour.

After this brief description of the plasma state and thermodynamic equilibrium and non-equilibrium conditions, we will concentrate now on the plasma research areas.

Plasmas are characterized by the electron density $n_e$ ($cm^{-3}$) and temperature $T_e$ (K or more conveniently eV). The dynamic range of $n_e$ and $T_e$ is shown in Fig. (1.1) [2]. In this graph several kinds of plasmas are indicated. Today different research areas for different plasmas are interesting. We can coarsely classify research areas of plasma into natural and technological (man-made) plasmas. Of natural plasmas, most of the visible matter created in our universe (more than 99%) is in the plasma state such as the sun and stars, interstellar gas, earth's ionosphere and magnetosphere, etc. [1]. Technological plasmas are driven by an externally applied power in order to sustain them.

### 1.1.1 Natural plasmas

Natural plasmas dominate research activities in the fields of space plasma physics and astrophysics. Space plasma physics studies the earth environment in space, this includes many different kinds of plasmas for example: solar winds, ionosphere, and Van Allen radiation belts. Astrophysics deals with the physics of stellar phenomena that are rich of plasmas under extreme conditions. Examples are, stellar interiors and interstellar medium. The goal of astrophysics or space physics laboratory experiments is to create a sample plasma similar to what would be found in the astronomical body, then to study its properties, radiation and thermodynamic state.

### 1.1.2 Technological plasmas

We can distinguish between two main groups of technical plasmas, i.e. high temperature plasmas (HTP) and low temperature plasmas (LTP) or gas discharges having different research topics.

**High temperature fusion-oriented plasma physics:** Fusion is the nuclear reaction that powers the sun and stars. In the core of the sun at temperatures of 10-15 million Kelvin, hydrogen is converted to helium providing enough energy to sustain life on earth. Laboratory fusion experiment research began in 1950 and was developed in order to yield a nuclear energy source on earth. Much of plasma physics research has been motivated by the goal of controlled thermonuclear fusion energy. The plasmas produced to create controlled thermonuclear fusion are LTE plasmas with very energetic heavy particles [3]. In order to achieve the deuterium and tritium fusion reaction (power out $\gg$ power in ), very high temperatures (over 100 million deg. K) and high density plasma (over $2 \times 10^{20}\ m^{-3}$) are required for a long enough time. In some fusion energy experiments, magnetic fields are used to confine the hot plasma. The fusion program has ongoing negotiations to build the International Thermonuclear Experimental Reactor (ITER) in a major collaboration involving the USA, the European Union, Canada and Japan. A wide range of physics research topics on ITER are possible, for example: plasma heating systems, plasma-wall interaction and development of both the fusion materials and the diagnostics.

**Low-temperature material science oriented plasma physics:** Two kinds of gas discharges or low-temperature plasmas (LTP) can be distinguished: the thermal plasma in which the gas temperature is the same as for the electrons and ions ($T_g \approx T_i \approx T_e \lesssim 2\times10^4 K$) [4]. This kind of plasma is in local thermodynamic equilibrium. Examples are electric arcs and plasma jets operating at atmospheric pressures [3]. Research on such kind of plasma focuses on applications such as cutting and welding, where heat is required. Moreover, another important research application branch is using this thermal plasma as a light source in the form of electroded and electrodeless high pressure, high-intensity discharge (HID) lamps. Non-thermal or cold plasma is the second type of low-temperature plasmas. These plasmas are far from local thermodynamic equilibrium (non-LTE), since the ions have energies corresponding to a gas at room temperature (300 K) and the electrons have energies of a few (1-10) eV ($T_g \approx T_i \ll T_e \lesssim 10^5 K$) [4]. Cold plasma (non-LTE) exists in case of low-pressure glow discharges. Examples of low temperature low pressure glow discharges are: the direct current (d.c) glow discharges, capacitively coupled radio frequency (CCRF) discharges, low pressure high density plasmas such as electron cyclotron resonance sources (ECRs), helicon sources, helical resonator sources and the inductively coupled plasma sources (ICPs). Cold plasmas serve as highly reactive tools for powerful but gentle applications without dissipation of great amounts of energy. This covers a broad range of research topics such as light sources and car industry, since cold plasma can be used, directly, or indirectly during the manufacturing.

Today, material science oriented plasma physics represents the most important research area of cold plasma. In materials processing cold plasmas are generally used, although high density is beneficial for increasing process speed. Material science oriented plasma physics covers different research topics including the deposition of thin films, the production of coatings with optical properties and in flat panel display fabrication. Using cold plasma in the case of plasma display panels (PDPs) and liquid crystal (LC) technology is an important industrial research field of rapidly increasing importance. In semiconductor processing (e.g. producing a modern PC processor chip), the plasma processes used to manufacture semiconductor devices consist of four main areas, namely deposition, etching, masking, and stripping to form and connect circuit elements like transistors and capacitors. The largest research areas of these are deposition and reactive etch pro-

cesses. Plasma based deposition processes are subdivided into sputter-deposition and Plasma Enhanced-Chemical Vapor Deposition (PE-CVD)[1]. Plasma etching is an important research topic, focusing essentially on removing material from a surface.

## 1.2 Scope and overview of the present thesis

Inductively and capacitively coupled plasma RF-discharges are the two main types of plasma system used commercially for surface modification, fabrication of modern integrated circuit (IC) devices and thin film deposition [5, 6]. The requirements for the fabrication of semiconductor devices with critical dimensions $< 0.25\,\mu m$ will require plasma processing tools delivering high plasma densities and controllable ion energy distribution at low pressures, which limits the use of such E-type (CCRF) discharges. Electrodeless plasmas (ICP), that can provide high electron density at low neutral pressure, are particularly attractive in the domain of plasma processing [7]. Hydrogen (and its isotopes deuterium and tritium) is the simplest element of the periodic table with one electron. Hydrogen discharges (the simplest electronegative gas discharges) are widely used in many technological plasma processes [8]. Two intensely developed applications of hydrogen (H) plasma in material treatments are reduction of oxides on surfaces and deposition of thin films where mixtures very rich in $H_2$ are used. Oxidized surfaces of metals become metallic upon exposure to atomic H or H plasma at appropriate pressure and temperature. Diamond thin films are synthesized by chemical vapour deposition (CVD) or hot-filament techniques using a few percent of hydrocarbons mixed into a flow of H gas over a substrate at the temperature around $800^oC$ [9]. Pure hydrogen plasmas are used in microelectronics for surface cleaning of GaAs [10]. These are the reasons for choosing the inductively coupled hydrogen plasma discharge the research topic of this Ph.D.

Homogeneity, controllable temperature and a high degree of dissociation are requirements of industrial applications. All of these parameters can in principle be investigated by some kind of lasers such as vacuum-ultraviolet (VUV) and Two photon Absorption Laser Induced Fluorescence (TALIF). Lasers, as a result of their complicated systems and costs, are not preferred by companies. Optical emission spectroscopy (OES) has proven to be an accurate and powerful tool, in addition OES has the advantageous other than laser of using 'less equipments'

and it is a much 'less complicated' method. *Can we improve and validate the applicability of OES to investigate such plasma parameters in an inductively coupled plasma (ICP) discharge?* This is the physical question and the reason for choosing diagnostic by OES. We answer this by checking of important plasma parameters such as gas temperature and the degree of dissociation which determine the applicability of the plasma itself. Gas temperature measurements are obtained by measuring both of rotational and translational temperature. Spatially resolved measurements are also performed in order to answer the question of homogeneity. A new advanced actinometric OES scheme in addition to the classical one is used for determination of the degree of dissociation. The basic problem of OES is that only excited species in plasma can be detected, i.e. the measured emission radiation only gives information about the excited state density and does not directly reflect the ground state population. To extract the required information ($n_e, T_e$, gas temperature, etc.) out of emission measurements, this problem can be solved by models based on atomic and molecular data [11].

This thesis is a diagnostic study of an inductively coupled hydrogen plasma (ICP) discharge working at 13.56 MHz. In addition to the OES diagnostic technique, other diagnostic methods are used during this work to get a complete description of the plasma. In principle the experimental work of the thesis is focused on three main points, firstly the transition characteristics of the inductively coupled discharge. Then the thesis describes in detail the determination of phase and space resolved gas temperature and the degree of dissociation. The thesis is ordered as follows:

After the general introduction, describing gas discharges and applications of low temperature plasma physics with some special consideration for inductive discharges in hydrogen.

**Chapter 2** provides background information about RF-discharges with some details of the inductively coupled type used during this work.

**Chapter 3** presents an overview of different diagnostic techniques and more detailed information about the applied diagnostic ones including Langmuir Probe (LP) diagnostics, Optical Emission Spectroscopy (OES), Fabry Perot Interferometric (FPI) technique, in addition a brief survey about the Two-photon Absorption Laser induced Fluorescence (TALIF) technique.

**Chapter 4** discusses the experimental setup with the implemented diagnostics.

**Chapter 5** comprises the description and discussion of the emission characteristics of our discharge. This chapter focuses on the transition characteristics between different modes of operation of the ICP discharge by the optical emission spectroscopy (OES) measurements, taking into account some probe results.

**Chapter 6** screens the central topic of this thesis, which is the determination of important plasma parameters. This chapter is subdivided into two main parts closely related to each other. The first part deals with the determination of the time and space resolved rotational temperature using Fulcher band. Whether this rotational temperature really reflects the gas temperature or not is a fundamental question. To solve this problem, Fabry Perot Interferometer (FPI) measurements of the translational temperature are compared. In addition, radially resolved rotational temperature measurements are achieved to test the homogeneity of the discharge. The results of time and space resolved rotational temperature measurements obtained are used as input parameters in the second part of this chapter in order to determine the degree of dissociation. The degree of dissociation is determined by the classical actinometric OES method and by a new advanced actinometric method called "two gas actinometry". Furthermore, the influences of the electron energy distribution function measured by the probe are used as another method for the determination of the degree of dissociation. A comparison measurement of the degree of dissociation by a Laser Induced Fluorescence (LIF) technique is presented. The electron temperature has been determined by comparing both actinometer lines of the advanced "two gas actinometry" method.

**Chapter 7** presents the summary and the conclusions of this work, and finally an outlook for future research.

# Chapter 2

## Concepts of RF-excited discharges

### 2.1 Introduction

Depending on the way power is coupled into the plasma, various kinds of discharges can be distinguished: direct current (DC) glow discharges, electron cyclotron resonance (ECR), microwave discharges operating in the GHz frequency range and radio frequency (RF) discharges, etc. RF discharges are one form of the nonlinear interaction of an electromagnetic field and a bounded plasma, with this interaction the parameters of the plasma itself are determined by the parameters of the external electromagnetic field. RF discharges are of increasing interest for technical and industrial applications. An important aspect of RF-discharges is that they are far from thermodynamic equilibrium. In such kind of non-equilibrium plasma the electron temperature does not equal the ion temperature, which can differ by two orders of magnitude (typically $T_e$= 2-5 eV and $T_i < 0.05$ eV). Perhaps the most notable feature of the plasma glow region is its ability to maintain a state of quasi-neutrality in which the net charge density is zero since:

$$n_e \simeq n_i \tag{2.1}$$

where $e$ and $i$ are referred to electron and ion respectively.

RF discharges usually operate in the frequency range from one to hundreds of Megahertz, $f = \frac{\omega}{2\pi} \cong 1 - 100MHz$. The corresponding wavelengths ($\lambda$ = 3-300 m) are large compared to the dimensions of the plasma reactor [4]. The commonly used frequencies in RF plasma reactors are 13.56 MHz and its higher harmonics

of 27.12 MHz and 40.68 MHz. These frequencies are allowed by international communications authorities [12]. Under RF conditions, plasma electrons respond in general to the instantaneous electromagnetic fields, whereas massive ions respond to the time averaged fields. The frequencies at 1 GHz and above correspond to the microwave range. The most commonly used frequency, in microwave discharges, is 2.45 GHz. These discharges are maintained by electromagnetic waves and normally used to obtain dense equilibrium plasmas at comparatively high (near atmospheric) gas pressures.

Since this thesis is concerning with RF discharges at 13.56 MHz, these discharges and their physical features will be considered in more detail. RF plasma discharges have the following characteristics [13]:

1. They are weakly ionized plasmas with a degree of ionization of the order of $10^{-4}$.

2. Charged particles usually interact weakly with each other.

3. Ionization of neutrals sustain the plasma in steady state as a result of collisions with electrons.

4. Heavy ions exchange energy by collisions with the background gas effectively.

5. Electrons are not in thermal equilibrium with ions.

The RF power absorption $P_{abs}$ per unit volume by a plasma is related to the amplitude of the electromagnetic field $E_0$ by the relation [3, 14]:

$$P_{abs} = \frac{n_e e^2}{2m_e \nu}\left(\frac{\nu^2}{\nu^2 + \omega^2}\right)E_0^2 \tag{2.2}$$

Where $n_e$ is the electron density, $e$ and $m_e$ are the electron charge and mass, $\nu$ is the electron-neutral collision frequency, $\omega$ refers to the angular frequency of the electromagnetic field.

The power coupling in RF discharges can be accomplished capacitively via the electric field, producing so called E-type or capacitively coupled RF (CCRF) discharge. This power can also be inductively coupled via the magnetic field, producing H-type or inductively coupled plasma (ICP) discharges.

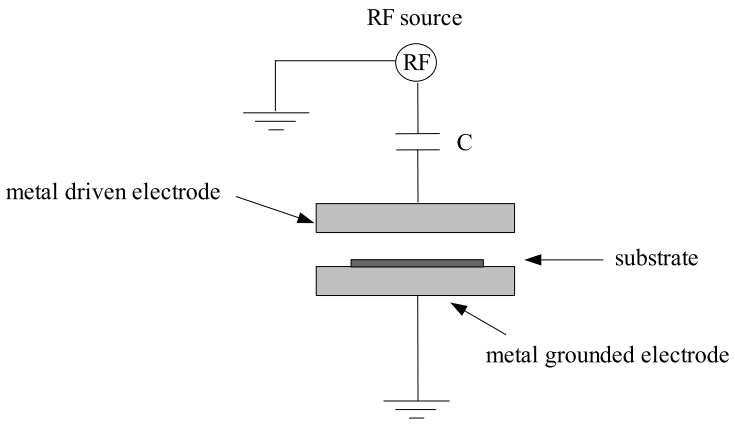


Figure 2.1: RF-discharges in the capacitively coupled type

## 2.2 E-type or capacitively coupled RF-discharges

E-type or capacitively coupled (CCRF) discharges, sometimes called diode discharges, are commonly used for materials processing. In these devices the coupling is generated between interior disc-shaped electrodes, built into the vacuum vessel [7, 14, 15]. These electrodes can be immersed directly into the plasma or separated from it by dielectric layers and they are separated by a small gap into which the gas is introduced. Normally one of these electrodes is driven by a high frequency RF voltage while the other one is grounded as shown in Fig. (2.1). The plasma is generated and maintained by an electric field that results from applying this RF voltage between these two electrodes. The typical RF driving voltage is $V_{RF} \approx 100 - 1000\,V$ operated at frequency of 13.56 MHz and the electrode separation is d $\approx 2 - 10$ cm. When considering CCRF plasmas, it is convenient to divide the system into two separate regions, the "bulk" plasma and the "sheath". It is reasonable to do this, since the physics occurring in these two regions is very different. The space between electrodes is filled with "bulk" plasma, which is separated from the electrodes by the "sheath" regions covering both electrodes. Typical discharge parameters are the pressure is within the range of 1-100 Pa, and the plasma density of the order of $10^9 - 10^{11} cm^{-3}$ [1]. As a result of the pronounced behavior of the sheath in CCRF discharges, it will be useful to mention it here in some detail.

### 2.2.1 Sheath formation in CCRF discharges

Before going into details of the description of the sheath we have to deal with two characteristic lengths of plasma physics called the Debye length and the mean free path, since the sheath thickness depends on these lengths. As mentioned in chapter 1, the plasma is characterized by its electron density $n_e$ $(m^{-3})$ and electron temperature $T_e$ (K or eV). Debye was the first to point out that the field of any charge imbalance is shielded, so that its influence is effectively restricted or screened within a finite range called the Debye shielding length, which is given by [7]:

$$\lambda_D\,(cm) = \sqrt{\frac{\varepsilon_0 k_B T_e}{e^2 n_e}} \tag{2.3}$$

where $\varepsilon_0$ is the permittivity of free space, $k_B$ refers to Boltzmann constant and $e$ is the electron charge.

The Debye length is a measure of the penetration depth of external electrostatic fields within the plasma, i.e. the thickness of the boundary sheath over which charge neutrality may not be obtained. The strong electrostatic fields which drive the electrons in order to re-establish neutrality cause oscillations about the equilibrium position at a characteristic frequency, the so-called electron plasma frequency $\omega_{pe}$. This frequency provides the fundamental time-scale in plasma physics. It may be expressed as [7]:

$$\omega_{pe} = \frac{\sqrt{k_B T_e / m_e}}{\lambda_D} = \sqrt{\frac{e^2 n_e}{\varepsilon_0 m_e}} \tag{2.4}$$

where $\sqrt{k_B T_e / m_e}$ is the electron thermal speed.

Clearly, there is a different plasma frequency for each species. However, the electron plasma frequency is the most important, and is generally referred to as the plasma frequency. Electromagnetic radiation of frequencies $\omega < \omega_{pe}$ are reflected, since these frequencies are prevented from penetrating the plasma by the more rapid electron response which neutralizes the field. Therefore, the electron density corresponding to the electron plasma frequency is called the "cut-off density" [14].

The mean free path $\lambda_{mfp}$ is another characteristic length related to elastic or inelastic collisions obtained in the sheath and it is defined as the average distance a particle moves without encountering collisions. In low pressure inductively cou-

pled plasmas, the collisional processes which are the most likely to happen are: electron-neutral collisions, ion-neutral collisions and neutral-neutral collisions.

**Capacitive RF sheath:** All surfaces in contact with the plasma are surrounded by a comparatively dark space sheath region which may be a few $\mu m$ to a few mm in size depending upon the plasma conditions (except in hydrogen discharge, as a result of the field reversal region near the powered electrode [16]). Consider an insulated surface is placed in contact with the plasma, the surface will initially be struck by positive ions and electrons when applying RF power. The flux of each species will be unequal because of the large $M_+/m_e$ ratio. Electrons will travel with much higher velocity in the plasma than the ions which can be considered to a first approximation as stationary. The surface will charge up negatively with respect to the plasma and it will acquire a potential called the "floating potential" $V_f$, which is lower than the potential of the quasi-neutral plasma potential $V_p$. The resulting depletion of electrons from the quasi-neutral plasma in the vicinity of the object leaves a space-charge or sheath region of ions, which sets up an electric field to further repel most of the electrons from leaving the plasma. The field, which blocks electrons from leaving the plasma, accelerates some of the slowly moving ions from the plasma to the surface. Since the sheath is a region over which a negative potential is dropped, electrons are rapidly expelled from the sheath. There is an apparent significant difference in electron density in plasma and sheath, the sheath is a region of effectively zero electron density, i.e. it contains only positive ions [17]. This loss of electron density results in a reduction of electron impact excitation reactions in that region. Since such reactions lead to fluorescent emission from excited species, the sheath region does not glow as much as the plasma bulk.

When an electrically biased element, such as a Langmuir probe, is introduced into the plasma, a positively charged (ion) sheath develops around a negatively biased probe, whereas a negatively charged (electron) sheath develops around a positively biased probe. The thickness of these sheaths depends on the Debye length. The Child-Langmuir law governs the relation between the Debye length $\lambda_D$ and the sheath width $l_s$ for a plane surface as [7]:

$$l_s = \lambda_D (\frac{eV_s}{k_B T_e})^{3/4} \tag{2.5}$$

where $V_s$ represents the potential drop across the sheath.

Both the Debye length and the mean free path are important to understand the concept of the sheath. Before the sheath, just in front of the sheath edge, there must be a region called the "presheath". In the presheath the ions begin to be accelerated toward the electrode, but the ion velocities are still low enough, so that the quasi-neutrality ($n_e \simeq n_i$) is still maintained. The physical dimension of the presheath is determined by such processes as electron-ion collisions, ion-neutral collisions, and geometric factors [18]. As the ions are accelerated, the ion density must decrease and, due to quasi-neutrality, the electron density also decreases, which results a decrease in the observed optical emission [19].

The nature of the sheath changes according to the coupling of the RF power into the discharge as follows: The powered electrode in case of CCRF discharges is capacitively coupled to a generator which provides a potential. This potential oscillates sinusoidally on an RF time scale. There are direct field lines between the RF powered electrode and the plasma, the distinguishing feature of CCRF discharges is the presence of RF- modulating or oscillating sheaths near electrodes, where the displacement current dominates conduction current. The electrons may undergo more "collisions" with the expanding and contracting sheaths in front of the electrodes than with neutral atoms or molecules. The powered electrode sheath potential can be very large (several hundred V).

## 2.3 H-type or inductively coupled RF-discharges

Inductively coupled RF-discharges were first investigated about a century ago [7]. ICP discharges can provide high density plasma ($> 10^{11} cm^{-3}$) of good uniformity in a low pressure gas ($< 10$ Pa) without the need for additional external magnetic fields [13, 19, 20, 21]. The ICP configuration usually consists of a chamber with a conducting external coil which can appear in different configurations (cylindrical or plane coil). Radio frequency (RF) power is applied to the coil and induces electric fields that partially ionize the gas inside the chamber and sustain the discharge.

The electric field is generated by a transformer of RF current from an external RF generator through the non-resonant, inductive coil (of one or a few turns) placed adjacent to the plasma region. The current-carrying coil or wire can either be outside or inside the plasma volume and is commonly driven at the industrial

frequency [22] f = 13.56 MHz using a RF power supply (output impedance 50 W) through a capacitive matching network. Typically, a dielectric window made of glass or ceramic separates the plasma and excitation coil. The most common window materials are quartz ($SiO_2$) and alumina ceramic ($Al_2O_3$).

The plasma created in ICP discharges has several advantages [13, 21, 23, 24]:

1. Simplicity and absence of contamination by electrode material.
2. The inductive power transfer and lack of electrodes leads to low voltage drop across all plasma sheaths and wall surface.
3. High density plasma at lower pressures.
4. Efficient use of power and long life time using reactive gases.

There is capacitively coupled RF field flowing between the coil and the plasma. An advantage of this field is to initiate the discharge and provide sufficient plasma density for inductive coupling. Capacitive coupling between the ICP source and the plasma reduces the conduction current of the coil along its length, which can be reduced by increasing the gap between the coil and the dielectric window, or by increasing the dielectric window thickness [25]. An electrostatic shield called "Faraday shielding" is sometimes placed between the coil and the plasma. It reduces this capacitive coupling, since the capacitive fields are short-circuited by the shield, while the inductive fields can penetrate. The way to use such Faraday shielding for decreasing capacitive effects in inductive discharges is not free from serious drawbacks, because this electrostatic shield (ES) [26]:

1. Dramatically suppresses discharge ignition, hence special efforts are required to ignite the discharge.
2. Increases the external size or decreases the useful internal discharge volume.
3. Impairs the inductive coupling by picking up some portion of inductive current.

### 2.3.1 Inductive sources geometries

The most common ICP source geometries for processing applications are the cylindrical (or top hat) design and the planar (or stove top) design.

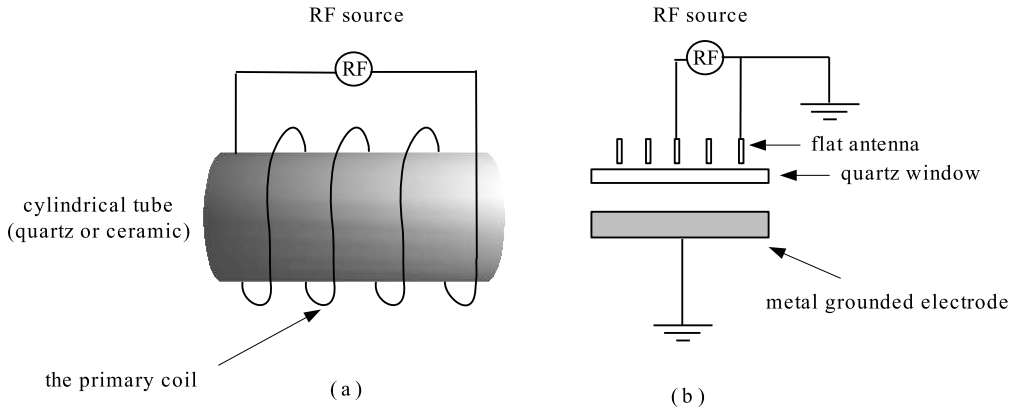


Figure 2.2: Inductive discharge in the (a) cylindrical and (b) planar configurations.

The inductive discharge in the cylindrical configuration has been extensively studied for over a century. It consists of a dielectric cylindrical tube and a metal helical coil (generally copper) is wound around it, as shown in Fig. (2.2 a). Inductive discharges can also be driven by a planar coil as shown in Fig. (2.2 b). For micro-electronic circuit fabrication the most common coil configuration is planar, where the coil is a flat spiral adjacent to a dielectric window on the top of a cylindrical chamber [7, 27]. There is a metallic grounded electrode on one side and a dielectric window on the opposite side of the discharge chamber. This dielectric window is usually made of quartz. It is transparent for both magnetic and electric fields and must be thick enough to withstand atmospheric pressure. In this work an inductive discharge with planar coil configuration is used. In both configurations the plasma is generated in the region of the most intense electric fields through ionization processes. The discharge is either maintained by the axial electrostatic field or by an azimuthal electromagnetic field of the primary coil. The electrostatic mode of operation appears at low RF power and the electromagnetic mode of operation appears when the coil current is large enough to induce an azimuthal electric field, that can maintain the ionization processes [13].

**Inductive RF sheath:** The RF-current passed through the external inductive coil in ICP discharges generates an RF magnetic field. The time variation of this magnetic field induces a circular (ring shaped) electric field. The power is

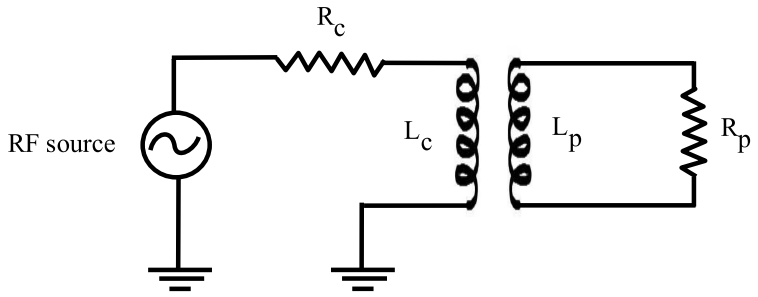


Figure 2.3: Transformer circuit model of the ICP. In the simplified circuit model, the inductance $L_p$ represents the secondary coil of the transformer, and $R_p$ represents the transformer secondary load.

transferred to the plasma via the dielectric window, i.e. there are no direct lines of electric field between the exciting coil and the plasma. The electric field lines in ICP discharges, are closed within the discharge and do not form oscillating sheaths as in case of CCRF discharges [28]. The sheath widths can stay small even for the high RF power input, which is needed for high density ICP operation.

**Transformer model:** The power absorbed by the plasma electrons can be estimated by using a circuit analysis derived from the so-called 'transformer formalism'. The ICP in both the cylindrical and planar configuration, as described by El-Fayoumi and Jones [29, 30], Piejak et al [31] and others, may be modeled electrically as a simple air-core transformer circuit as shown in Fig. (2.3). This model considers the induction coil as the primary side with N turns and inductance $L_c$, while the plasma acts as a single-turn secondary coil with inductance $L_p$ of the air-core transformer. The power is coupled from the primary to the secondary side. Because the coil and the plasma are adjacent, a mutual inductance M exists between the coil and the plasma inductance ($L_c$ and $L_p$). The coupling constant K, between the primary and secondary circuits is defined by:

$$K = \frac{M}{\sqrt{L_c L_p}} \tag{2.6}$$

The plasma conditions such as gas pressure, discharge type, applied RF power and the ICP source geometry set the values of the transformer circuit elements.

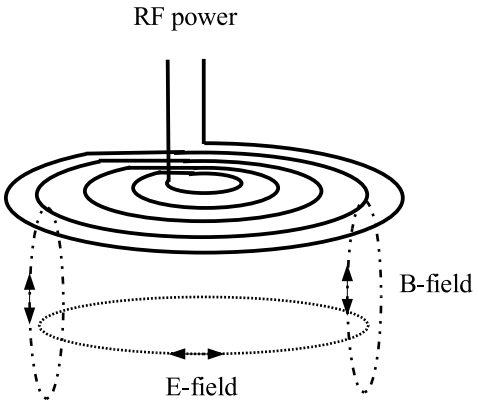


Figure 2.4: Schematic diagram of the electric and magnetic field lines as of a planar coil carrying RF current.

Even though the planar ICP source is difficult to model analytically as an air core transformer, measured impedance data show that the general behavior of the planar ICP is qualitatively similar to the cylindrical ICP. In low pressure ICP discharges, the bulk plasma electron density $n_e$ may be considered roughly uniform over the entire discharge volume, since the electron mean free path $\lambda_{mfp}$ is similar to or greater than the discharge chamber dimensions. In steady state the power balance states that power $P_{abs}$ absorbed by the plasma electrons from the driven antenna coil must balance the power $P_{dis}$ dissipated via collisions between electrons and the gas species. These collisions with the gas species still keep the power within the vessel but this power is dissipated by collisions with chamber wall, system cooling, gas flowing, etc.

### 2.3.2 Electromagnetic theory of ICP discharges

The basic excitation mechanism for the ICP in both the cylindrical and planar geometry is that the electric field required to transfer electrical power from the RF-power supply to the plasma electrons is provided by RF electric currents flowing through the excitation coil located outside of a gas containing chamber. This oscillating electric current in the coil creates a time dependent RF magnetic field $\overrightarrow{H}(r,t)$ around the coil; the situation is depicted in Fig. (2.4). This RF magnetic

field penetrates and sets up a similar time dependent RF-electric field $\overrightarrow{E}(r,t)$ in the plasma region according to Faraday's law:

$$\bigtriangledown \times \overrightarrow{E} = -\mu_0 \frac{\partial \overrightarrow{H}}{\partial t} \tag{2.7}$$

where $\mu_0 = 4\pi \times 10^{-7} H/m$ is the permeability of free space and $\overrightarrow{B} = \mu_0 \overrightarrow{H}$.

In the case of a planar coil ICP with an axisymmetric cylindrical geometry, the coil generates an inductive field of magnetic induction components $B_r(r,z)$ and $B_z(r,z)$ and an electric field component $E_\Theta(r,z)$. The plasma is treated here as a continuous medium in which the RF-current can flow in the conducting plasma in opposite direction to the coil current, similar to an electrical transformer. Maxwell's second equation (generalized form of the Ampere's law) relates both the electric and the magnetic fields with the associated current density $\overrightarrow{J}$ as:

$$\bigtriangledown \times \overrightarrow{B} = \mu_0 \overrightarrow{J} + \varepsilon_0 \mu_0 \frac{\partial \overrightarrow{E}}{\partial t} \tag{2.8}$$

These induced electric fields in the plasma accelerate electrons via $eE_{rf}$ forces. These accelerated free electrons collide with and ionize feedstock gas molecules, thus sustaining the plasma [1]. In addition to the generated induced electric field, the excitation coil creates also a capacitive field due to voltage between the coil terminals. The penetration of capacitive components into plasma can be prevented by placing a Faraday (electrostatic) shield between the coil and the plasma as mentioned before.

The induced electric field in the plasma does not propagate into the plasma volume, but it is penetrating into the plasma electrons within a narrow region called the "skin depth" layer of scale length thickness $\delta$ . This skin depth layer is located close to the inductive coil, just below the dielectric window. In the skin depth or in the sheath region most of the interaction between the external power source and the plasma electrons occurs. The electromagnetic skin depth is an important factor influencing plasma uniformity, because it determines the scale length for the absorption of electromagnetic energy [32]. In case of low pressure discharges, the skin depth thickness $\delta$ is given as [7, 32]:

$$\delta = [\frac{m_e}{e^2 \mu_0 n_e}]^{1/2} \tag{2.9}$$

where $m_e$ and $e$ are the electron mass and charge respectively and $\mu_0 = 4\pi \times 10^{-7} H/m$ is the permeability of free space. $\delta$ is typically 1 or 2 cm in case of $n_e = 10^{11} cm^{-3}$.

The skin depth in a plasma can be anomalously greater at low pressure (electron ionization mean free path $> \delta$) due to the motion of high-energy electrons out of this region [32]. The thermal motion of the electrons must be taken into account when the pressure falls clearly below 20 mTorr (2.66 Pa) [33, 34]. Since we are away from this pressure, we have a normal skin effect thickness in our discharge as mentioned in the preceding equation.

### 2.3.3 Heating mechanisms in inductively coupled plasma discharges

Electron heating is one of the key processes that determine the power deposition and spatial uniformity of the plasma [28], which are two important aspects in industrial plasmas. For low pressure discharges the plasma is not in thermal equilibrium, and the electric power from the external source is coupled most efficiently to the plasma electrons. In the bulk plasma energy is transferred from electrons to ions and neutrals by collisional processes. Depending on the method of sustaining the plasma from an external source, there are various ways of transferring energy to the plasma electrons and indirectly to the ions. The resulting heating mechanisms are ohmic heating, stochastic heating, resonant wave-particle interaction heating, and secondary electron emission heating. Understanding of such heating mechanisms is important in predicting whether a plasma is radially uniform. Ohmic and stochastic electron heating are the dominant mechanisms capacitively coupled RF-discharges. In low-density inductively coupled discharges, the power is transferred from the inductive RF electric fields to the plasma electrons within the skin depth layer near the plasma boundary by collisional (ohmic) dissipation, and by collisionless heating processes in which plasma electrons "collide" with the oscillating electric field [35].

#### 2.3.3.1 Joule (collisional) heating

Joule (Ohmic) heating is present in all discharges and principally due to the transfer of electron energy through collisional processes involving neutral background gas. Ohmic heating is particularly important at high pressures (above ≈20 mTorr) at which the collisional frequency is high, where it can be the dominant heating

mechanism [36]. In this operating regime the electron mean free path $\lambda_{mfp}$ is small compared to characteristic discharge dimensions. The normal skin effect in inductively coupled discharges is accompanied by ohmic (collisional) heating [23]. In the presence of a dc electric field E, the electron current density $J_e$ is given by [37]:

$$J_e = \sigma_{e,dc} E \tag{2.10}$$

The electron collisional heating or ohmic heating can be accurately described by:

$$Ohmic\,heating = J_e E = \sigma_{e,dc} E^2 \tag{2.11}$$

where $\sigma_e$ is the electron conductivity, given as:

$$\sigma_{e,dc} = e n_e \mu_e \tag{2.12}$$

with $n_e$ and $\mu_e$ the electron density and mobility respectively .

In case of an RF field, the field angular frequency $\omega$ is not negligible with respect to the electron collisional frequency $\nu_m$, there is a phase shift between electron current and electric field. In this case the ohmic heating becomes:

$$Ohmic\,heating = \sigma_{e,dc}\{\nu_m^2/(\nu_m^2 + \omega^2)\} E_{rms}^2 \tag{2.13}$$

#### 2.3.3.2 Collisionless heating

Collisionless electron heating mechanism is an effect analogous to the anomalous skin effect in metals [36]. In this operating regime, the mean free path $\lambda_{mfp}$ is larger than or comparable to the discharge dimensions. Collisionless electron heating is of fundamental interest in plasma physics [7]; both experimental and theoretical results in lower pressure discharges (CCRF, ICP and ECR) indicate that power deposition involves a collisionless electron heating mechanism [33, 38, 39]. The heating in the collisionless regime is ascribed to nonlocal behaviour of electrons such as resonant interaction with electromagnetic fields and specular reflections at the boundary [40]. Interesting kinetic effects are caused by thermal motion of electrons in this regime [28]. Collisionless (stochastic) electron heating is well known for CCRF- discharges where it occurs in the vicinity of boundaries

due to inelastic collisions of plasma electrons with oscillating sheath boundaries [41, 42]. This collisionless heating mechanism may also occur in the skin depth layer of an inductively coupled discharge [37] and it becomes important when the effective electron mean free path exceeds the skin depth. The existence of collisionless (stochastic) heating in the ICP was suggested by Godyak et al. [20].

Stochastic (collisionless) heating in inductive discharges can be described as follows [37]: Electrons with thermal energy described by a Maxwellian distribution with $T_e$ in the bulk plasma enter the RF skin depth region. These electrons then feel the RF electric field in the skin depth region, but they continue moving toward the dielectric window. At any dielectric window-plasma interface a floating sheath exists to keep electrons trapped in the plasma. The thermal electrons impinge on the floating sheath and are repelled back towards the bulk plasma, if collisions with neutrals are negligible during that time. They continue to feel the RF field in the skin depth region until they are back into the plasma bulk. If the time the electrons spent in the skin depth region is smaller than the RF period $T_{RF} = \frac{1}{f_{RF}}$, then the electrons gain energy from the RF field which is transferred to the bulk plasma through electron-neutral collisions in the plasma bulk.

# Chapter 3

## Diagnostic concepts of RF-excited discharges

Plasma diagnostics play an important role in industrial plasma processing. The importance of these diagnostic methods is that they are essential for quality control and reducing costs. Application of different diagnostic methods for a specific kind of plasma enables one to check and improve the product quality. Moreover, it helps to get more information about the plasma under consideration.

In this chapter a brief description of different plasma diagnostic methods with some examples will be mentioned. The diagnostic methods used during this work will be discussed in more detail later.

### 3.1 An overview of different plasma diagnostic techniques

#### 3.1.1 Absorption spectroscopy

Direct absorption spectroscopy is a simple technique used to obtain information about gas phase species by access to the ground state particles. A bound system may absorb a photon if the energy of the incident photon corresponds to the energy of an allowed transition. The radiation of an external light source such as a deuterium lamp (for ultraviolet region), a tungsten lamp (for visible region) or a laser is directed through the discharge. The intensity $I$ of light at a given wavelength transmitted through a plasma is given by Beer's law:

$$I = I_0 e^{-\sigma n l} \tag{3.1}$$

where $I_0$ is the intensity of the incident light, $\sigma$ is the absorption cross-section of the specific transition, $n$ is the density of absorbing species and $l$ is the optical

path length.

If the absorption cross-section of the species is known, the density can be calculated from the intensity of the transmitted light. The main advantage of this technique is its ease of implementation in most cases, but it requires high spectral resolution [3].

**Diode Laser Absorption (DLA):** This is an optically active technique in which a laser beam after penetrating the plasma is detected to measure the absorption coefficient of the plasma. Absorption spectroscopy with tunable diode lasers can provide direct information on atomic, molecular and ionic densities. By tuning the frequency of the laser, the line profile can be measured. Electron density or heavy particle temperature can be measured from the line width by Stark broadening or by Doppler broadening respectively. The absolute value of the absorption coefficient gives the density of the excited state that absorbs the laser radiation. The detector used for Diode Laser Absorption is a photodiode; Intensified Charged Coupled Device (ICCD) could be used for the spatially resolved requirements. The sensitivity of this technique can be improved by an optical multi-pass system. An extension of this technique is the so called Cavity Ring-Down (CRD).

**Cavity Ring-Down Absorption Spectroscopy (CRD):** Cavity ring-down (CRD) spectroscopy is a versatile and highly sensitive (detection limit typically $10^{-8}\,cm^{-1}$) absorption technique used in the optical absorption analysis of atoms and molecules. The CRD technique was first demonstrated by O'Keefe and Deacon in 1988. This technique is based on the measurement of the absorption (decay) rate of light confined in an optical cavity and, therefore, is insensitive to intensity fluctuations of the light source. In this technique, light from a pulsed or continuous wave (cw) laser is coupled into a stable, high-finesse (low-loss) optical cavity formed by two dielectric multilayer reflectors mirrors separated by a distance $d$ around the sample medium (discharge) with density $n$. The laser beam must be aligned onto the cavity axis such that the laser beam is reflected back into itself [43]. The light inside the cavity is reflected many times back and forth between the mirrors. The light intensity inside the cavity will decay exponentially as a result of light exiting the cavity during reflections; this decay is detected. The time at which the light intensity inside the cavity decreases to $1/e$ of its initial value

is called the ring-down time $\tau$. The ring-down time as a result of introducing an absorber over a path length $l$ inside the cavity is given by:

$$\tau = \frac{d}{c[(1-R)+kl]} \tag{3.2}$$

where $d$ is the cavity length, $c$ is the speed of light, $R$ is the mirror reflectivity and $k$ is the absorption coefficient of the absorber.

An absorption spectrum can be obtained by measuring the empty cavity ring-down time and the change in ring down time due to the absorber as a function of the wavelength of the laser used. The sensitivity attainable with CRD spectroscopy depends on the reflectivity of the cavity mirrors and the accuracy with which the ring down time can be determined. The technique can be used for spectroscopic investigations of molecular species to obtain information about molecular structure and energy levels and it can also be used in trace gas analysis. The cavity ring-down (CRD) technique has advantages that combines a good sensitivity with a rather simple and straightforward experimental set-up [44].

### 3.1.2 Laser Thomson Scattering (LTS)

In laser scattering diagnostic techniques, the radiation scattered by the plasma is studied. The probability of scattering can be as low as $10^{-17}$, which demands a strong light source such as a pulsed laser and sensitive detection.

Thomson scattering is a process by which the laser radiation is partly scattered in various directions by free electrons in the plasma. It is a non-intrusive diagnostic method applied to measure the free electron gas properties, such as electron density , electron temperature and energy distribution. Under special conditions the density and temperature of ions could be also measured. We will restrict this remark on Thomson scattering to the case:

$$\lambda_D \gg \frac{\lambda}{4\pi sin\frac{\theta}{2}} \tag{3.3}$$

where $\lambda_D$ is the Debye length, $\lambda$ the laser wavelength and $\theta$ is the scattering angle between the laser beam and the direction from the scattering volume to the observer.

This condition will be fulfilled, as a rule, for low-temperature plasmas and sizeable angles $\theta$. The integral intensity of Thomson scattered radiation is directly

proportional to the electron density $n_e$, and the spectral line profile is determined by the Doppler shift caused by the electron motion in this case. The electron density $n_e$ can be determined absolutely by calibrating the optical system of LTS with the aid of the intensity of rotational Raman scattering in nitrogen with a known density $n_{N_2}$ and temperature [45, 46]:

$$n_e = n_{N_2} \frac{I_T}{I_{Rm}} \Gamma_{Rm} \tag{3.4}$$

where $I_T$ and $I_{Rm}$ are the measured intensity of LTS and the sum of the intensities of the various rotational Raman lines respectively. $\Gamma_{Rm}$ represents the cross-section ratio of the two scattering types.

If the electron velocity distribution function (EVDF) is isotropic, then the measured scattering spectrum represents the one dimensional EVDF. In the case of Maxwellian electron energy distribution function (EEDF) of the plasma, the scattering spectrum has a Gaussian profile and $\triangle\lambda_{1/e}$ is directly related to the electron temperature as [45, 46]:

$$T_e = [\frac{m_e c^2}{8 k_B \lambda^2 sin^2(\theta/2)}] \triangle \lambda_{1/e}^2 \tag{3.5}$$

where $m_e$ is the electron mass, $c$ the speed of light, $k_B$ the Boltzmann constant.

In addition to the direct measurements of electron density and temperature, laser Thomson scattering technique has other advantages such as, high spatial resolution and limited influence on the plasma. The main problems of this technique are the extreme low scattering cross-section, the presence of relatively intense stray light; therefore it is experimentally demanding.

## 3.2 The diagnostic methods applied

The basic diagnostic method used in these studies of low temperature inductively coupled hydrogen plasma discharge is optical emission spectroscopy (OES), using a 2m-spectrograph in combination with a fast gated intensified charged coupled device (ICCD) as detector to record the emission lines of interest. Using this technique, we extract information on the gas temperature and the degree of dissociation. The results of the gas temperature are compared with corresponding results obtained by Fabry-Perot interferometry (FPI). Moreover, the Langmuir probe (LP) diagnostic technique is used in order to gather information about

different plasma parameters such as electron density, electron temperature and electron energy distribution function, which can be used also in the determination of the degree of dissociation. On the other hand a measurement of the atomic hydrogen density by two-photon laser induced fluorescence (TALIF) has been performed; these results are compared with OES results.

### 3.2.1 Optical Emission Spectroscopy (OES)

Optical emission spectroscopy (OES) is one of the most popular plasma diagnostic methods in both research laboratories and industry because of its simplicity and accuracy [47]. OES has proven to be a very powerful tool used to monitor gas-phase population during process development and for end point detection during integrated circuit (IC) manufacturing. Another important advantage of this method is its low 'cost', since in principle all you need for OES method is a lens and a detection system. Because in experiments it is unsatisfactory to use probes inserted into the plasma to determine internal plasma parameters; in this case OES is a convenient non-intrusive diagnostic tool, that operates without disturbing the discharge objects under consideration. If the required model is applied OES is a suitable method for determination of important plasma parameters such as electron densities $n_e$, electron temperatures $T_e$ and the gas temperature $T_g$. It is also used to infer other more complex plasma parameters such as electron energy distribution functions and degrees of dissociation. Fig. (3.1) shows both the absorption and emission processes. In case of emission, an atom relaxes from its higher state to a lower state. It may lose that energy in the form of light, provided that the transition is allowed.

**The corona model:** The corona model is based on the assumptions that only the plasma electrons have kinetic energies high enough to excite the atoms and molecules. In this model, excitation by collisions with other excited species and cascading processes from higher excited states as well as de-excitation by collisional quenching are considered negligible, and only the de-excitation through spontaneous emission process is balanced by the direct electron impact excitation from the ground state [48, 49]. Based on the present model, the excited state $n_k^*$ is populated by electron impact excitation with ground state particles in a single step:

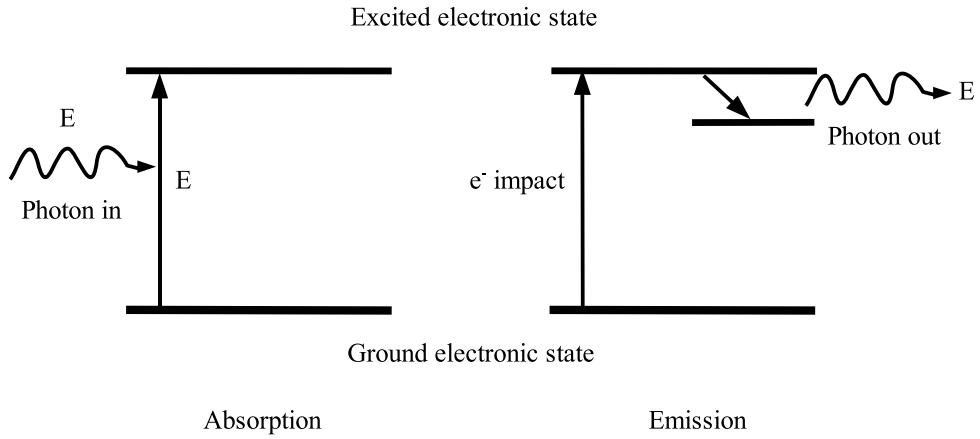


Figure 3.1: Absorption and emission processes.

$$e^- + n_g \rightarrow n_k^* + e^- \tag{3.6}$$

The de-excitation by radiative processes is given as:

$$n_k^* \rightarrow n_j^* + h\nu_{kj} \tag{3.7}$$

Cascading processes from higher excited states are omitted in the corona model, and the emission intensity of spectral lines is given by [6]:

$$I(\lambda_{kj}) = C\frac{A_{kj}}{\sum_j A_{kj}} h\nu_{kj} n_e X_{exc}^k n_g \tag{3.8}$$

where $n_e$ is the electron density, $n_g$ is the population of the ground state $h\nu_{kj}$ is the energy of the transition under investigation, $A_{kj}$ is the Einstein coefficient (transition rate) for spontaneous emission and $X_{exc}^k$ is the excitation rate coefficient into the level $k$ for electron collisions with ground state particles. $\sum_j A_{kj}$ comprises all radiating transitions starting at level $k$. The factor $C$ contains all geometrical and optical parameters of the observation system.

Taking into account radiationless process, the effective de-excitation rate of an excited state $k$ is written as:

$$A_k = \sum_j A_{kj} g_{kj} + \sum_q k_q n_q = \frac{1}{\tau_k} + \sum_q k_q n_q \tag{3.9}$$

Here $g_{kj}$ is the escape-factor, which has values of 1 or 0 in case of optically thin or optically thick plasma respectively, $\sum_j A_{kj} g_{kj}$ the reciprocal of the life time $\tau_k$ of the level and $k_q$ is the specific de-excitation collisional (quenching) coefficient of the excited species.

In this case eq. (3.8) becomes:

$$I(\lambda_{kj}) = C \frac{A_{kj}}{A_k} h\nu_{kj} n_e X^k_{exc} n_g \tag{3.10}$$

The excitation rate coefficient (electron impact excitation) is a complex function. It can be expressed in terms of the cross section for electron collisions and the electron energy distribution function as:

$$X^k_{exc} = \int \sigma_{exc}(E) \sqrt{\frac{2E}{m_e}} f(E) dE \tag{3.11}$$

where $\sigma_{exc}(E)$ is the excitation cross section for electron collisions, $E$ is the electron energy, $m_e$ is the electron mass, $f(E)$ is the electron energy distribution function.

**Practical aspects:** Optical emission spectroscopy instrumentation involves the collection, spectral dispersion and the detection of light, these can be discussed as follows:

**Optical system for light collection:** Normally, an optical system consists of a combination of mirrors and lenses, and in some cases it could be just only one lens depending on the situation of the experimental setup. Mirrors are sometimes preferred because of absence of chromatic aberrations.

**Wavelength selection:** The light collected by the optical system can be dispersed by means of filters, prisms or grating systems (spectrograph). One design of a grating spectrograph is that a mirror images the source from the entrance slit onto a parallel beam that is directed to the diffraction grating. The same mirror or another mirror (depending on the mounting type) focuses the diffracted beam onto the exit slit. The diffraction grating is commonly a square, of length $l$, with

$\nu$ grooves per millimeter. The groove density determines the spectral dispersion and the grating equation is given by:

$$m\lambda = d(sin(i) - sin(r)) \tag{3.12}$$

where $m$ is the diffraction order, $d$ is the groove separation, and $i$ and $r$ are the angles of incidence and reflection (diffraction) respectively.

For infinitely narrow slits the resolvable $\Delta\lambda$ is given by:

$$\frac{\lambda}{\Delta\lambda} = R = \nu lm$$

For finite slit width the spectral resolution due to dispersion is given by [50]:

$$\Delta\lambda = \frac{w}{m\nu f} cos(i) \tag{3.13}$$

where $w$ is the slit width of the spectrograph, and $f$ is the spectrograph focal length which is the distance from the exit plane to the last focusing mirror.

It is important to mention that the efficiency of a grating system is a function of wavelength too, therefore, it must be taken into account in the emission intensity detected. The spectral resolution of an OES system is often limited by the detector, instead of the grating's groove density.

**A detection system for recording spectral lines:** A detector is simply a device that senses and measures the dispersed light from the diffraction grating system (spectrograph) across a range of wavelengths. Such detectors are known as opto-electronic devices, among them photodiode, photomultiplier and Charged Coupled Device (CCD) array detector. We will restrict our discussion to the CCD detector.

**Charged Coupled Device (CCD):** A charge coupled device (CCD) image sensor is an analogue integrated circuit (IC) that converts an optical image into an electronic output. It is essentially an array of metal-oxide-semiconductor (MOS) capacitors (pixel). The photo MOS type is a simple device made of a P-type semiconductor with a thin layer of silicon dioxide above it. A very thin transparent layer of metal or highly doped semiconductor is placed on the top of the oxide layer, known as the gate. Normally, two dimensional arrays of these photosensitive

elements MOS capacitors are linked, so that the charge stored in each one may be transferred to adjacent capacitors by the correct sequence of bias signals. Charge is created in each capacitor when incident photons are absorbed in the sensitive (semiconductor) region of the device, which generates electrons or photoelectrons. Each of these single capacitors represents one pixel in the 2-D map when displayed on computer. To avoid build up of thermally excited charge at longer integration times, CCD's must be cooled. Such cooling could be done either by thermo-electric Peltier coolers, or by liquid nitrogen. The quantum efficiency QE (measure of how many electrons are produced for every photon absorbed by the light sensitive area of the detector) and the dynamic range of CCD detectors are typically lower than that of photodiodes, however CCD arrays have lower noise readout electronics and they are preferred at low temperature operations.

**Image Intensifiers:** The incorporation of image intensifiers into high-performance Charged Coupled Device (CCD) cameras has produced intensified CCD (ICCD) systems for imaging and spectroscopy that possess high sensitivity in ultra-low-light conditions and allow temporal resolution of extremely fast phenomena (less than 2 ns). These ICCD systems are widely used in optical emission spectroscopy (OES), laser induced fluorescence (LIF) and laser induced breakdown spectroscopy (LIBS). Intensified Charged Coupled Devices are preferred in OES measurements because they have the advantage of measuring the intensities of the rotational lines, like Fulcher band simultaneously and additionally more than one dimension can be provided. An image intensifier is a vacuum tube device, generally 18-25 mm in diameter. The intensifier comprises a photocathode input, a phosphor screen, and a complex electron-multiplying microchannel plate (MCP) as shown in Fig. (3.2).

The photocathode is the first major component in an image intensifier. Photocathode coatings convert a portion of the incident light photons into electrons via the photoelectric effect. These electrons are then multiplied and accelerated to the phosphor screen, where they strike the coating and light is released. This released light consists of many photons for every incident photon striking the photocathode surface. ICCDs use photocathode coatings with higher quantum efficiency (QE) in the blue/green region of the spectrum such as GaAs. A component of the noise in an intensifier comes from thermally generated electrons from the photocathode, which contaminate the image signal. This contamination can

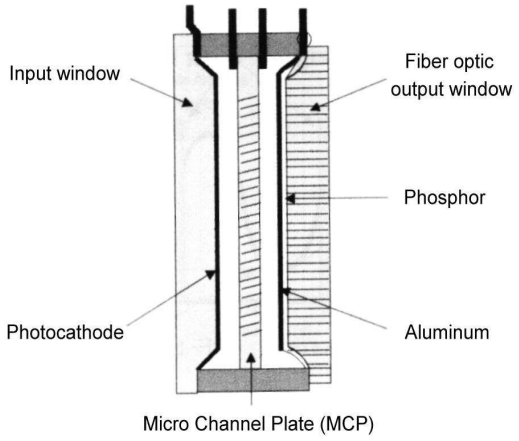


Figure 3.2: The construction of an image intensifier.

be reduced by cooling the image intensifier.

The Micro-channel Plate (MCP) is the second component of an image intensifier. MCP is a planar device which intensifies impinging radiation by multiplication of electrons in small channels under the presence of a high electric field. MCP consists of a slightly conductive glass substrate (approximately 2 cm in diameter and 0.5 mm thick) with millions of parallel traversing etched channels of around 10 $\mu m$ diameter with spacing of several tens of microns, containing a secondary electron emitter like cesium and copper iodide on their inner walls. These channels are set at a small bias angle to the major axis of the MCP to increase the chances for collisions of electrons with the channel walls. Electrons generated by the photocathode are driven through the channels by a constant field from a voltage (600 V-1 kV) [51] applied to the MCP. Electrons which travel inside these channels scatter frequently with the channel walls producing more and more secondary electrons. This process amplifies the original signal by several orders of magnitude depending on the electric field strength and the geometry of the Microchannel plate. The quantum efficiency (QE) for a standard MCP is approximately 65 %.

The third major component of an image intensifier is the phosphor screen. Electrons exciting the MCP are accelerated by a constant voltage (5-8 kV) and

strike the screen, where they are converted back into light photons which are guided and detected by the CCD. The phosphor screen is covered by aluminium surface which acts as a mirror in both directions. Various phosphor screens with different features are used. They differ in their luminescence colour, efficiency, decay time and grain size. It usually emits a green light, for which the CCD is more sensitive.

**Coupling of Image Intensifiers to CCDs:** Intensified Charged Coupled Device (ICCD) is a CCD that is connected to the output window of the intensifier. The output window could be either fiber optical based or by a lens system. Lens coupling has the advantage of flexibility in adding or removing an intensifier. Disadvantages of such coupling include lower light throughput (5-10 %) and increased stray light in the camera system. CCD coupling via fiberoptics offers better light throughput, less signal to noise ratio than lens coupled device. Fiberoptic couplings are capable of sensitivities approaching single photoelectron detection. Disadvantages are that the fiberoptic coupling is permanent and the detector must be operated in a dry, non-vacuum, inert environment.

**Image Intensifier gating:** Temporal resolution in an ICCD camera is made possible by switching the intensifier on and off very rapidly (gating). If the photocathode is biased more positively than the MCP, electrons will not enter the MCP and the intensifier is gated off. If the photocathode is negatively biased, electrons will be accelerated into the MCP and the intensifier is gated on. Hence the image intensifier can be seen as a shutter whereas the CCD can be seen as an integration and storage device.

### 3.2.2 Interferometric method using Fabry-Perot Interferometer (FPI)

The need for another technique to prove measurements of gas temperature was very important to clarify whether we really measure the gas temperature or not. Since the plasma optical emission provides enough intensity for interferometry measurement and signal detection, the known Fabry-Perot interferometry technique in connection with the 2-meter spectrograph is chosen to provide proof. A brief description about the principles of this interferometer will be given now.

An interferometer is an optical device in which two or more waves are allowed to interfere by coherent addition of electric fields, the observed intensity is modulated

according to whether the fields interfere in phase or out of phase hence constructive or destructive interference could be obtained, respectively [52]. The Fabry-Perot interferometer (FPI) was devised by Charles Fabry and Alfred Perot and it is constructed with two partially transmitting mirrors. These mirrors can be flat or radiused, placed parallel to each other. If the plate spacing can be mechanically varied, the device is called an interferometer, whereas if the plates are held fixed, it is called an etalon. FPI employs multiple-beam interference to produce a sharp interference pattern of very high resolution and it is described in detail elsewhere [53, 54]. The conditions under which sharp multiple beam frings can be employed have been summarized as follows [55]:

1. The surfaces must be coated with a highly reflecting film of minimal absorption.
2. The surfaces must be separated by at most a few wavelengths of light.
3. A parallel beam should be used.
4. The incidence should preferably be normal.

The Airy's function which describes the performance of a Fabry-Perot etalon can be expressed for perfectly lossless mirrors by [56]:

$$\frac{T}{T_{max}} = [1 + \frac{4R}{(1-R)^2} sin^2(\frac{\phi}{2})]^{-1} \tag{3.14}$$

where $T$ and $R$ are the transmittance and reflectance of the FPI mirrors. The absorption of the plate material should be negligible, thus $T + R = 1$ and $\phi$ is the round trip phase change which is given by [56]:

$$\phi = (2\pi/\lambda)2ndcos\theta \tag{3.15}$$

where $d$ is the distance between the two mirrors (also known as cavity spacing), $n$ the refractive index of the medium between the two mirrors and $\theta$ is the angle between the normal surface of the mirrors and the incident light.

The condition for constructive interference for a transmitted wavefront is:

$$m\lambda = 2ndcos\theta \tag{3.16}$$

where $m$ is an integer.

In case of normal incidence:

$$m\lambda = 2nd \tag{3.17}$$

and the phase difference $\phi$ is given by:

$$\phi = (2\pi/\lambda)2nd = 2m\pi = \frac{4\pi}{\lambda}nd \tag{3.18}$$

**The free spectral range ($\Delta\lambda_{FSR}$):** The free spectral range of the FPI instrument is defined as the distance between two peaks for successive orders of n. It is a measure for the useful working range (no overlapping orders) and is given by the period of the Airy function as:

$$\Delta\lambda_{FSR} = \lambda^2/2nd \tag{3.19}$$

**Finesse ($F$):** Finesse ($F$) is a numerical value describing the performance of a FP (characterizing the width or the sharpness of the maximum) and is defined as the ratio of the free spectral range to the full width at half maximum of a peak, or the ratio of peak distance to peak halfwidth.

**Resolution ($\Delta\lambda_{Res}$):** The resolution of an optical instrument is defined by the bandwidth of a spectral line, i.e. the broadening imposed on the line by the instrument and it can be expressed by the finesse as:

$$\frac{\lambda}{\Delta\lambda_{Res}} = mF \tag{3.20}$$

The last equation is the resolving power of the instrument and is defined by the product of the finesse $F$ and the interference order $m$, hence:

$$\Delta\lambda_{Res} = \frac{\lambda}{mF} = \frac{\lambda^2}{2nd}\frac{1}{F} = \frac{\Delta\lambda_{FSR}}{F} \tag{3.21}$$

This leads to:

$$F = \frac{\Delta\lambda_{FSR}}{\Delta\lambda_{Res}} \tag{3.22}$$

### 3.2.3 Langmuir Probe Diagnostics

Electrostatic or Langmuir probe measurement is an experimentally simple method used to determine several basic discharge parameters, such as plasma potential,

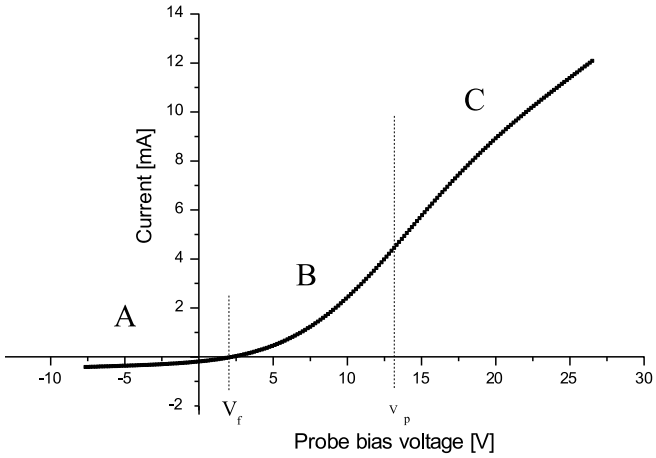


Figure 3.3: Characteristic curve of a Langmuir probe.

floating potential, charged-particle densities and temperatures. It can be used to determine the spatial density profiles and the electron energy distribution function (EEDF) in high density-low pressure plasma, but it does not provide information on the chemistry of the plasma. This diagnostic method dates back to Langmuir, over fifty years ago. A Langmuir probe is a metallic electrode made of a high melting point metal such as tungsten, molybdenum or platinum. This electrode is insulated, except the tip which is in contact with the plasma. Because the Langmuir probe has to be inserted into the plasma, this technique is an in-situ intrusive diagnostic method that may cause local perturbation of the plasma. The probe tip is several mm long and mm or smaller in diameter. Cylindrical probes are preferred to spherical or planar because of their simplicity in construction and smaller collecting area that could decrease the disturbances that is created in the plasma.

**Theory of the Langmuir probe:** The Langmuir probe diagnostic method involves the measurement of electron and ion currents to the probe as different voltages from an external power supply are applied to the probe. The current collected by the probe is representative of the charged particles attracted by the biased probe tip. This current is determined as a function of applied (bias) voltage.

The resulting curve is called the current-voltage (I-V) probe characteristic of the plasma. From the shape of this I-V characteristic, it is possible to derive the main plasma properties when the appropriate theories are applied. A typical probe characteristic curve (I-V curve) is shown in Fig. (3.3). Here we have to define two main potentials which divide the I-V characteristic curve measured by a Langmuir probe into three regions. Firstly the floating potential $V_f$ is the potential at which the probe draws equal ion and electron currents (net current is zero). The second one is the plasma potential $V_p$ and is defined as the potential at which the plasma and probe potentials are equal. Three characteristic regions A, B and C are represented:

- A: The ion saturation region

In this region the biasing probe potential $V_{bias}$ is strongly negative with respect to the plasma potential $V_p$. Electrons, even highly energetic ones, are repelled and only ions are collected by the probe. The ion saturation current is reached and as a result an ion sheath develops in front of the probe tip.

- B: The electron collection region

This is the intermediate region. If the biasing probe potential $V_{bias}$ equals the floating potential $V_f$, the fluxes of electrons and ions are equal and the probe is at the floating potential ($I_{tot} = 0$). With increasing the biasing probe potential $V_{bias}$ past $V_f$, electrons are still repelled, but some of them (the most energetic ones) have enough energy to hit the probe tip resulting in a negative current. When $V_{bias}$ is increased further, the electron current continues to increase, causing the measured current to increase until the probe voltage $V_{bias}$ equals the plasma potential $V_p$.

- C: The electron saturation current region

In this region the biasing probe potential $V_{bias}$ is positive with respect to the plasma space potential $V_p$, electrons are collected by the probe, and the electron current reaches a saturated level, while ions are fully repelled. The probe tip in this case is surrounded by an electron sheath.

The classical Langmuir approach states that by evaluating the slope of the line that fits $\ln(I_e)$ versus $V$ of the probe characteristics in the electron collection region where the probe potential is less than the plasma potential, the electron

temperature $T_e$ is obtained [57]. Using the obtained electron temperature $T_e$, the mean electron velocity is determined according to:

$$\bar{v}_e = (8k_B T_e/\pi m_e)^{1/2} \tag{3.23}$$

The density $n_e$ can be computed by measuring the electron saturation current which is defined as [57]:

$$I_{esat} = \frac{1}{4} e n_e \bar{v}_e A_p \tag{3.24}$$

where the probe bias voltage equals the plasma potential and $A_p$ is the collecting area of the probe and given by $A_p = 2\pi l_p r_p$.

Depending on the nature of the sheaths in front of the probe, different theories are employed to calculate the plasma parameters from the I-V curve. Sheaths are defined to be either thick or thin. Thick sheaths are obtained when the sheath width is larger than the radius of the probe $l_s > r_p$. In the opposite case $l_s < r_p$ the sheath is said to be thin sheath.

- In the case of collisional sheaths i.e, mean free path of the particles is smaller than Debye length or more precisely the sheath width ($\lambda_{mfp} < l_s$), hence particles can undergo collisions and its movement becomes radial. Allen, Boyed and Reynolds in 1957 developed the so called ABR (radial) theory for these collisional sheaths which was completed by Chen in 1965.

- If the sheaths are collisionless i.e, mean free path of the particles is larger than sheath width ($\lambda_{mfp} > l_s$), the particles conserve their total energy and momentum. A theory called Orbital Motion Limited (OML) can be used in that case. The basics of the OML theory was first introduced by Mott-Smith and Langmuir [58]. Laframboise [59] refined the theory by improving the analysis of the ion saturation region.

The data handling system of our Langmuir probe (Smart Probe of Scientific Systems Ltd.) uses the OML analysis of the Laframboise theory. The plasma potential is calculated as the crossing point of the second derivative of the I(V) with zero and the floating potential is found at the point where $I_{tot} = 0$.

**Determination of plasma parameters using the smart probe system:** The electron temperature is calculated by taking the current measured at the

plasma potential and dividing it by the integral of the I-V curve from the $V_f$ to $V_p$ as follows [60]:

$$\frac{I(V_p)}{\int_{V_f}^{V_p} I(V)dV} = \frac{1}{k_B T_e} \tag{3.25}$$

Once the electron temperature $k_B T_e$ (in eV) is determined, the electron density $n_e$ is calculated according to:

$$n_e = \frac{I(V_p)}{A_p}(\frac{2\pi m_e}{e^3 k_B T_e})^{1/2} \tag{3.26}$$

where $A_P$ is the area of the probe, $m_e$ mass of electron and $e$ electronic charge

Electron Energy Distribution Function (EEDF), $f(\varepsilon)$, provides information on the energy available for excitation or ionization of the discharge gas. The Smart Probe software offers the possibility of obtaining the EEDF from the measured I-V curve.

Mott-Smith and Langmuir [58], Druyvesteyn [61] showed that the second derivative of the probe current with respect to the probe bias voltage is proportional to the EEDF, which is given as [7]:

$$f(\varepsilon) = \frac{2m}{e^2 A_p}(\frac{2eV}{m})^{1/2}\frac{d^2 I_e}{dV^2} \tag{3.27}$$

This is referred to as the Druyvesteyn formula. The plasma potential is the voltage where the second derivative of the electron current $I_e$ is zero and takes into account that when the probe voltage $V_{bias}$ equal the plasma $V_p$ there is no sheath.

One can use the Electron Energy Probability Function (EEPF), $f_p(\varepsilon)$, since its representation in a semi-logarithmic plot as function of energy $\varepsilon$ is a straight line for a Maxwellian distribution. The EEPF is deduced from the EEDF as:

$$f_p(\varepsilon) = \frac{f(\varepsilon)}{\sqrt{\varepsilon}} \tag{3.28}$$

where $\varepsilon$ is the electron energy, the function $f_p(\varepsilon)$ is expressed in $cm^{-3}eV^{-3/2}$

The electron density $n_e$ can be deduced from the integration of the measured EEDF's as:

$$n_e = \int_0^\infty f(\varepsilon)d\varepsilon = \int_0^\infty \sqrt{\varepsilon} f_p(\varepsilon)d\varepsilon \tag{3.29}$$

also the mean electron energy $\bar{\varepsilon}$ is given by:

$$\bar{\varepsilon} = \frac{1}{n_e}\int_0^\infty \varepsilon f(\varepsilon)d\varepsilon = \frac{1}{n_e}\int_0^\infty \varepsilon\sqrt{\varepsilon} f_p(\varepsilon)d\varepsilon \tag{3.30}$$

which gives the effective electron temperature as:

$$k_B T_{eff} = \frac{2}{3}\bar{\varepsilon} \tag{3.31}$$

### 3.2.4 Two Photon Absorption Laser Induced Fluorescence (TALIF)

The particles in the plasma are pumped by resonant absorption of laser radiation into short-lived higher energy levels. After a short time (fluorescence time) these particles may lose this extra absorbed energy by emitting a photon and return to their low energy states as shown in Fig. (3.4). The emitted photons obtained from these particles are called fluorescence radiation and such technique is called laser induced fluorescence (LIF). The intensity of the fluorescence radiation is proportional to the particle density. The density of molecules, atoms, and ions in the ground state, as well as in metastable or unstable excited states, can be determined by measuring the number of emitted photons, i.e. the intensity of the fluorescence radiation. It is convenient to choose a wavelength different from the pump wavelength, so that stray light is of no concern. A tunable (dye) laser is generally used to tune the frequency of the exciting light. Dye lasers, pumped by either an excimer laser or a Nd-Yag laser are highest in peak power and are the most common tunable pulsed sources. To use the LIF technique, the investigated species must fluoresce and the tunable laser must be able to match a transition for the investigated species [3].

TALIF is the diagnostic technique used for the detection of light atoms such as hydrogen, carbon, oxygen, nitrogen and fluorine, having their first energy level above 6.5 eV. For these species the photo-excitation is only possible with vacuum-ultraviolet (VUV) photons, i.e. with wavelengths shorter than 190 nm [62]. Two laser photons, with wavelengths between 200 and 305 nm, are simultaneously absorbed to induce the transition between the ground and the first excited electronic levels allowed by the selection rules. The two-photon excitation is much

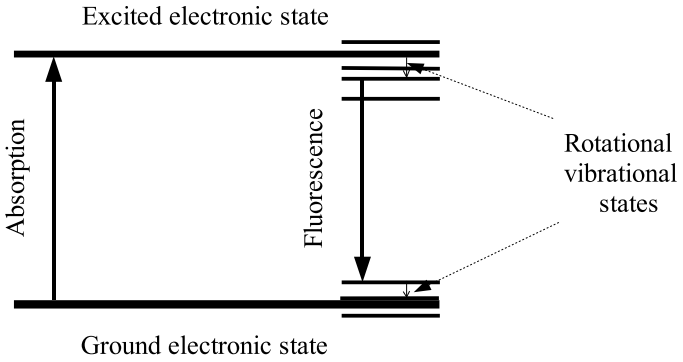


Figure 3.4: Laser Induced Fluorescence (LIF).

less efficient than the single photon excitation [63, 64].

The detection is performed by collecting the subsequent fluorescence signal, usually observed perpendicularly to the axis of the probe laser beam with a monochromator or a filter in front of a photomultiplier tube or by an optical multichannel analyzer. The TALIF signal, which is proportional to the ground-state population gives only relative values of the density and absolute measurements require an additional calibration method. Alternative calibration techniques can be made either by adding a reference of known species concentration to the plasma under consideration or by using other absolute measurement techniques with the same plasma [62].

**Absolute calibration using reference (noble) gas:** This calibration method is based on a comparative measurement at a spectrally close two-photon resonance of a noble gas of known concentration [65]. The well known two-photon resonance of atomic hydrogen have corresponding transition in krypton. In the case of excitation with sufficiently low laser intensities a depletion of the ground state population $n_1(t) \approx n_0$ as well as photo-ionization effects on the excited state population $n_2(t)$ can be neglected. The number of photons per unit volume in the fluorescence channel to an intermediate state labelled 3 is given by [64]:

$$n_F = n_0 a_{23} \frac{G^{(2)}\sigma^{(2)}}{(h\nu)^2} g(\triangle\nu) \int_0^\infty I_0^2(t)\, dt \tag{3.32}$$

where $a_{23} = (A_{23}/A_2)$ is the optical branching ratio, $G^{(2)}$ the photon static factor, $\sigma^{(2)}$ the excitation cross section, $g(\triangle\nu)$ the normalized line profile of the photon excitation and $I_0(t)$ is the spectral integrated intensity of the laser which is proportional to the laser pulse energy.

The time and spectrally integrated photomultiplier signal results by integration of $n_F$ over the two-photon resonance and the observed excitation volume taking into account the observation sensitivity:

$$S_{PMT} = \frac{\triangle\Omega}{4\pi} T\, \eta\, G\, e_0 R_L \int\int n_F(\vec{r})\, dV\, d\nu \tag{3.33}$$

since $\triangle\Omega$ is the solid angle of detection, $T$ and $\eta$ the transmission of the observation optics and the quantum efficiency of the photomultiplier at the fluorescence wavelength, respectively, $G$ the amplification of the photomultiplier, $R_L$ the load resistor and $e_0$ is the elementary charge.

The atomic density species $X$ in the presence of a reference gas $R$ is given by:

$$n_X = \gamma\left(\frac{\sigma(R) a_{23}(R) I_F(X)}{\sigma(X) a_{23}(X) I_F(R)}\right) n_R \tag{3.34}$$

where $\gamma$ represents the ratio of the detection sensitivity.

Here $I_F$ is the normalized fluorescence signal:

$$I_F = \frac{S_{PMT}}{\int\int I_0^2(t, \vec{r})\, dt\, dV} \tag{3.35}$$

**Advantages of TALIF:**

1. Non-intrusive, in-situ detection of plasma species.
2. Very high sensitivity and selectivity.
3. It has the possibility to detect both ground state and excited state species.
4. High spatial and temporal resolution, depending on focusing and laser pulse duration.
5. It can provide measurements of velocities and temperatures of species.

**Disadvantages of TALIF:**

1. Tunable UV lasers are complex in construction and are expensive.
2. More interesting minority species have very low concentration and therefore, are not easily detected despite the high sensitivity of the method.
3. At high pressure absolute calibration is problematic because of quenching.

## 3.3 Spatial resolution based on Abel inversion

The diagnostics mentioned above can be divided into two categories, space resolved techniques (e.g. Langmuir probe and laser induced Fluorescence) and line integrated (e.g. Interferometry, absorption and emission spectroscopy). The observed results of the latter techniques give the line-of-sight integrated information along the optical path of the light beams. It is helpful to obtain information on the corresponding spatial profiles [66]. It is not possible to measure directly the desired spatial distribution; this can be done by tomography. A simplest way is by using the well known Abel inversion. In case of optical emission spectroscopy (OES), an Abel inversion algorithm can be used to reconstruct a cylindrically symmetric distribution from line-of-sight integrated intensity measurements [67], which leads to line-of-sight intensity as a function of radius r (emissivity). Abel inversion has many applications in science, the most extensive use is for plasma diagnostics [68]. The asymmetric Abel inversion procedure gives an added dimension to the physical characterization of the ICP through the use of spacial emission profiles [69]. With help of a stepper-motor controlled mirror it is possible to determine the radial distribution of the rotational temperature in our ICP discharge from the lateral emission measurements.

An axisymmetric emissivity $\varepsilon(r)$ distribution can be determined by measuring the line-of-sight integrated signal $i(y)$ as shown in Fig. (3.5). The relation between the integral data $i(y)$ and the radial distribution $\varepsilon(r)$ is given by the forward Abel transform:

$$i(y) = 2\int_y^R \varepsilon(r)\frac{r}{\sqrt{r^2 - y^2}}dr \tag{3.36}$$

The emissivity can be recovered from projection data analytically by the inversion

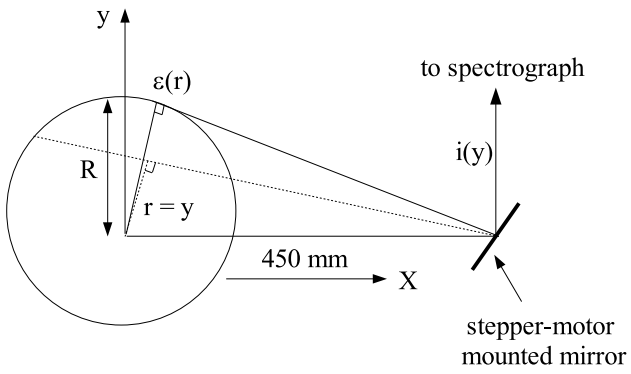


Figure 3.5: Rotatable mirror for Abel inversion.

of equation (3.36).

$$\varepsilon(r) = -\frac{1}{\pi}\int_{y}^{R}\frac{di(y)}{dy}\frac{dy}{\sqrt{r^2-y^2}} \tag{3.37}$$

This analytical integration formula has a derivative term $\frac{di(y)}{dy}$ that complicates the problem of inversion.

In practice the projection $i(y)$ is not given analytically but in the form of a certain number of measured data points, so that the inversion can not be performed directly. Various numerical methods have been developed to solve the inverse problem and several implementation procedures to perform Abel inversion are available. All methods used to solve this inversion problem require symmetry of measured data $i(y)$ and zero value at the borders of the radial distribution [70]. A powerful technique recently developed is the so-called Fourier method.

### 3.3.1 Fourier method

Unlike many other methods of numerical Abel inversion, this method does not perform the Abel inversion by working gradually from the periphery to the center but computes the calculations in one single step. This avoids the propagation of calculation or measurement errors from the periphery to the center [70]. The method was presented first by Pretzler [71] and Pretzler et al., [72] and it can be summarized as follows:

The unknown radial distribution emissivity $\varepsilon(r)$ is expanded in a series similar to a Fourier-series which is a sum of $n$ model functions $\varepsilon_n(r)$ with unknown amplitudes $A_n$:

$$\varepsilon(r) = \sum_{n=N_l}^{n=N_u} A_n \varepsilon_n(r) \tag{3.38}$$

$N_l$ and $N_u$ are the lower and the upper frequency limits. The upper limit $N_u$ should correspond to the limit of measured data, as higher frequencies just reconstruct noise with astonishing high amplitude at regions near the center. In most cases the maximum order lies between 5 and 15. For the lower limit $N_l$ it is not recommended to take the zero order, as this represents a constant added to the variation of $\varepsilon(r)$, for nearly all distributions a minimum order of 1 is convenient [70]. In our case we choose after some checks $N_l$= 1 and $N_u$= 5, since with our high resolution step-motor we had just only the possibility to measure 12 measurement points while scanning half of the discharge. The problem is the distance between the stepper-motor mounted mirror and the discharge window, that does not allow even with our high resolution stepp-motor, a high number of measurement points.

The functions $\varepsilon_n(r)$ are a set of cosine functions with:

$$\varepsilon_0(r) = 1 \tag{3.39}$$

and:

$$\varepsilon_n(r) = 1 - (-1)^n cos\frac{n\pi r}{R} \tag{3.40}$$

where $R$ is the radius of the distribution. Applying the Abel transformation to equation (3.36) we get:

$$I(y) = 2 \sum_{n=N_l}^{n=N_u} A_n I_n(y) \tag{3.41}$$

where $I_n(y)$ is an integral given by:

$$I_n(y) = \int_y^R \varepsilon_n(r) \frac{r}{\sqrt{r^2 - y^2}} dr \tag{3.42}$$

The problem here is this integrals $I_n(y)$, which include the cosine function. These integrals can be numerically pre-calculated and stored in the computer. The unknown amplitudes are determined by considering that at the $N$ points $y = y_k$, the function $I(y, A_n)$ should approximate the measured values $i(y_k)$. So the Abel transformation equation (3.41) is least square fitted to the real data measurements $i(y)$ at each measurement point. This leads to:

$$\sum_{k=1}^{N}[2\sum_{n=N_l}^{n=N_u} A_n I_n(y_k) - i(y_k)]^2 = min \tag{3.43}$$

where $N$ is the number of measured data points.

Differentiation with respect to the unknown amplitudes $A_n$ gives:

$$2\sum_{n=N_l}^{n=N_u} A_n \sum_{k=1}^{k=N} I_n(y_k)I_m(y_k) = i(y_k)I_m(y_k) \quad n_l \leq m \leq N_u \tag{3.44}$$

Evaluation of this equation system yields $A_n$. Then the emissivity (radial distribution) can be determined by applying equation (3.38).

The Fourier method has the following advantages:

1. It is derivative free since the transformation is done from the r- to the y-space.
2. There is no need to do any smoothing or any other pre-treatment of the measured data i(y).
3. The exact form of the functions $\varepsilon_n(r)$ can be adapted to the given physical conditions.
4. The method can be used as a noise-filter by choosing the minimum and the maximum order of model function $N_l$ and $N_u$ which determines the range of spacial frequencies used to build $\varepsilon(r)$.

With the help of a stepper-motor controlled mirror (1000 doupled step per cycle) see Fig. (3.5), we have the possibility to acquire the necessary data. By using such a construction it is not possible to measure parallel data points, instead we took into account the angle in calculating the axial distance $y$ while carrying out the numerical integration (3.42).

# Chapter 4

## Experimental set-up and implemented diagnostics

### 4.1 Discharge chamber geometry

The experimental setup, including the arrangement of the diagnostic optical system is shown in Fig. (4.1). The inductive coupled discharge chamber consists of a cylindrical stainless-steel vacuum vessel with an internal diameter of 220 mm and a length of 250 mm. The walls of the chamber contain two CF-100 ports used for optical emission spectroscopy, another two similar ports to allow laser diagnostics. The chamber is evacuated through a bottom CF-200 port by means of a PFEIFFER TPH170 turbomolecular pump backed by an EDWARDS two stage rotary pump. The pumps are capable of producing a base pressure of about $10^{-4}$ Pa. A gate valve is situated between the chamber and the turbo pump. The top port contains a dielectric quartz window positioned between the plasma and the coupling coil. The coupling coil is mounted to the matching unit that is positioned on top of the chamber. The inductive coil is concentric with the chamber to maintain discharge symmetry. The dielectric quartz window which is kept at atmospheric pressure, prevents direct contact between the plasma and the antenna. It has a thickness of about 4 mm below the coil area. There is no Faraday shield placed between the coil and the quartz window in our discharge.

The lower electrode inside the discharge is fixed at the center of the discharge top window on both horizontal sides by tubes connected to facing ports, these tubes are also used as a water circle for electrode cooling. The electrode is made of stainless steel, and has a diameter of 100 mm. Both the stainless-steel vessel and electrode are electrically grounded. The gap between the antenna power coupling

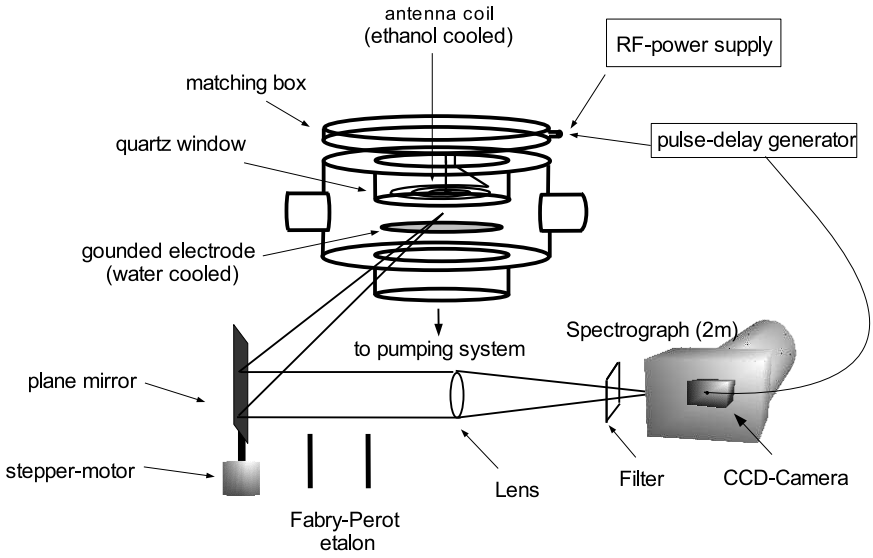


Figure 4.1: Experimental Setup.

window and the bottom stainless steel electrode is ∼33 mm. Due to the holder of the dielectric quartz window, there is a not optically accessable axial distance of about 3 mm just below this window. The optically accessable axial distance between the lower grounded electrode and the dielectric quartz window is 30 mm, as shown in Fig.(4.2). There is an additional port used for the commercial RF-compensated Smart Soft Langmuir Probe. Another 4 ports in the lower part of the vessel are used to allow access for pressure gauges and gas inlet. The working gas is 95% $H_2$ with minority species concentrations of about 3.5% Ne and 1.5% Kr flowing through one of the lower ports to the discharge body. This mixing of these constituents is used in order to determine the degree of dissociation. The working gas is fed through a Tylan gas (mass) flow controller, which has a maximum range of 100 sccm Hydrogen gives a maximum pressure of about 75 Pa. The discharge pressure is monitored by EDWARDS wide range gauge and a capacitive Barocel pressure gauge.

## 4.2 Planar coil construction

The RF electromagnetic field is induced by a spiral planar antenna coil of five-

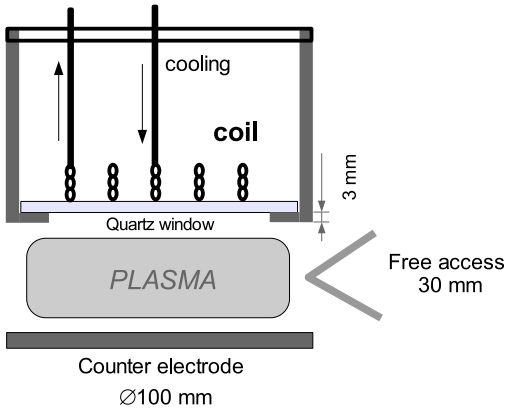


Figure 4.2: Discharge details.

turns. The five turn coil is made of a 3 mm thick and 12 mm wide copper strip with an outer diameter of 80 mm and 4 mm spacing between turns. The coil is about 700 mm long and it is cooled with ethanol. The ethanol-cooled copper tubing antenna coil used for the coupling is positioned above and at the centre of the dielectric quartz window which is located in the midplane of the discharge chamber. The central winding of the exciting coil is powered through a matching network by an RF power supply source, while the outer winding is grounded.

## 4.3 Power supply and coupling circuit

The source used during this work is powered at 13.56 MHz using an ENI-OEM-12A type radio frequency power generator. This RF-power supply can give away a maximum forward power of 1400 Watts. Because of the thermal effect the power used during the experiments has a maximum value of 500 Watt. The forward power $P_{for}$ and reflected power $P_{ref}$ are measured directly from the power meter incorporated in the power supply. The values of the reflected power in our inductively coupled plasma discharge vary from the capacitive to the inductive mode, and are dependent on the power transmitted to the discharge. The matching network was adjusted to have the minimum reflected power for each plasma condition by monitoring with the RF power meter. A steady-state discharge is obtained with reflected power of about 20 Watt in the capacitive mode. This

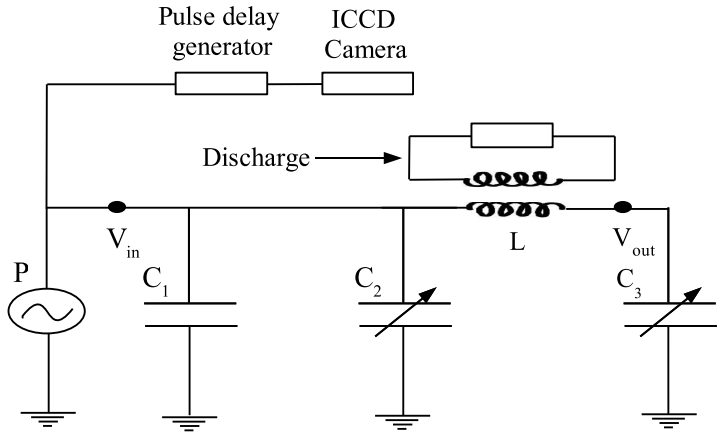


Figure 4.3: The circuit diagram showing the power supply P, P-matching network with capacitors $C_1$= 600 pF, $C_2$= 10 -1000 pF and $C_3$= 5 - 500 pF, inductive coil and the plasma discharge.

reflected power decreases with increasing the transmitted power until it reaches zero Watt in the inductive mode. The input power $p$ considered was recorded as the difference between the forward and the reflected power $P = P_{for} - P_{ref}$ as read from the power supply meter.

The RF-power is fed to the antenna through a P-type matching network. Our matching network consists of a fixed capacitor $C_1 = 600$ pF, a variable load capacitor $C_2$ in the range of 10-1000 pF and a tunable series resonant capacitor $C_3$ in the range of 5-500 pF. The circuit diagram is shown in Fig. (4.3). The antenna has an inductance high enough to replace the inductor of a conventional p-type matching unit. The matching network is connected directly to the coil and is placed as close as possible to the inductive discharge to minimise the losses. Maximum power transfer into the plasma could be obtained by adjusting the values of the variable capacitors to match the 50 Ω output resistance of the power supply to the inductive coil and in this case the power transfer from the radio frequency generator to the discharge is at peak efficiency while the reflected RF-power is minimized.

Two voltage probes (Tektronix P6015A, 1000 x 3.0 pF) with 100 MΩ impedance are connected directly at the input and the output positions of the matching unit

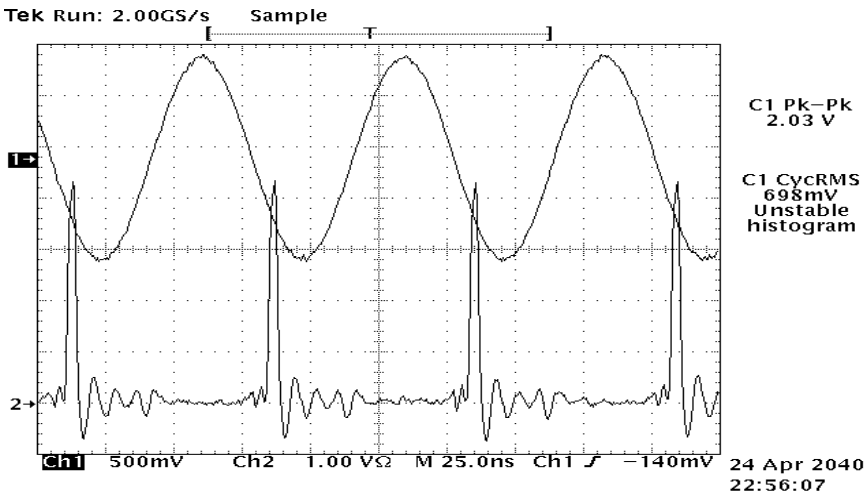


Figure 4.4: Camera gate.

to measure the input (to the matching) peak to peak voltage $V_{in(P_k-P_k)}$ and the output (from the matching) peak to peak voltage $V_{out(P_k-P_k)}$. The input and the output signals measured by the voltage probes are displayed and recorded on a four channel digitizing Tektronix TDS 640 oscilloscope, 500 MHz with a 2 GS/ s sampling rate.

## 4.4 Implemented diagnostics

### 4.4.1 Optical Emission Spectroscopy Equipment

The light emitted from the inductive discharge is imaged with a combination of a rotatable plane mirror and one lens (f = 350 mm) onto the entrance slit of the spectrograph as shown in Fig. (4.1). Using such a rotatable mirror, controlled by a stepper-motor (1000 double steps per cycle) enables us to do lateral emission scans. Dealing with these lateral measurements by means of Abel inversion algorithm, we have the possibility to check the radial homogeneity of the discharge and to acquire the radial rotational temperature results.

The light collected by the optical system is dispersed by the diffraction grating system. Our diffraction grating system consists of a 2m-spectrograph (Jenoptik PGS 2) with a diffraction grating of 1302 grooves $mm^{-1}$. This diffraction grating

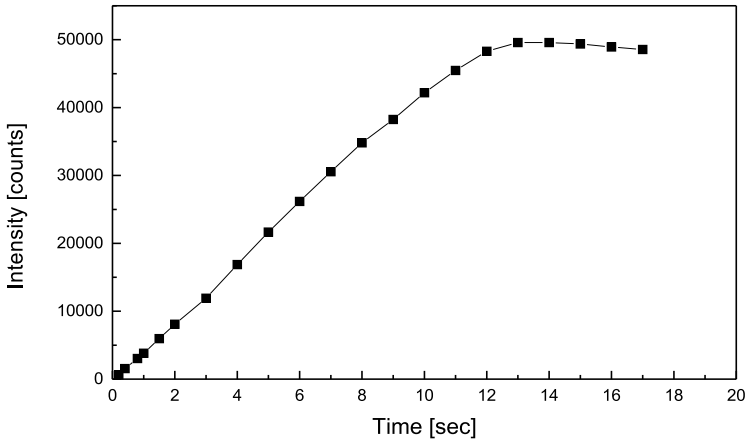


Figure 4.5: Linearity of the ICCD camera.

has an inverse dispersion of 0.34 nm $mm^{-1}$ at 600 nm.

A fast gated intensified charged coupled device (ICCD) camera (LaVision Picostar HR) with an active image array of about 4.5 nm (13.2 mm $\times$ 8.8 mm, 576 $\times$ 384 pixel) is used as detector during this work. The camera is mounted in the focal plane of the spectrograph. Gateable cameras allow time-resolved measurements by locking the gate to a fixed phase position within the RF cycle [11]. The intensities integrated over 25 time windows for a complete RF-cycle of 74 ns with gate time of 3 ns. A spectrum of about 4.5 nm on the CCD ship and a spectral resolution of 0.03 nm with slit width of 50 $\mu m$ could be obtained. A variable delay between the fixed phase and the gate allows one to cover the complete RF cycle as shown in Fig. (4.4). The output window of image intensifier of the camera is a fiber optical window, where the most effective light transmission from the image intensifier to the CCD can be realised. The result of the repeated collisions inside MCP is an electron gain up to $10^3$ [51]. The applied ICCD is a full frame type (PicoStar F) camera, by which less intense emission lines can be observed and monitored with RF time resolution. The repetition rate using such special camera, can be as high as 13.56 MHz so that each individual RF cycle can be utilized. This reduces measurement times by a factor of 1000 as compared to standard ICCD cameras. The linearity of the ICCD has been checked and

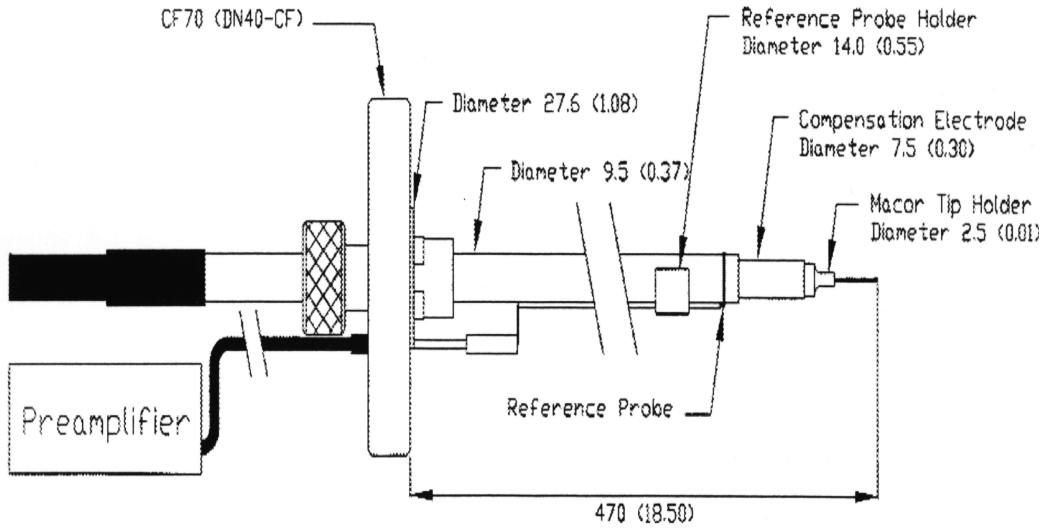


Figure 4.6: Smart soft Langmuir probe construction.

the result is shown in Fig. (4.5). It is clear from the figure that the linearity is obtained only up to about 45000 counts, beyond these values, the linearity can not be warranted and a saturation in the curve is obtained. All measurements during this work has been done with short integration times at which much lower intensities clearly below 40000 counts are obtained.

For absolute line intensity measurements needed to obtain absolute values for the population densities, an absolute calibration of the detection system has been performed with a tungsten ribbon lamp [16]. This calibration is used in calculations during this work.

### 4.4.2 Fabry-Perot Interferometer set-up

The Doppler-broadened linewidth meets about $\Delta\lambda_{FWHM} \approx 5\,pm$ at a gas temperature of 300 K. This value exceeds by far the resolution of the installed 2-m spectrograph/ camera combination. Therefore the optical system was extended for some measurements by installing a Fabry-Perot interferometer (FPI; Burleigh RC-150) within the optical path in front of the entrance slit of the spectrograph. The plasma discharge is considered to be the light source for the FPI, which is located in the focal plane of a collimating lens. The used FPI etalon is a piezo-electric

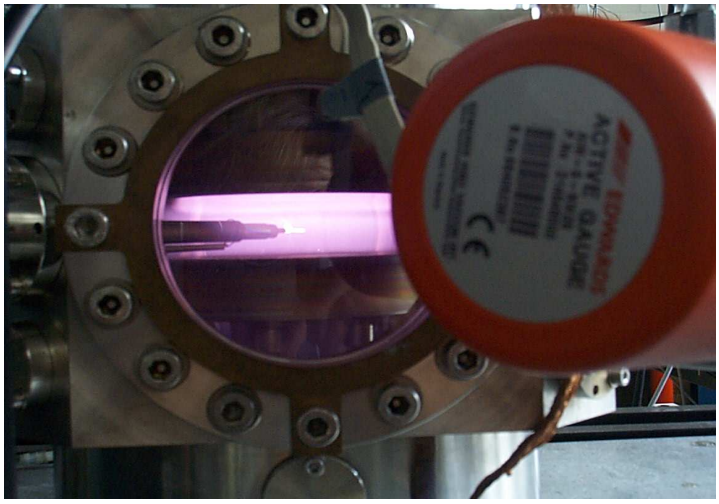

Figure 4.7: A picture of the Smart Soft Langmuir Probe during an experiment.

scanning type with a broad band coating for red wavelengths. The interferometer is equipped with two plane plates of 50 mm diameter mirrors and an adjustable cavity spacing of about 12 mm measured mechanically. The measurements are carried out with Fabry Perot interferometer (FPI) in combination with two-meter spectrograph, since the light transmitted from FPI is focused using a lens ( 45 cm focal length) on the entrance slit of the spectrograph. The spectrograph is used as a wavelength pre-selector because of the very narrow free spectral range of the Fabry-Perot interferometer and provides the high parallelism of the light required for a high finesse [56]. The slit width of the spectrograph is set, such that the linewidth of the spectrograph matches the free spectral width of the Fabry-Perot interferometer.

### 4.4.3 The Smart Soft Langmuir Probe System

A Smart Soft Langmuir Probe (SSLP) made by Scientific Systems Inc. is used during this work. The active part of the Langmuir probe is a short, thin, cylindrical tungsten wire of 5 mm length and 0.06 mm radius that is inserted into the plasma as shown in Fig. (4.6). The probe tip lies vertically 12 mm above the lower electrode inside the discharge. The tip is connected to the acquisition unit via a coaxial cable which is shielded from the plasma by a ceramic shaft. The

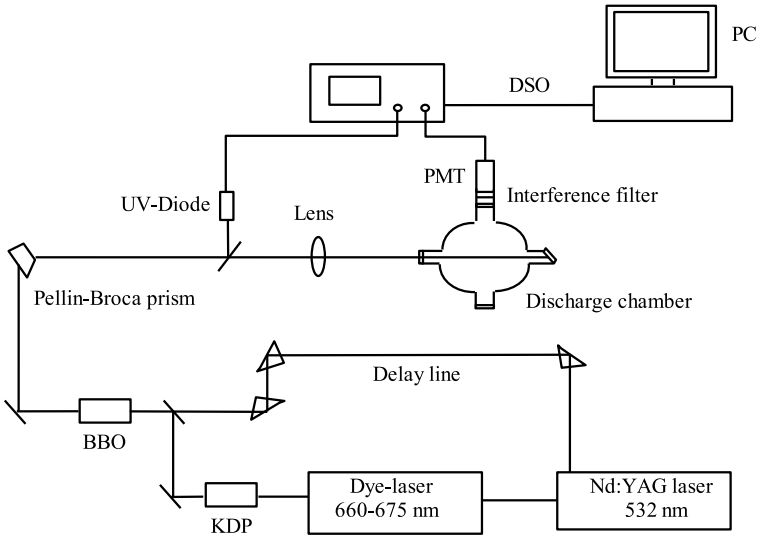


Figure 4.8: Set-up for two photon laser induced fluorescence.

flange on the probe is standard conflat CF70. A mounting kit including copper gaskets and mounting screws is supplied with the system. A compensation electrode in contact with the plasma is capacitively coupled to the probe tip. The large capacitance and low impedance of this electrode reduces the probe to plasma sheath. Air inlet and exhaust tubing is built into the Langmuir probe system. Air cooling should be used at all times during performing the probe measurements. A reference probe, which tracks and compensates for any low frequency DC shift in the plasma potential is added [60]. A computer-controlled stepper motor (housed with the Smart Probe) allows the radial motion of the Smart Probe System. A photograph of the probe inside the plasma discharge, showing the glow of the probe tip during an experiment is shown in Fig. (4.7).

### 4.4.4 TALIF set-up

The radiation of Spectron SL400 dye laser system ($\lambda = 660\,to\,675\,nm$) is pumped by a frequency-doubled Spectron SL800 Nd:Yag laser ($\lambda = 532\,nm$), as shown in Fig. (4.8). Frequency-doupling of the dye gives radiation in the blue region at $\lambda = 330\,nm$ using a KDP-crystal. This frequency-doubled dye laser output is mixing with the second harmonic of the Nd:Yag radiation in a BBO-crystal

to give the UV light at $\lambda = 205\,nm$, which is necessary for the atomic hydrogen measurements. The dye is a mixture of Pyridine 1 and DCM dissolved in propylene carbonate. A maximum UV energy of 160 $\mu J$ with a pulse duration of 10 ns and a repetition rate of 10 Hz are obtained. The UV radiation is singled-out with a Pellin-Broca prism and is focused with a suprasil lens ($f = 30\,cm$) into the ICP vessel. Fluorescence radiation is detected transverse to the laser beam using a Hamamatsu R 955 photomultiplier tube (PMT) equipped with interference $H_\alpha(\lambda = 656\,nm)$ and krypton ($\lambda = 826.3\,nm$) filters. The PMT output is shown on a digitizing oscilloscope. The laser energy is monitored with a fast UV diode on the same digitizing oscilloscope, which is connected to a PC.

# Chapter 5

## Operation characteristics

### 5.1 Introduction

Inductively coupled plasmas (ICPs) are exhibit mode transitions between a capacitively coupled mode (E-mode) and an inductively coupled mode (H-mode). The transition between the E-mode and the H-mode is one of the most important characteristic features of ICPs. This thesis is interested in diagnostics of the ICP discharge and the interest of this chapter is to check the applicability of OES to follow the transition phenomena under our conditions to see whether we have the possibility to diagnose these discharges modes. It is also important to investigate under which conditions the discharge is running in the E- or H-mode. The determination of some important plasma parameters in different discharge modes is also of interest. The transition phenomena from the E-mode to the H-mode show a hysteresis behavior in some discharges. Hysteresis phenomena are also an important topic of investigation.

### 5.2 Transition from the capacitive to the inductive-mode

Low-pressure electrodeless RF discharges with high density are assumed to be stable, producing relatively quiescent glow discharges [73]. They exhibit two distinct modes of operation: as the RF power (or antenna current) is increased from zero, the gas first breaks down into a weak capacitively coupled electrostatic mode (E-mode), and evolves gradually into the inductive mode (H- mode). A number of experiments were performed to show whether the discharge is maintained by the axial electrostatic or the azimuthal electromagnetic field of the inductor coil

[13]. In low pressure argon discharges, the mode change can be hard to observe experimentally, but in some other discharges working with complex gases such as $CF_4, O_2, H_2$ and $He$, the E-mode may not only be easy to observe, it may actually be hard to drive the plasma in the H-mode. The studies of this transition phenomenon were performed in different ways: by studying electrical properties (V-I characteristic, power transfer efficiency, electron energy distribution, etc.) [29, 30, 74, 75, 76], by optical emission spectroscopy [77] and by computerized tomography (CT) [78].

It is established that in the E-mode the power dissipated in the discharge is low, reflection of RF-power is high and there is no threshold for operation. In addition, this E-mode is characterized by a low electron density, very high RF-coil voltages and a glow localized near the coil. The energy distribution is clearly non-equilibrium. The discharge is maintained by the electrostatic field which is larger than the induced electrical field. The E-mode discharge in this configuration is not completely understood, but it is generally thought to be driven by some combination of capacitive (E-field) coupling from the high RF voltage across the coil and very weak inductive coupling between the coil current and the plasma. With increasing RF power and above a certain threshold current high enough to ignite the inductive plasma mode of operation, the discharge switches abruptly to an inductively coupled magnetic mode (H-mode) where inductive power deposition dominates. An H-mode plasma requires an induced electric field high enough to support sufficient ionization to balance the particle loss rate on the chamber walls [75]. In the H-mode there are exactly the opposite characteristics as compared to the E-mode, since high power is dissipated with relatively low reflection, it occurs with a relatively large threshold (of the coil current or power). In this mode there is a sudden increase of both the plasma luminosity (much brighter glow) and the electron density. It was mentioned that the H-mode occurs, if the plasma has an adequate electron density, and the E-mode is obtained, if the electron density is not high enough to sustain the H-mode. It was found by optical emission spectroscopy together with computerized tomography (CT) [78] that the radial and azimuthal CT images of the E-mode are quite different from those of the H-mode. The E-mode structures show clearly the presence of capacitive coupling, while the H-mode structures correspond to the predicted induced fields.

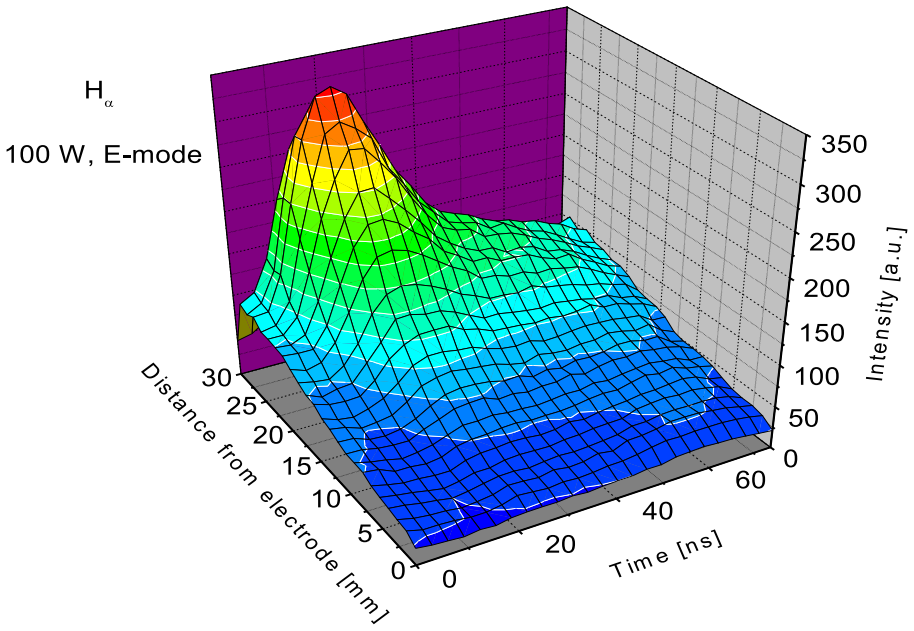


Figure 5.1: Time resolved $H_\alpha$ emission in the E-mode at 25 Pa $H_2$ and 100 W.

**Time and axial dependencies of emission:** In a capacitively coupled (CCRF) hydrogen discharge the electron distribution function is modulated with the RF frequency in a characteristic way. Our optical detection system is fast enough to follow this time dependence [11]. This modulation of the emitted radiation is observed in the inductively coupled hydrogen plasma (ICP). Our measurements demonstrated that the (OES) intensities undergo considerable changes during the E-↔H-mode transitions. In general, there is a stationary mixed mode between these stable E- and H-mode, we call it the transition mode (T-mode). This transition-mode (T-mode) is observed under certain conditions of power closely (about 10 W) below the power required to ignite completely an inductive mode discharge at a defined pressure. A discrimination between E-mode, T-mode or H-mode operation is possible from the temporal structure of the emission and by intensity.

The E-mode is characterized by the evolution of one emission maximum per RF-cycle ($t_{RF} = 74ns$) as shown from Fig. (5.1), while in the H-mode discharge two emission maxima per RF-cycle are clearly discriminable as shown in Fig. (5.3). On

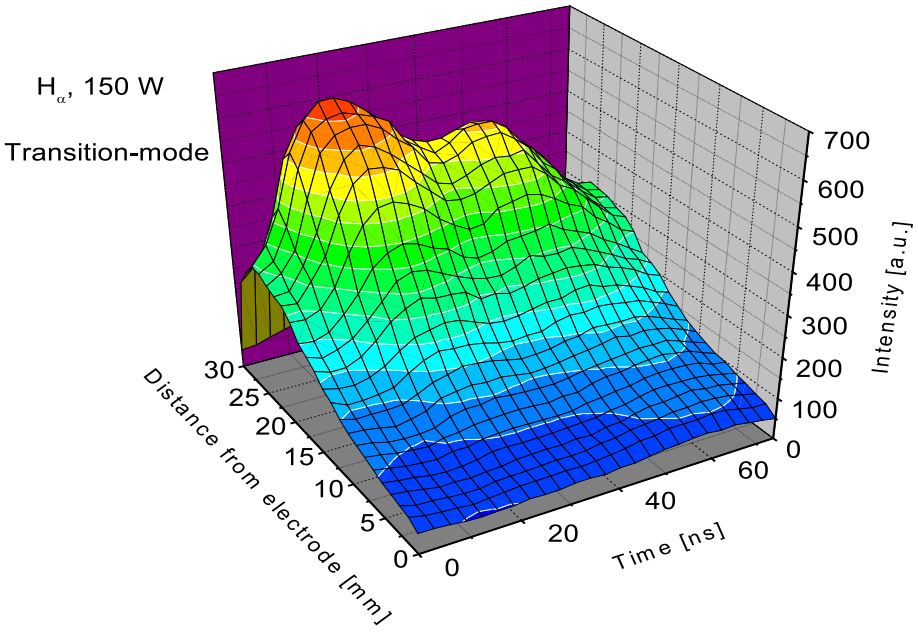


Figure 5.2: Time resolved $H_\alpha$ emission in the Transition-mode at 25 Pa $H_2$ and 150 W.

the other hand during the transition-mode the second emission maximum starts to built up which results in a broadening in the capacitive emission maximum (Fig. 5.2). The single maximum of the E-mode is attributed to the fast electrons expelled by the sheath building up near the coil once in every excitation cycle. In the H-mode the observed two emission maxima are brought about by the currents in the discharge induced twice per period. The T-mode is an intermediate mode produced from mixing of the CCRF and ICP excitation, i.e. the discharge in this case is maintained by both the electrostatic and the electromagnetic field of the excitation coil. Furthermore, the E- mode has a faint optical emission which is a factor of two of the intensity in the T-mode. The H-mode emission intensity is about 2 orders of magnitude higher than these values of the low density E-mode.

It is clear from these figures that the first emission maximum is always located at the same time position independent of the ignition mode. The second emission maximum in the transition mode starts to appear at about $\triangle t = 30\,ns$ ($\triangle t$ is the time difference between the two emission maximum), moreover it reaches a time

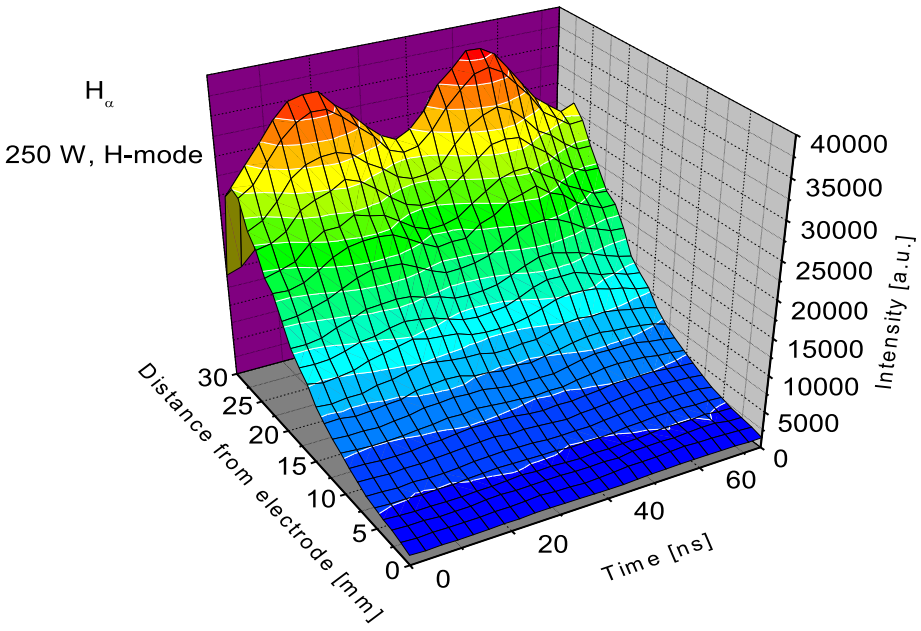


Figure 5.3: Time resolved $H_\alpha$ emission in the H-mode at 25 Pa $H_2$ and 250 W.

position around $\triangle t = 36\,ns$ in the H-mode. The spatial intensity distribution of the capacitive, transition and inductive mode operations is characterized by very low emission intensity close to the grounded electrode which is cooled with water. A gradual increase of the emission intensity is clearly observed from the grounded electrode until the emission maximum is reached.

**Axial position of emission maximum and amplitude of temporal emission modulation:** The position of the maximum emission and the intensity modulation in case of $H_\alpha$ as a function of pressure at 100 W and 350 W are shown in Fig. (5.4 a and b). At low power (100 W) the discharge is ignited in the capacitive mode for different pressures. With 10 Pa the emission maximum is located at about 9 mm below the upper observation limit (15 mm below the antenna coil). By increasing the pressure, the position of this emission maximum moves closer to the antenna coil until it reaches a distance of about 2 mm below the upper observation limit at 60 Pa. This means that the penetration depth of the external electrostatic field at high pressure is localized close to the excitation coil. The

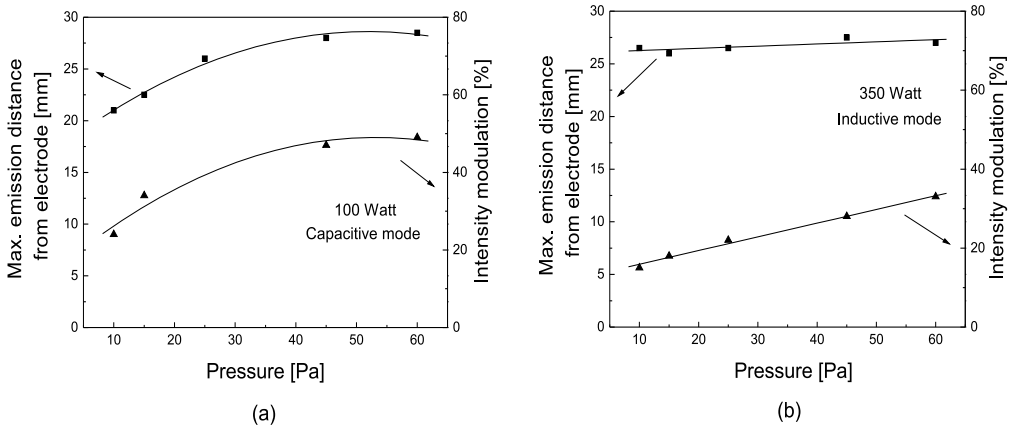


Figure 5.4: Position of maximum $H_\alpha$ emission and $H_\alpha$ emission modulation as function of $H_2$ pressure for (a) 100 W and (b) 350 W for different pressure.

emission intensity modulation obtained at the same power 100 W, increases with pressure. A maximum modulation within the range of 50 % is reached for higher pressures at 45 and 60 Pa.

At high power (350 W), the discharge is always working in the H-mode within our pressure conditions. The position of the emission maximum at any pressure variation is always located at approximately 3 mm below the upper observation limit. A steep increase in the emission intensity modulation is observed with rising pressure. A modulation of about 20 % is obtained at 25 Pa, meanwhile an emission modulation maximum of about 33 % is reached at 60 Pa.

Comparing both emission maximum position and emission modulation in both E- and H-mode, it is clear that at low pressures the position of maximum emission in the H-mode is obtained more close to the inductive coil than in the E-mode. At high pressure (45 and 60 Pa) the position of maximum emission more or less similar in both modes. The emission modulation has always higher values in E-mode than in H-mode.

**Parameter variations:** The power and pressure variations of the maximum $H_\alpha$ emission intensity is shown in Fig. (5.5 a and b). The emission intensity rises with increasing power and changes abruptly to much higher values (up to 2 orders

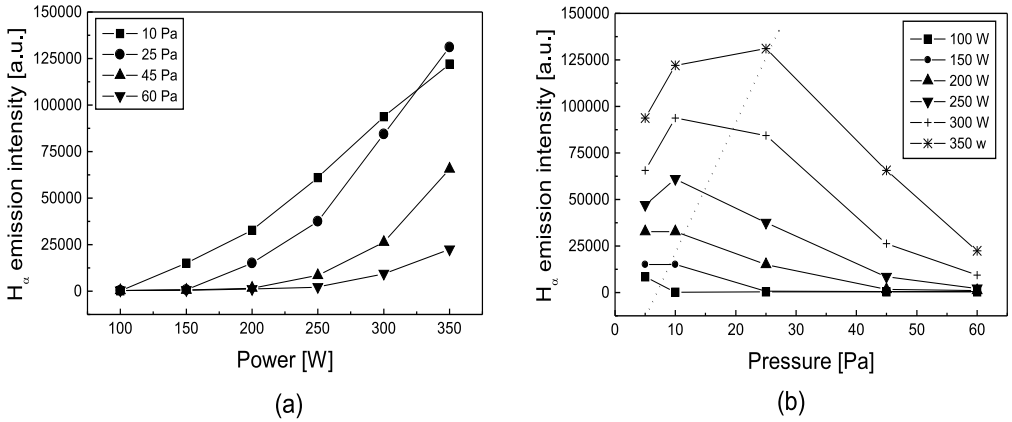


Figure 5.5: $H_\alpha$ emission intensity as a function of both power and pressure.

of magnitude) when the discharge changes to the H-mode. The power required to support an inductive mode increases with increasing pressure. The inductive mode is reached with 10, 25, 45 and 60 Pa at powers within the range of about 150 to 300 W. After achieving the inductive mode, a gradual increase of the emission intensity is obtained with rising power. It is also clear from the same figure that the emission intensities have higher values at lower pressures (as in case of 10 Pa in comparison with results at 60 Pa for the whole range of power).

The effect of pressure can be discussed as follows: We can clearly notice that the emission intensity increases with increasing the pressure from 5 to 10 Pa at different power except for 100 W. At 5 Pa, the discharge is already ignited in the high density inductive mode (H-mode) and with increasing of pressure it switches to the lower density mode (E-mode) passing through the transition mode (T-mode). Hence a decrease in maximum emission intensity must be obtained as a result of the mode transition. With increasing of power it looks that there are slightly shifted emission maxima obtained at different pressures. A decrease of the emission intensities with pressure are obtained after emission maxima are reached. It has to be clear for example that the transition from the high density inductive mode to the lower density modes (transition and capacitive modes) starts above

25 Pa at 350 W. The increase in the emission intensity can be attributed to an increase in the dissociation rate, i.e. much excitation processes inside the discharge leads to this increase of emission intensity. Of course these processes increases as a result of power. The reason for decrease of emission intensities afterwards is due to the discharge transition from the higher to the lower density modes. Hence a change in the electron energy distribution function is acquired during these mode transition results in a decrease in the emission intensity.

## 5.3 Capacitive effects at high pressure

From the viewpoint of material processing, the electrostatic coupling generated in an ICP source is unfavorable (because of capacitive problems) and often causes serious impurity problems because it gives rise to sputtering of material in the vicinity of the coil [79]. Capacitive currents are usually undesirable except for the initial gas breakdown as mentioned in Chapter 2. The capacitive currents are caused by time-varying electric charges on the coil, which generate a strong capacitive electric sheath at the dielectric window next to the inductive coil [26].

At low power and high pressure, the capacitive effects in our discharges are much more pronounced. These effects can be discussed by comparison of emission intensity of $H_\alpha$ and the Fulcher Q[1] lines shown in Fig. (5.6 a and b). In case of $H_\alpha$ two structures (I, II) appear. These structures have been observed in a pure capacitively coupled (CCRF) discharge measurements [80]. The first emission maximum (structure I) is obtained in all discharge modes (E-, T- and H-modes) at the same time position as mentioned before. This structure is related to the sheath expansion, in which the electrons is moving to the plasma bulk. The first emission maximum is followed by another (structure II) at about $\triangle t = 36\,ns$ as in CCRF discharge. Typically, the second emission maximum is not as pronounced as the first one but it expands to fill the distance until the electrode is reached. Comparing this structure to the CCRF results, it is related to fast secondary electrons created by ion impact. In CCRF hydrogen discharge two other structures have been observed, one of these structures is caused by a field reversal across the space charge sheath and the other is related to fast hydrogen atoms created at the electrode surface by the impact of hydrogen ions. Since these structures were very close to the powered electrode in capacitive discharge, there was no opportunity to check this in ICP discharge. The reason is that, there is a not optically accessable

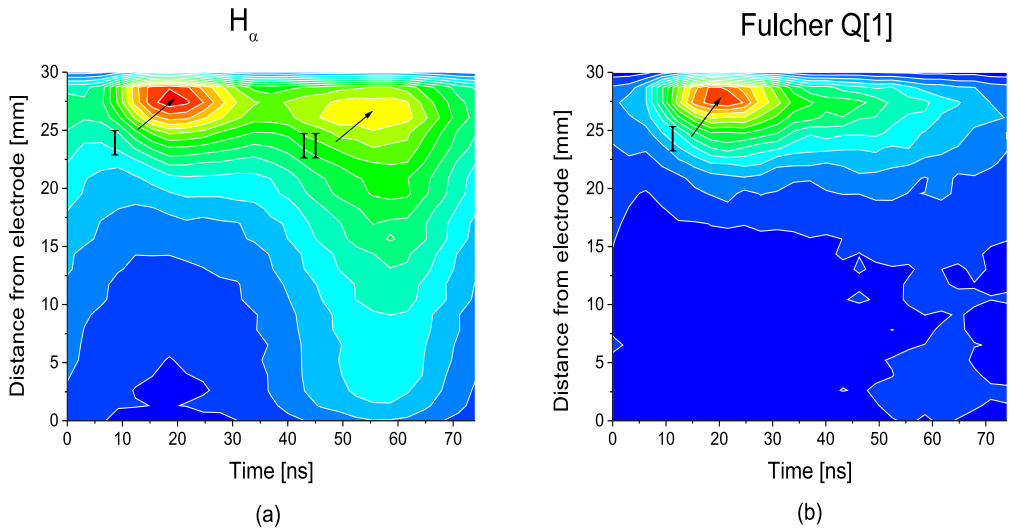


Figure 5.6: Time resolved emission intensity of (a) $H_\alpha$ and (b) Fulcher Q[1] lines at 150 W and 60 Pa.

axial distance of about 3 mm just below the dielectric window of 4 mm thickness.

In comparison with the emission obtained from the molecular hydrogen line Fulcher Q[1], the second emission maximum (structure II) does not appear in accordance with CCRF results [80].

## 5.4 Smart Probe measurements

An interesting aspect of the mode transition in an inductively coupled plasma (ICP) is the evolution of the plasma during the transition. Kortshagen et al [77] proposed that a stable magnetic H-mode plasma can only be achieved, if the applied power and antenna current exceed a critical limit. They also described qualitatively the dynamics of the E to H transition as follows: " Starting with an E-mode plasma and increasing the antenna current (power applied), a value is reached where the induced electric field can produce ionization. At this point the ionization rate suddenly becomes higher than the loss rate, power balance no longer holds and $n_e$ starts to increase. Since the effectiveness of the power deposition increases linearly with $n_e$ (at low $n_e$), a higher amount of power is

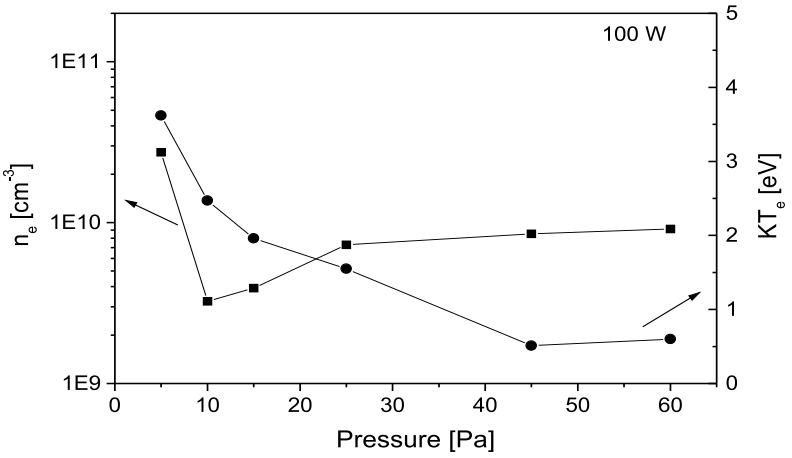


Figure 5.7: Smart Soft Probe results of electron density and temperature at 100 W.

absorbed with increasing $n_e$, and the electron density will continue to rise. At a high enough $n_e$ the skin effect becomes significant. The inductively absorbed power increases more slowly than $n_e$ and a new steady-state H-mode discharge, satisfying the power balance, is finally reached".

### 5.4.1 Electron density and temperature measurements

In case of CCRF discharges the plasma density is proportional to the square root of the absorbed power, while in case of ICP discharges the electron density is linear with power. Conventional non-magnetized CCRF discharges are limited to a density of $10^{10}cm^{-3}$ where the density limitations in the ICP are of the order of $10^{12}cm^{-3}$. For efficient inductive discharge operation a plasma density in the order of $10^{11}$- $10^{12}cm^{-3}$ is obtained which is still typically 10 times higher than for capacitive RF discharges in the same pressure range ($\sim 1Pa$) [1].

In comparison with our results, the probe measurements at different power and pressure were performed to investigate quantitatively the behaviour of the electron density ($n_e$), electron temperature ($T_e$) and electron energy distribution function (EEDF) in different discharge modes. The smart soft Langmuir probe is positioned at the center of the discharge and axially at about 13 mm above the electrode. Before using the probe for a measurement, the probe tip was cleaned by drawing electron current sufficient to have the tip glow bright red. To begin

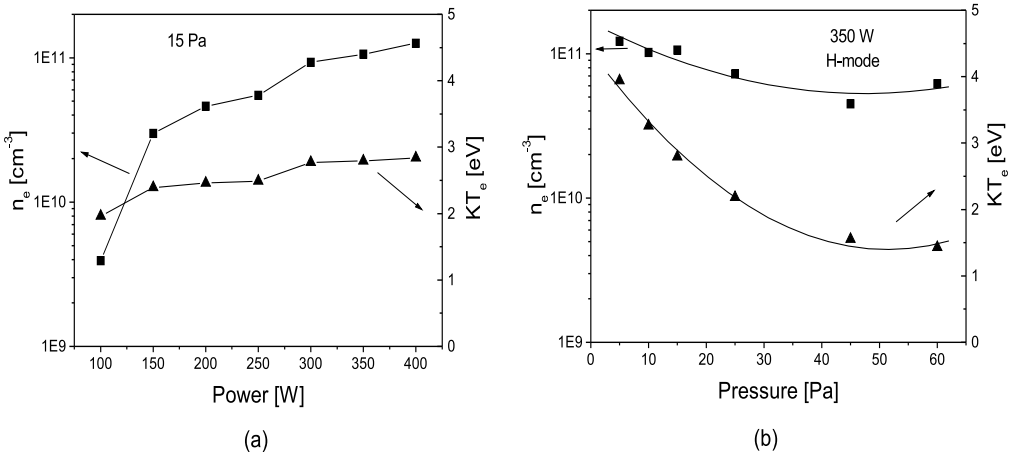


Figure 5.8: Smart soft probe results of electron density and temperature as a function of (a) power at 15 Pa and (b) pressure at 350 W.

with, the electron density $n_e$ and temperature $T_e$ are measured by the smart soft Langmuir probe system at 100 W power and different pressure. The results are shown in Fig. (5.7). It is clear from this figure, that the discharge switches from the high density H-mode to the lower density modes above 5 Pa as proved by optical emission spectroscopy. The discharge at this pressure condition (5 Pa) has a high electron density in the range of $5 \times 10^{10}\, cm^{-3}$ and an electron temperature of about 3.5 eV. With increasing the pressure, the discharge switches to an intermediate transition mode (T-mode) at 10 Pa. The plasma during this mode is characterized by a lower electron density of about $3 \times 10^{9}\, cm^{-3}$. For higher pressure of more than 10 Pa, the capacitive mode is reached with a little higher electron density. With increasing of pressure the electron density is increased up to about $8 \times 10^{9}\, cm^{-3}$ at 60 Pa. The electron temperature decreases by increasing the pressure until the capacitive mode is reached at which an electron temperature of about 0.5 eV is obtained.

The Smart soft probe results obtained at 15 Pa and different powers are shown in Fig. (5.8 a). At 100 W, the discharge works in E-mode. In this mode, an electron density of about $10^{9} cm^{-3}$ and electron temperature of about 2 eV are obtained. As the power is increased, the plasma undergoes a transition to the

high density H-mode. The transition mode was not observed within our power variations. It is expected that it might be observed at about 130 W. An increase in electron density is clearly observable with rising power. An electron density of about $10^{11} cm^{-3}$ is obtained at more than 300 W. A steep increase in electron temperature from 2.3 eV to about 2.8 eV is obtained with increasing of power from 150 to 400 W.

The behavior of plasma parameters at high power (350 W) and various pressures is shown in Fig. (5.8 b), the discharge in this case is always working in the inductive mode. We can clearly see that the electron density is within $10^{11}\, cm^{-3}$. A slight decrease in electron density is obtained by rising of pressure. A stronger decrease in the values of the electron temperature with increasing pressure is noticed. The electron temperature has a value of about 4 eV at 5 Pa, and it decreases to reach 1.5 eV at the highest pressure value.

### 5.4.2 Electron energy distribution function (EEDF)

EEDFs measured by the Smart Soft Probe at 25 Pa at different discharge modes are shown in Fig. (5.9). Discharge modes are defined by OES measurements as mentioned before at the beginning of this chapter. At 25 Pa the discharge operates in the capacitive, transition and inductive modes at powers of 100, 150 and 200 respectively. Here it is clear that there is an EEDF shape change for different discharge modes in accordance with Cunge et al [75]. Many authors found intermediate distribution functions $f(E)$ between a Maxwellian distribution shape, i.e. $f(E) \sim exp - (E/kT)$ and a Druyvesteyn distribution shape with $f(E) \sim exp - (E/kT)^2$ [81].

The shape of the EEDF changes in our measurements during the transition. A mode transition with a switch from a Druyvesteyn-like distribution (depleted in the high energy region) in the pure capacitive mode (E-mode) to a Maxwellian-like distribution in the magnetic H-mode is noticed. The Druyvesteyn-like distribution shape stands also for the intermediate power (150 W) at which the transition T-mode is obtained. It is thought here that the gradual decrease in both the emission intensity and in the electron temperature shown in Figs. (5.5 b and 5.7) respectively, i.e. the increase in the plasma potential during E-mode, can be attributed to the change of the electron energy distribution function. Turner and Lieberman [82] mentioned that the energy supplied to support an electron ion pair

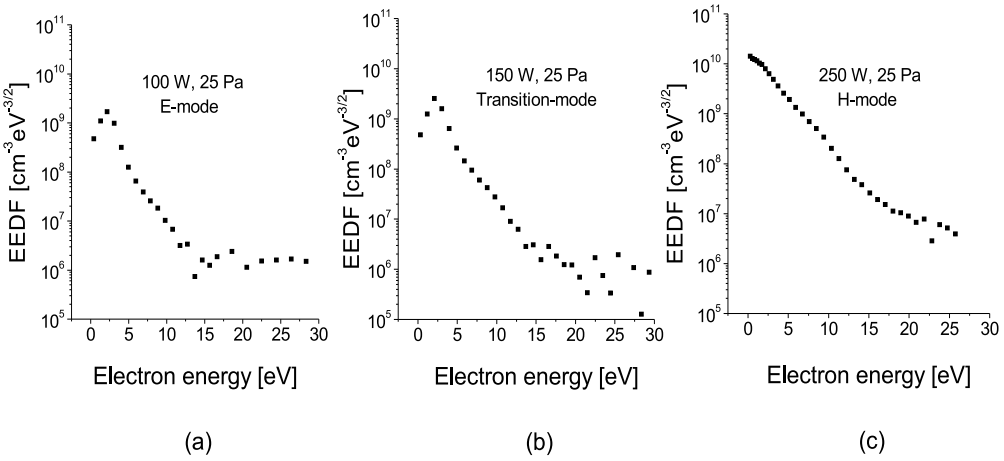


Figure 5.9: EEDF measurements at 25 Pa and different powers.

within its lifetime, depends on the EEDF shape. Consequently the change in the EEDF will lead to a nonlinearity of the dissipated power ($P_{dis}$) and so contribute to the hysteresis in the transition. The transition phenomena will be discussed in the next section in some detail.

## 5.5 The hysteresis in the system

As mentioned before, a common observation in the ICP discharges is a mode jump from the low input power (low density) mode to the high input power (high density) H-mode. The transition phenomena between E- and H-modes have frequently been described in literature to be abrupt and exhibit a pronounced hysteresis [74, 76, 77, 78]. Due to the high electron density of the ICP, its kinetics are quite different from the CCRF plasma, and thus when power is reduced hysteresis occurs [78]. When operating with electropositive gases, the transition between E- and H-mode occurs at a given power, and the discharge is always stable. In contrast, when operating with electronegative gases like hydrogen the transition is usually unstable, and a wide range of power exists where the discharge oscillates between E- and H-modes [83, 84, 85]. The transition between these modes exhibits a hysteresis, i.e. the E- to H-mode transition (while increasing power) occurs at a

different power than the reverse H- to E-mode transition (while decreasing power) [75]. As a result, an antenna current $i_1$ required for the transition from E- to H-mode is different from the current $i_2$ at which the reverse transition occurs. It is also possible to say that the discharge is bi-stable, i.e. that there is a range of coil currents which can support both modes [82]. The nonlinear behaviour of the power balance equation was shown to cause the hysteresis. For a stable E or H discharge to exist, the power absorbed by the electrons, $P_{abs}$, must identically balance the power dissipated $P_{dis}$:

$$P_{abs}(n_e) = P_{dis}(n_e) \tag{5.1}$$

To obtain hysteresis, it is necessary to introduce a nonlinearity either in $P_{dis}$ or in $P_{abs}$ (or both) at low $n_e$. Nonlinearity in absorbed power results from various circuit effects, including power loss in the matching unit. Nonlinearity in dissipated power can arise from changes in the efficiency of plasma production when, for example, multistep ionization is included [75]. Nonlinearity in $P_{dis}$ and $P_{abs}$ means deviation from their linear behaviour. A range of unstable intermediate operating points exists between the stable E- and H-modes. The intermediate region could be operated in E- or H-mode, depending on the previous history. If the input power is increased from the E-mode to the H-mode, the discharge will remain in the E-mode through the intermediate region before the transition to the H-mode. Conversely, if input power is decreased in going from the H- to the E-mode, the discharge will remain in the H-mode through the intermediate region before transition to the E-mode.

The experimental results about hysteresis found in literature have generally been obtained by increasing the RF power step-by-step, and measuring plasma parameters at those points. Such an approach has the advantage of being straightforward, but because of the discontinuous character of the E to H transition, the dynamics of the transition remains hidden. Another technique used by El-Fayoumi et al [74] and El-Fayoumi and Jones [30] consists in varying the value of the tuning capacitor in the matching network in order to change the antenna current and thus obtain the desired E to H (or H to E) transition. This has the disadvantage of changing the matching condition during the measurement.

The hysteresis in our ICP was studied by measuring the power required to sustain the plasma in the E- and H-mode at different pressures. The matching

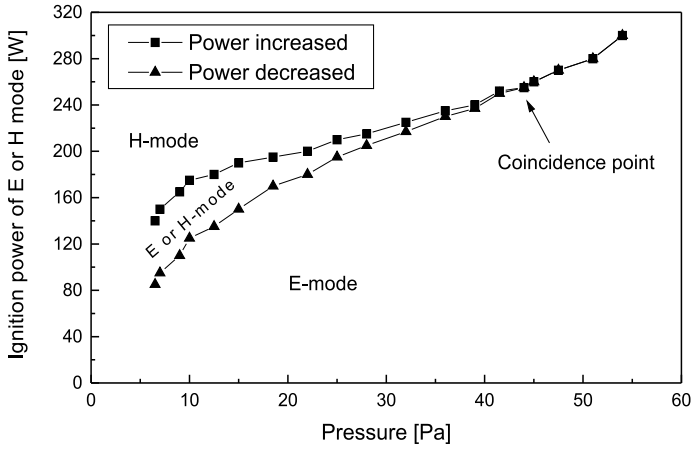


Figure 5.10: Hysteresis loop.

network was adjusted once at the beginning of the measurements to have the smallest reverse power, beginning with a defined pressure and measuring the power required to ignite the H-mode while increasing the power, then decreasing the power and measuring the power required to sustain the plasma in the E-mode. This experiment was repeated for different pressures until a maximum value of pressure (55 Pa) is reached at which we can not distinguish between the E- and H-mode (i.e. the switch from the E- to H-mode can't be seen anymore). The characteristics of the hysteresis loop is shown in Fig. (5.10).

Just by looking at the plasma brightness, it is generally possible to determine whether the plasma is operating in the E- or H-mode [75]. It is often easy to see the E-H mode change since the optical emission of the E-mode is generally very weak compared to the strong and abrupt change in emission of the H-mode. If we start with a pressure of 15 Pa and increase the power, the discharge ignites in the E-mode, characterized by relatively weak light emission. As the power is increased there is a sudden transition to the brighter H-mode at $\sim$ 190 W. When the power is then decreased, a sudden transition back to the E-mode is observed at a lower power of $\sim$ 140 W. The power difference required to sustain the H- or E-mode, i.e while increasing or decreasing power depend on the pressure. The power difference is about 50 W at lower pressures and it decreases with pressure to about 20 W at 25 Pa, further increase in pressure is followed by a decrease

in power difference until the point of coincidence is reached at about 45 Pa. At that point a "zero power difference" is obtained. The power difference still has zero values with increasing pressure until 55 Pa. At higher pressures the E- to H-transition and the H- to E- transitions are so smooth that it becomes difficult to identify, i.e. we can not distinguish between the E- and H-mode discharge since light emission appears to increase gradually with increasing of power without an abrupt change. It is clear from the hysteresis figure that the loop is wider at lower pressures. Thus the nonlinearity leading to hysteresis becomes stronger at lower pressures.

Of course, we can not distinguish by eye between the lower density modes, i.e. the transition and the capacitive modes. But we have to keep in mind as mentioned before that the transition mode is clearly defined by optical emission spectroscopy. We have to mention here that there is no instability observed in our ICP - $H_2$ discharge or at least under our operating conditions of powers and pressures, although instabilities have been observed in other electronegative gases such as $SF_6$ and $Ar/SF_6$ mixtures [85].

In conclusion, our OES diagnostic technique can be applied to follow temporally and spatially the transition phenomena. The conditions required to support different discharge modes can also be determined by OES. Measurements of the electron density and electron temperature in addition to the EEDF are obtained by the Smart Soft Langmuir Probe. These measurements are in a good agreement with the emission measurements for various discharge modes. The transition from the different discharge modes shows a hysteresis behaviour. It can be discussed just by looking at the discharge while increasing or decreasing of power. We will now focus on the spectroscopic determination of gas temperature and degree of dissociation.

# Chapter 6

## Measurements of properties of the neutrals

### 6.1 Determination of Gas Temperature

The gas temperature is one of the main characteristics of the discharge gases, it is a key parameter in calculating other discharge parameters such as particle densities and the degree of dissociation. For industrial applications the homogeneity of the discharge is of major concern for all technological applications. Gradients along the surface to be modified influence the efficiency of the processes and have to be controlled to be within specified limits. The knowledge of gas temperature distributions within the discharge and in particular close to the surface to be modified are, therefore, of great importance for the application.

Infrared absorption, laser-induced fluorescence and optical emission spectroscopy (OES) are various techniques normally used to measure temperatures of excited or ground state molecular species in gas discharges [86, 87]. OES is a convenient [47] and non-intrusive diagnostic tool well suited for the determination of important plasma parameters such as particle densities, particle temperatures, electron energy distributions and for determination and control of the gas temperature [11, 88, 89].

Three well known optical methods are used for the determination of the gas temperature [90]:

- Determination of the rotational temperature from the rotational intensity distributions in the vibronic bands of Fulcher-$\alpha$ band system.
- Doppler broadening of molecular lines.

- Doppler broadening of atomic lines, taking into account the fine structure.

### 6.1.1 Gas temperature measurements based on rotational transition

The most commonly experimental technique for the determination of the gas temperature is the analysis of the intensity distribution in the rotational fine structure of electronic transitions [91]. OES can be used to measure relative intensities of rotational lines within a single vibrational band [90]. When the rovibrational populations are distributed according to the Boltzmann distribution, rotational and vibrational temperatures can be determined [92]. The rotational population $N(N^{'})$ of a vibrational sequence $(v^{'})$ is mostly well characterised by a rotational temperature $T_{rot}(v^{'})$ that reflects the gas temperature under certain conditions. $N^{'}$ and $v^{'}$indicate the respective rotational and vibrational quantum numbers. $T_{rot}$ is obtained either by using the "Boltzmann-plot-technique" or by a comparison of measured spectra with simulations based on the appropriate molecular constants. The Boltzmann plot method, is the most popular method, however this method may be unreliable in cases in which the rotational structure is not completely resolved, so in using this method it is necessary to identify, and to be able to resolve a sufficient number of well isolated rotational lines, which should not overlap one another [93]. The later method based on molecular constants (the method used during this work) requires extensive calculations, but offers the advantage of the incorporation of lines with specific spectral features [94]. It is well known that most of the excited electronic states of hydrogen are considerably perturbed, and the simple adiabatic models of the Franck-Condon approximation and Hönl-London formulae are not valid for the calculation of transition probabilities in this case. The Q-branch of the Fulcher-$\alpha$ band of $H_2$ are often used for gas temperature determination, because they are considered to be free from these perturbations [95] and free from superposition with other spectral lines. These rotational lines are located in a convenient spectral range (around 600 nm) and are relatively intense-easily recordable with common photodetectors. A basic problem of emission spectroscopy is the need to draw a conclusions on ground state populations and related properties from the measured emission out of excited states. It was shown recently [11, 96] that by combining sophisticated techniques like phase resolved optical emission spectroscopy (PROES) and modelling, this basic problem of OES can be overcome and that quantitative information referring to

the ground state can be retrieved.

The determination of the rotational temperature is based on the observation of rotational line intensity distributions in the rovibronic bands of Fulcher-$\alpha$ band system. The Q-branch transitions ($\triangle N = 0$) of the diagonal bands ($\triangle v = 0$) of the Fulcher-$\alpha$ system ($3p\,^3\Pi_u^- \rightarrow 2s\,^3\sum_g^+$electronic transition) are recorded. Although we have the possibility to detect the vibrational band $v^{'} - v^{''}$= (0 - 0, 1 - 1, 2 - 2, 3 - 3, 4 - 4) with $\triangle v = 0$, we selected the usual vibrational $v = 2$ Fulcher-$\alpha$ band of $H_2$ in calculation of the rotational temperature. This band has no overlap with other emission lines. Knowledge of the intensity ratios within one rotational band is necessary to infer the rotational temperature, and it is advantageous to measure the intensities of the rotational lines simultaneously in order to avoid the influence of time dependent drifts of the plasma or the experimental conditions [11]. It is possible to record a sufficient section of a rotational band (five rotational lines) in one spectral image with our detection system.

#### 6.1.1.1 Rotational temperatures determination from $3p\,^3\prod_u^- \rightarrow 2s\,^3\sum_g^+$ transitions of $H_2$

To summarize the basis of this diagnostic, it is useful to remind that the intensity of a spectral line due to a ($n^{'}v^{'}N^{'} \rightarrow n^{''}v^{''}N^{''}$) ro-vibronic transition can be written as the product of the population density of the upper state $N_{n^{'}v^{'}N^{'}}$ and the Einstein transition probability for spontaneous emission $A^{n^{'}v^{'}N^{'}}_{n^{''}v^{''}N^{''}}$:

$$I^{n^{'}v^{'}N^{'}}_{n^{''}v^{''}N^{''}} = N_{n^{'}v^{'}N^{'}} A^{n^{'}v^{'}N^{'}}_{n^{''}v^{''}N^{''}} \tag{6.1}$$

where a single prime (') is used to denote quantities pertaining to the upper level (in emission it is the initial state) and double primes (") to the lower level (the final state in emission), and $n^{'}$,$^{''}$, $v^{'}$,$^{''}$, $N^{'}$,$^{''}$ are quantum numbers of electronic, vibrational and rotational (total angular momentum without electronic spin) levels, respectively. If the population of one rotational band of the upper state can be described by a Boltzmann distribution, then the rotational temperature $T_{rot}(n^{'}, v^{'})$ can be obtained from the relation:

$$N_{n^{'}v^{'}N^{'}} = c_{n^{'}v^{'}} g_{as}(2N^{'}+1) exp(\frac{-E_{n^{'}v^{'}N^{'}}}{k_B T_{rot}(n^{'}v^{'})}) \tag{6.2}$$

where $c_{n^{'}v^{'}}$ is a normalizing constant, $g_{as}$ the degeneracy caused by the nuclear spin, $E_{n^{'}v^{'}N^{'}}$ the energy of the ro-vibronic level, $k_B$ the Boltzmann constant and

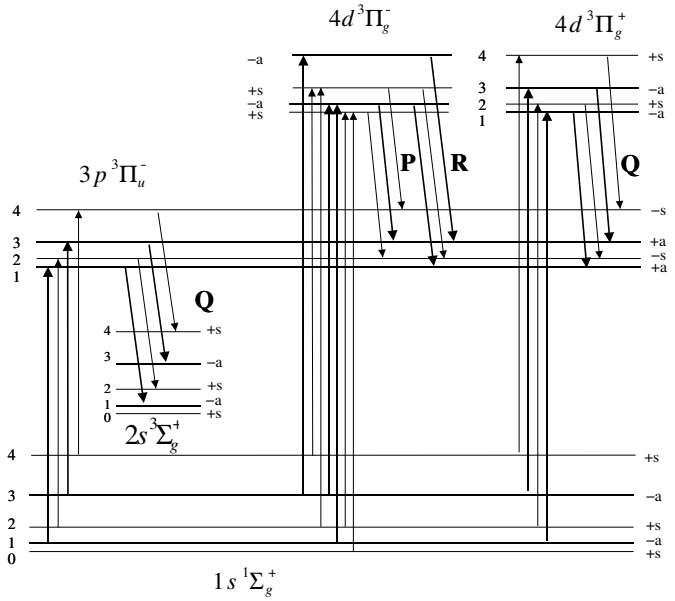


Figure 6.1: Diagram illustrating the population mechanisms; the left-hand side of the graph shows a Q-branch of the Fulcher-$\alpha$ band, the right-hand side shows P-, Q-, R-branches from the $\Pi$states of the 4d level into the upper Fulcher -$\alpha$ levels; the numbers correspond to the rotational quantum number N, a, s, +, - designate the symmetry properties of the molecular states.

$T_{rot}$ the rotational temperature. A detailed discussion of the conditions required for the relation between the rotational line intensity distribution and the gas temperature to hold was given by T. Gans et al. [11] on the basis of a kinetic model for the population and the depopulation of excited levels involved. These assumptions are:

1. The population distribution in the ground state $1s\,^1\sum_g^+$ is determined by heavy particle collisions and obeys a Boltzmann distribution whereby the rotational temperature $T_{rot}$ equals the gas temperature [97].

2. The excited states are populated only via electron collisional excitation out of the ground state.

3. The rate coefficients can be used in the adiabatic approximation. This is fulfilled for the Q-branches of the Fulcher-$\alpha$ band system ($3p\,^3\Pi_u^- \rightarrow 2s\,^3\sum_g^+$).

4. The excitation without change of the rotational quantum number ($\triangle N = 0$) dominates.

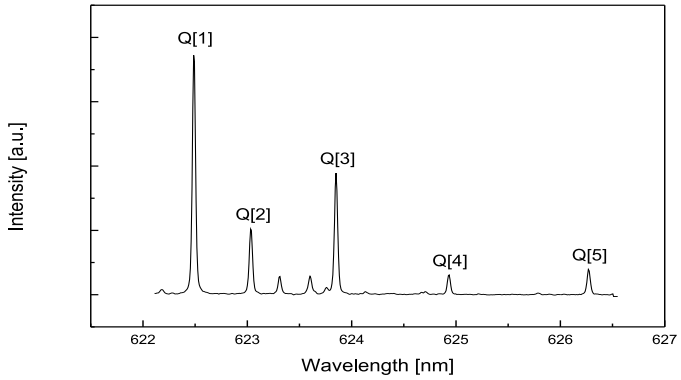


Figure 6.2: The first five rotational lines of the Fulcher-$\alpha$ (v=2) Q branch.

5. The effective lifetime of the excited states is independent of the rotational quantum number and are much shorter than the relaxation time of the rotational levels.

The thermal rotational distribution of the electronic ground state $1s\,^1\sum_g^+$ is "copied" into the excited state $3p\,^3\prod_u^-$ without change of the rotational quantum number $N$, under these conditions. The rotational distribution of the excited state can be determined from the spontaneous emission into the lower state $2s\,^3\sum_g^+$ as shown in Fig. (6.1). A fit of a Boltzmann distribution to these emissions yields the rotational temperature that is directly connected to the gas temperature under these assumptions.

The intensities of the first five Q-branch (2-2) Fulcher-$\alpha$ rotational lines are measured and a spectrum for these five lines is given in Fig. (6.2). The measured intensities of the first five Q-branch (2-2) Fulcher-$\alpha$ rotational lines differ within one spectrum by at least a factor of ten so a detection system with a high dynamic range is necessary, if the calculation of the rotational temperature is to be inferred from one single record. Since the relative error of low-intensity molecular lines is larger than for more intense, no linear fit was applied to obtain the temperature from a Boltzmann plot, but the least squares deviation between the calculated and the measured intensities was used instead, so that all rotational lines contribute according to their intensity.

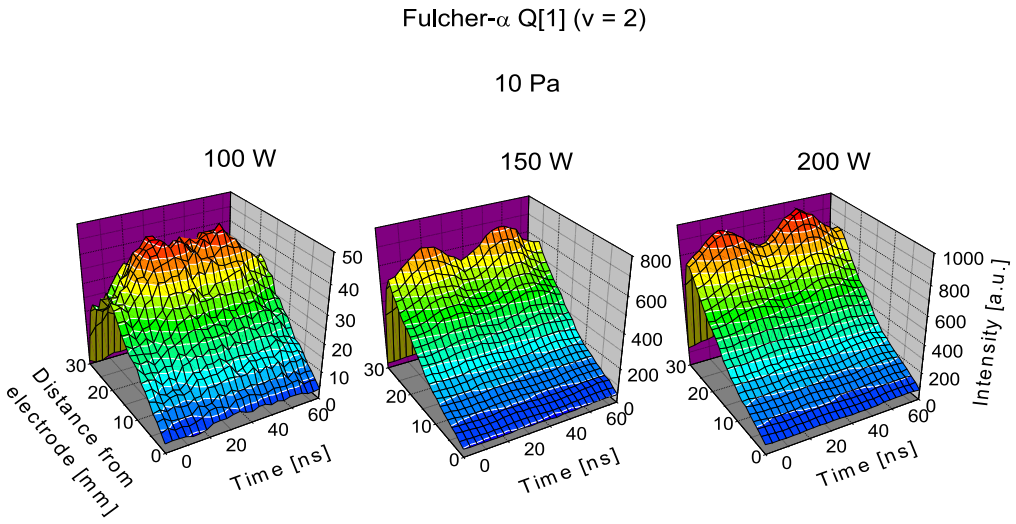


Figure 6.3: Time and space resolved emission intensity of Fulcher-$\alpha$ (v=2) Q [1] at 10 Pa with different powers.

#### 6.1.1.2 Time and axial dependencies of emission and rotational temperature

The temporal and axial behaviour of emission of $H_\alpha$ is already discussed in chapter 2. In principle the Fulcher-$\alpha$ lines display the same emission behaviour as the $H_\alpha$ line. In Fig. (6.3) the time and axial emission of the first Q [1] Fulcher-$\alpha$ (v=2) line at 10 Pa for different powers is shown. It has to be mentioned that the emission intensity of Fulcher-$\alpha$ (v=2) Q [1] is much lower than the emission intensity of $H_\alpha$. To ignite the discharge in the capacitive E-mode under this pressure condition (10 Pa), we need power less than 100 W. As a result much less intensity will be obtained with such low power. In this case there will be some problems in calculation of the rotational temperature as we will see afterwards. The transition mode is obtained at 100 W, which has intensity of one order of magnitude less than the inductive H-mode, which is obtained at 150 W. With increasing the power, the emission intensity rises. An emission modulation of about 20 % is obtained under this pressure condition. Other axial and time behaviours have already been discussed in Chapter 5 (section 1). The transitions Q[2] to Q[5] exhibit the same emission characteristics as Q[1]. An analysis of the

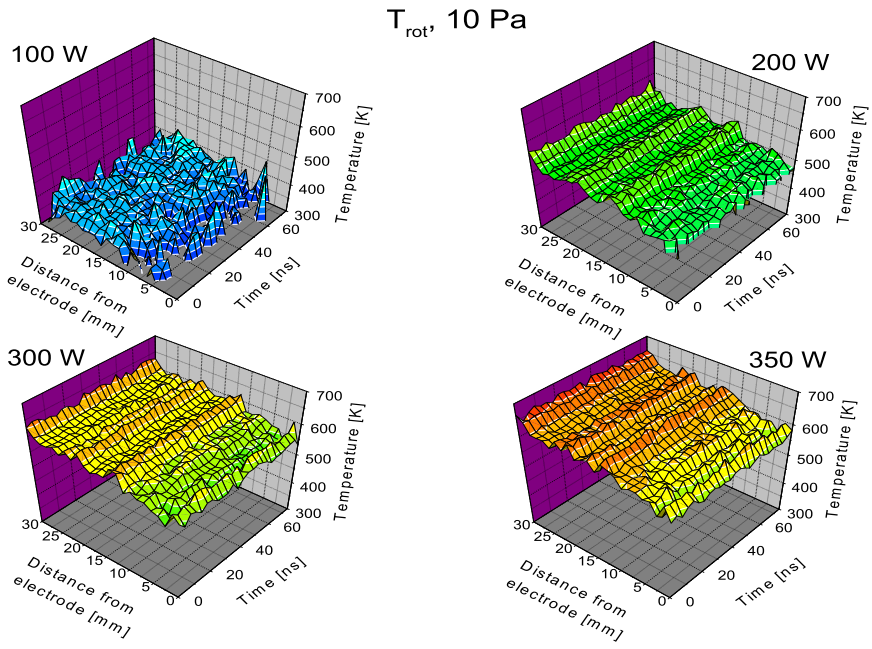


Figure 6.4: Time and space resolved of rotational temperature obtained from the first five Fulcher-$\alpha$ rotational lines at 10 Pa with different powers.

temperature from emission intensity measurements can be performed at any time and position between the electrodes using these five rotational lines.

The temporal development of the rotational temperature along the discharge axis obtained from the analysis using the first five Fulcher$\alpha$ (v=2) lines at 10 Pa with different powers are shown in Fig. (6.4). In the transition mode, which is obtained at 100 W, the rotational temperature assumes values in the range of about 350 to 400 K. With this low power, the cooling of both the grounded electrode and the coil has a big effect on the gas (species) kinetics. Hence, less collisions as a result of cooling and low pressure inside the discharge leads to a measurable rotational temperature of about 100 K higher than room temperature. The inductive H-mode is obtained at more than 100 W, with which an increase in the rotational temperature is clearly remarked. The temperature increases axially with increasing the power. Near the coil the temperature has values of about 550, 600 and 650 K with powers of 200, 300 and 350 W respectively. At the same time the temperature close to the electrode rises from about 470 K at 200 W to reach

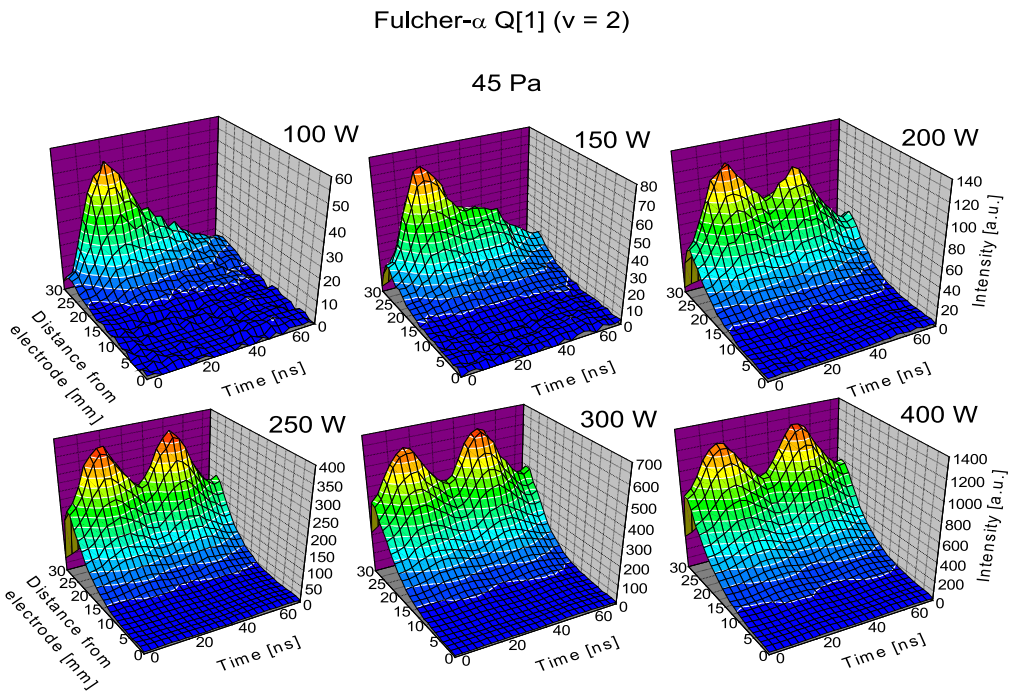


Figure 6.5: Time and space resolved emission intensity of Fulcher-$\alpha$ (v=2) Q [1] at 45 Pa with different powers.

more than 570 K at a power of 350 W. Hence, a temperature gradient of more than 50 K is observed axially between the antenna coil and the electrode.

The results of time and axial emission of Fulcher-$\alpha$ Q[1] (v=2) and rotational temperature obtained at another pressure (45 Pa) with different powers are shown in Figs. (6.5 and 6.6) respectively. In contrast to emission results at 10 Pa, emission results at 45 Pa reveals that the discharge is ignited in the E-mode up to about 150 W. A much stronger emission modulation of about 80 % is obtained as compared to 90 % modulation observed in the CCRF discharge [11]. The transition mode is sustained with increasing the power at about 200 W. A fully inductive H-mode is delayed at this pressure condition to be reached at about 250 W in comparison with 150 W at 10 Pa. In this case of high pressure a little more neutral gas is flowing through the discharge vessel than at 10 Pa. The electron mean free path in this case is decreasing, as a result low energy is gained by these electrons from the external source. In this case fast electrons required for collision

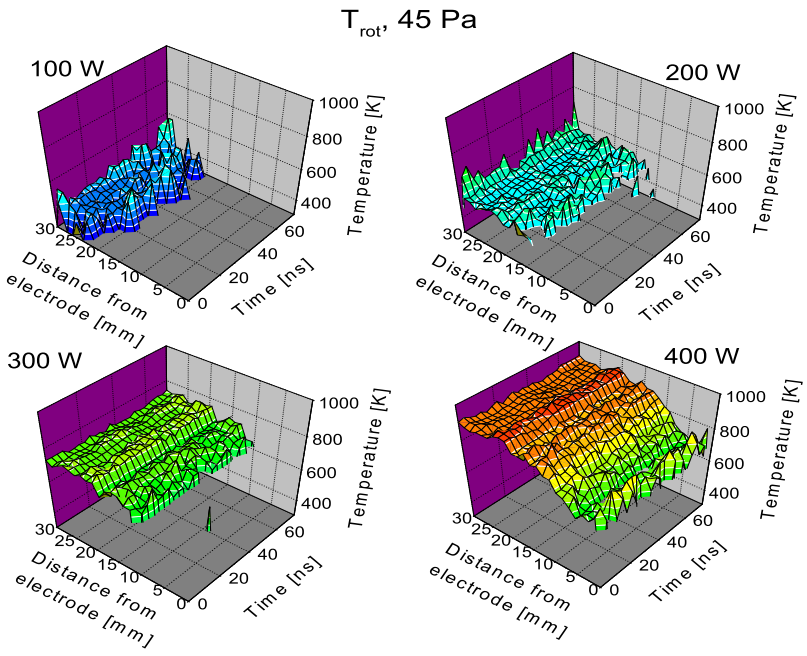


Figure 6.6: Time and space resolved of rotational temperature obtained from the first five Fulcher-$\alpha$ rotational lines at 45 Pa with different powers.

and excitation processes decreases. Hence the discharge needs much more power to reach the condition required to ignite the H-mode.

As always declared, the emission intensity rises with increasing the applied power to reach more than two orders of magnitude at 300 W (H-mode) as compared with the emission obtained at 100 W (E-mode). The emission modulation obtained in the inductive mode at this pressure is reduced to about 40 %. A very small gradual increase of emission is noticed from the grounded electrode until a distance of about 20 mm is reached. An abrupt change of emission in all the discharge modes is obtained after 20 mm until the emission maximum is reached.

Under some conditions (low power, far away from the coil, near the cooled electrode) it was not possible to calculate a rotational temperature, because the emission was so faint that only three rotational lines and less could be safely recorded. Even with our fast camera the integration time would have been so long that one measurement would have taken more than a day. An explanation could be that this area closed to the electrode is much more distant from the power

transmitted area under the antenna coil. The applied power is too low that, it is not really enough to have an effect away from the coupling area close to antenna coil especially near the grounded electrode. In addition the grounded electrode is cooled by water, which also could contribute as a factor for cooling of plasma near electrode. These are the reasons that part of the rotational temperature near the grounded electrode is missing at powers of 100, 200 and 300 W in Fig. (6.6) showing the temporal development of the temperature at 45 Pa along the discharge axis. At 100 W, a capacitive mode is reached assuming a rotational temperature value in the range of 400 K near the coil (the possible results) in agreement with the results obtained before in a 'real' CCRF discharge at the same power and pressure conditions [11]. A temperature of about 500 K (near the coil) is reached for T-mode at 200 W. With increasing the power the missing temperature part is contracted to reach less than 10 mm in the inductive mode at 300 W at which a temperature of about 700 K is obtained.

At 400 W, we can observe three important features: First we have no problem any more in calculating the rotational temperature as a result of higher emission intensity obtained under high power condition. Second, in contrast to the gradual decrease in the rotational temperature from the coil towards the grounded electrode in case of 10 Pa at high power, a plateau area within values of approximately 850 K near the coil is obtained. This area expands up to about 15 mm distance from the coil, afterwards a gradual decrease in the rotational temperature is noticed axially towards the grounded electrode. The third feature, a considerably higher temperature of about 600 K is obtained near the grounded electrode. The reason for these three things might be that at high power the energy is deposited deeper into the volume between coil and electrode. At the same time the electrode and the vessel are heated more so that the cooling by the electrode becomes less effective.

#### 6.1.1.3 Comparison with model

As one very important information from the time resolved rotational temperature measurement within one cycle of the ICP-discharge we observe that the rotational temperature does not exhibit any prominent time dependence on a time scale of the RF period ($\tau_{RF} = 74ns$) in either of the discharge modes at low pressure (10 Pa) as displayed in Fig. (6.4). At 45 Pa we can say that there are just a little bit time behavior of the rotational temperature within the range of about

20 K near the exciting coil as shown in Fig. (6.6). It may be important to remark that these results are calculated with the same program applying the same algorithms and underlying model that reveals a time dependent modulation of the rotational distribution equivalent to about 100 K in the case of a CCRF discharge [11]. In that case it could be shown that the time variation is correlated with population out of high lying cascading states so that the conditions for the underlying model are fulfilled best at the excitation maximum. Then the analysis yields the (formally) lowest rotational temperature.

One important difference between the CCRF discharge and the ICP is as already mentioned, that the modulation of the emission intensity in case of the CCRF-discharge was high in comparison with the intensity modulation in the H-mode ICP-discharge for our conditions. The observed time modulation in CCRF discharge was explained to be due to a change of the rotational distribution of the upper levels, which can occur by collisions of excited molecules with other molecules or by additional population of the excited rotational levels by cascading processes from higher states [11]. The influence of the cascading processes from higher lying electronic states on the population dynamics of the $3p^3\prod_u^-$ state was analysed. The largest contributions issue from the $4d$ states so that according to the selection rules Q-transitions from the $4d^3\sum_g^+$, $4d^3\prod_g^+$, $4d^3\Delta_g^+$ states and P- and R-transitions, i.e. with change of the rotational quantum number out of the $4d^3\prod_g^-$, $4d^3\Delta_g^-$ states have to be taken into account.

The temporal development of the population $N_{N'}(t)$ of a $3p^3\prod_u^-$ rotational level is described by the rate equation [11]:

$$\frac{d}{dt}N_{N'}(t) = -(A+Q)N_{N'}(t) + C(N')exp(-\frac{t}{\tau}) \tag{6.3}$$

Where A and Q represent the fluorescence and the quenching rate respectively, the parameter $C(N')$ describes the strength of the cascading contributions.

Then we get:

$$N_{N'}(t) = N_{N'}(0)exp(-(A+Q)t) + \frac{C(N')}{A+Q-(1/\tau)}[exp(-\frac{t}{\tau}) - exp(-(A+Q)t)] \tag{6.4}$$

The dependence of the cascade contributions $C(N')$ on the rotational quantum number $N'$ is determined by the transition probabilities from the $4d$ into the $3p$

states and by the rotational distribution in the $4d$ states. The transition probabilities can be described by the Hönl-London factors in the adiabatic approximation [98]. Neglecting further cascades the rotational population of the $4d$ states by electron collisional excitation out of the ground state can be described by [99]:

$$n_{n',v',N'} \propto Y_{n' \leftarrow n''}(T_g, N') \cdot g_{a,s} \cdot (2N'+1) \cdot exp\left(-\frac{N' \cdot (N'+1) \cdot B_0}{k_B \cdot T_g}\right) \tag{6.5}$$

Here $B_0$ is the rotational constant of the ground state and $Y_{n' \leftarrow n''}(T_g, N')$ describes the dependence of the excitation rates on the rotational quantum number. $Y_{n' \leftarrow n''}(T_g, N')$ is depending on the electronic state and can be represented with the 3-j symbols of Wigner for the different states [100]. It has to be discerned between states $4d\,^3\sum_g^+$, $4d\,^3\Pi_g^+$, $4d\,^3\Delta_g^+$ where $\Delta N = 0$ is valid for allowed transitions and the states $4d\,^3\Pi_g^-$, $4d\,^3\Delta_g^-$ for which $\Delta N = \pm 1$ is valid. For the first case $Y_{n' \leftarrow n''}(T_g, N')$ describes the different weightings for transitions of different rotational states that yield a redistribution in the upper state (6.6). In the later case we get two contributions due to the change in the rotational quantum number making the redistribution quite obvious (6.7):

$$Y_{n' \leftarrow n''}(T_g, N') = (2N'+1) \begin{pmatrix} N' & 2 & N' \\ -\Lambda' & \Lambda' & 0 \end{pmatrix}^2 \tag{6.6}$$

$$\begin{aligned} Y_{n' \leftarrow n''}(T_g, N') &= (2N'-1) \begin{pmatrix} N' & 2 & N'-1 \\ -\Lambda' & \Lambda' & 0 \end{pmatrix}^2 \cdot exp\left(\frac{2N' \cdot B_0}{k_B \cdot T_g}\right) \\ &+ (2N'+3) \begin{pmatrix} N' & 2 & N'+1 \\ -\Lambda' & \Lambda' & 0 \end{pmatrix}^2 \cdot exp\left(-\frac{(2N'+2) \cdot B_0}{k_B \cdot T_g}\right) \end{aligned} \tag{6.7}$$

$\Lambda'$ is the angular momentum along the internuclear axis of the excited state. The 'zero' within the 3-j symbol results from the $\Lambda'' = 0$ of the ground state. The '2' is valid for the transition from $1s$ to $4d$. The changes of the population distribution described by this $Y_{n' \leftarrow n''}(T_g, N')$ in combination with a different lifetime of the cascading states result finally in rapid variations of the rotational distribution that are attributed to a rotational 'temperature'.

With the given formula for the temporal population of the rotational levels, both the temporal behaviour of the emission and the history of the temperature

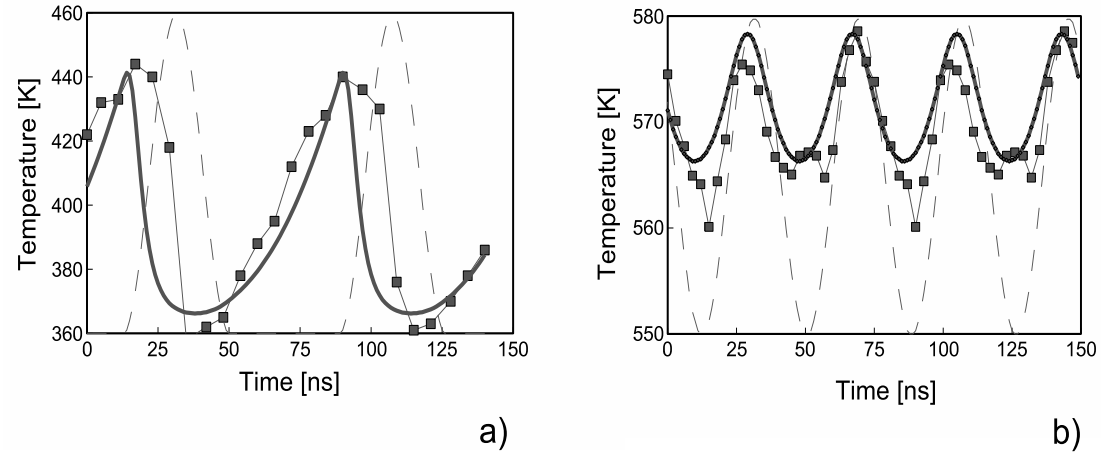


Figure 6.7: Modelling of the time dependent rotational temperature for a capacitively coupled RF discharge at 42 Pa and 100 W and for an inductively coupled RF discharge at 15 Pa and 350 W. Both calculations are done for the axial distance of maximum emission. The squares show measured temperature values. The continuous line displays the time dependence of the temperature calculated from the model. The dotted line shows the assumed excitation function.

can be determined on the basis of the comparison of all rotational lines with the model described.

To further analyze this behavior the mentioned analytical model was replaced and extended by a numerical model based on the same assumptions [11]. A constant lifetime of 143 ns for the cascading levels was used while for the Fulcher transitions the effect of collisional quenching was taken into account. The upper Fulcher levels and the cascading levels are located at excitation energies of about 14 and 14.7 eV, respectively. Within the model we assume that they are populated according to a mean electron 'temperature' of 1 eV. This value, together with a drift energy of about 50 eV, was determined by PROES for the electrons of the CCRF discharge at the position of maximum emission [101]. The contribution of the cascades to the population of the upper Fulcher level is now treated as a parameter. In contrast to the analytical model starting from the condition of maximum excitation and running only until the next exciting pulse, the numerical model includes the periodic excitation due to the electrons driven by the RF generator. To describe the time behaviour of the excitation we chose a $sin^2\omega_{RF}t$-

functionality for the excitation function providing the necessary twofold excitation per RF- cycle in H-mode. For the CCRF the second maximum of the function within a cycle was arbitrarily set to zero. The behaviour is represented in Fig. (6.7) by dashed line. The half-width of the excitation maxima of about 20 ns is in good agreement with the measurements. In a first step the population of cascade and upper Fulcher levels is calculated neglecting the rotational sublevels until stationarity is reached. As a first result it was found that within the model a contribution by the cascades of about 8% yields a modulation of the emission that agrees very well with the observed one for the H-mode of the ICP as well as for the CCRF discharges and for different pressures. This is in good agreement with the results of the analytical model. In a second step the population dynamics of the rotational sublevels is taken into account. As initial value the population of the rotational ground state levels is set according to a given gas temperature. Note that this initial temperature corresponds to the gas temperature, since equilibrium is assumed in the ground state. From here, population and depopulation of upper Fulcher and cascade levels are calculated as described above. All cascade levels are equally weighted. The calculation runs through about 30 RF-cycles before the results become stationary. The resulting distribution is finally correlated with a rotational 'temperature'.

As a test the model was applied to the conditions of the capacitively coupled discharge as used by Gans et al. [11]. The result is shown as continuous line on the left hand of Fig. (6.7) in comparison to the temperature behavior as measured by PROES (filled squares). Two RF cycles are displayed on the time axis. The bottom value of the temperature axis marks the initial temperature of the calculation. The temperature 'rise' after the end of the excitation pulse agrees well with the measured behavior. Deviations for the time of the excitation pulse can be attributed to differences between the shape of the 'synthetic' and actual excitation function.

The right graph of Fig. (6.7) shows the calculated temperature behaviour for an inductively coupled plasma at 15 Pa in combination with measurements taken at the point of maximum emission about 10 mm below the coil. Again the base line temperature corresponds to the initially assumed gas temperature for the model and two RF cycles are plotted. Both graphs clearly demonstrate that the model describes well the time behaviour for both discharge types. During the excitation

phase the rotational 'temperature' falls quickly towards the given gas temperature since, at that time the influence of the cascades is minimum. After this phase the cascade contributions yield a change of the rotational distribution due to the long lifetime of the cascading levels. This is analysed as an (artificial) increase of the attributed temperature. For the CCRF due to the long time between excitation pulses the temperature variations are large ($\Delta T \approx 90$ K) since, the relative contribution from the cascades increases because of the longer lifetime of these states. At the same time the population of both levels has fallen so far, that it can be neglected compared to the population by the following excitation pulse. In this way the temperature at maximum excitation is very close to the ground state temperature. Due to the more rapid repetition of the excitation in the ICP, the variation of the relative contribution to the population is reduced, so that the temperature variations stay small - for our conditions resulting in temperature variations of about 20 K. On the other hand the Fulcher states are not depleted as much as in the capacitive mode, so that there is a continuous contribution resulting in a more pronounced deviation from the ground state temperature as compared to the capacitive case. For our pressure range of 5 to 60 Pa this increase stays below 20 K. This means that both effects are within the estimated error of our temperature measurement. From the modelling, it can be taken that quenching prevents a stronger deviation from the starting temperature under these conditions but yields a stronger temperature modulation of about 50 K at 60 Pa. Intensity problems impede an verification of these structures in our discharge. The base temperature rise as well as the modulation would assume higher values if the cascade contributions were stronger than mentioned above. In conclusion, it can be stated, that the effects described here influence the results of the common time-integrated OES analysis but the deviations will stay within typical experimental errors.

#### 6.1.1.4 Power and pressure dependencies on the rotational temperature

Fig. (6.8) illustrates the effect of power and pressure on the rotational temperature at position of maximum emission (about 6 mm from the dielectric window in front of the exciting coil). Lower rotational temperatures of about 400 K are obtained during the capacitive mode at low pressure, a little bit higher values are obtained at higher pressures. With increasing the power, an increase in the rotational temperature is observed at all pressures. It is clear from the figure that the

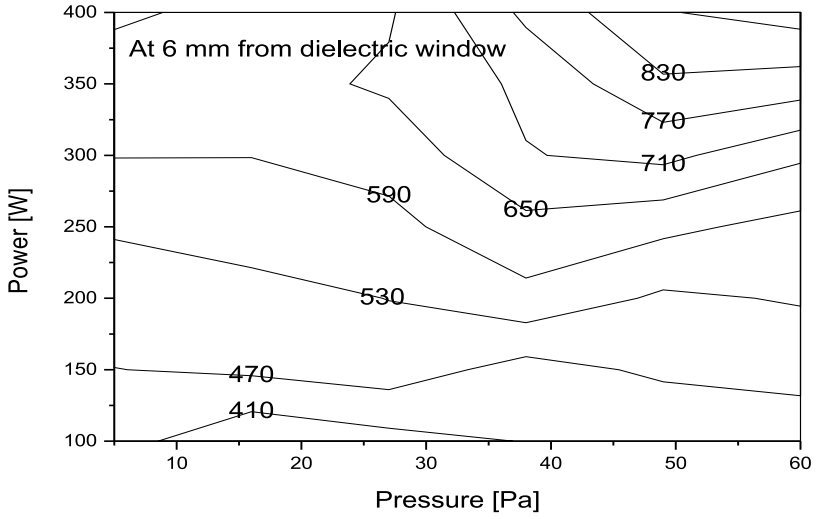


Figure 6.8: Effect of power and pressure on the rotational temperature at distance of about 10 mm from the exciting coil.

rotational temperature is strongly dependant on the pressure, which divides the graph into two parts: Below 25 Pa, the discharge is always ignited in the H-mode, characterized by its higher rotational temperature except at very low power. A slow increase of temperature is obtained with increasing of power. At 300 W a temperature of about 600 K is obtained, while a maximum temperature of about 650 K at 400 W is reached. On the other hand, at high pressure above 25 Pa, the discharge is ignited in the E-mode with much lower density until 250 W is reached. Afterwards a rapid increase of rotational temperature with power is observed. At 300 W a temperature of more than 700 K is obtained. A much higher values of more than 850 K is reached at maximum power and pressure.

Hence an H-mode obtained at lower pressure and at higher power is characterized by a rotational temperature of about 600 K, meanwhile H-mode obtained at higher pressure and at higher powers poses a very high rotational temperature of more than 800 K.

### 6.1.2 Determination of the gas temperature by Fabry-Perot Interferometry

The discussion of the rotational temperature immediately leads to the demand of

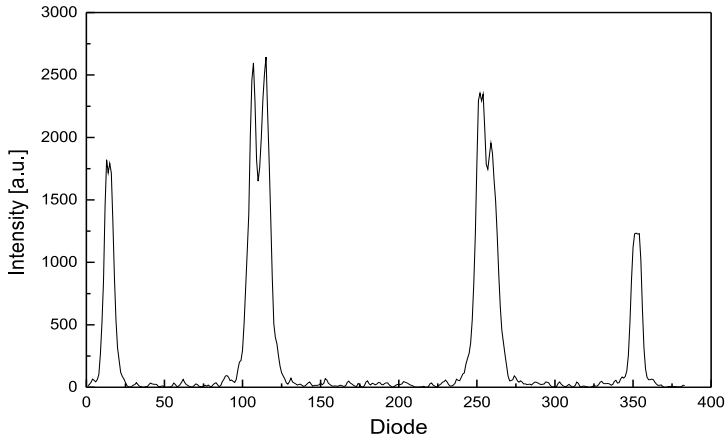


Figure 6.9: The obtained interferogram of He-Ne laser using FPI.

an independent check of the gas temperature. A technically challenging method would be the calculation from the measurement of the ground state line width by laser induced fluorescence. For this diagnostic tunable high power lasers are required with small linewidth and emission in the VUV for one photon excitation ($\lambda \sim 120$ nm) or in the UV for two photon excitation ($\lambda \sim 230$ nm). Much simpler and equally significant is the determination of the translational temperature on the basis of Fulcher-linewidths. A combination of 2-meter spectrograph and FPI etalon was used to determine the translational temperature. In this construction the spectrograph serves to select one free spectral range of the interferometer which itself provides the necessary spectral resolution. In this arrangement only a cross section of the typical ring system of a Fabry-Perot interferometer appears within one spectral line of the spectrograph on the camera. Since this dimension of the camera coincides with the axial dimension of the discharge, it is possible - in principle - to get spatially resolved information. In our experiment this is limited by the available intensity at each location, so that again the position of maximum emission was used for the analysis.

**Determination of the instrument function and the finesse:** The instrument function and the finesse of the used Fabry-Perot interferometer (FPI) were

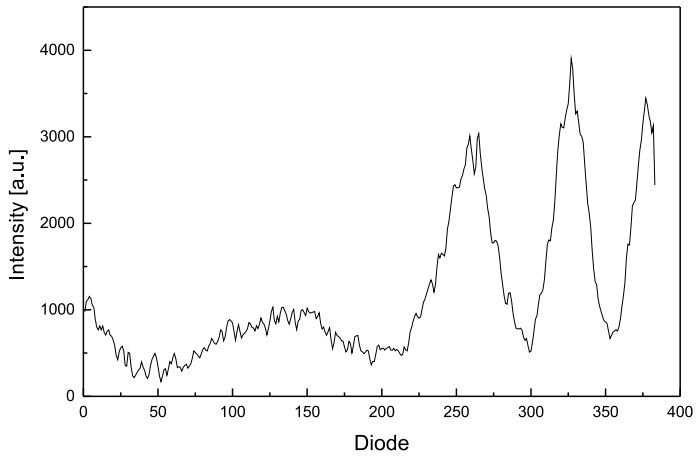


Figure 6.10: The FPI ring system of the Fulcher-$\alpha$ Q[1] (v = 2) line.

checked by using a He-Ne laser (632.8 nm) as a light source. The instrument function (Airy function) can be seen directly in the output signal as shown in Fig. (6.9). The free spectral range for near-normal incidence is expressed as mentioned in chapter 3:

$$\Delta\lambda_{FSR} = \lambda^2/2nd \tag{6.8}$$

The finesse ($F$) of the FPI is the ratio of the distance between two peaks to the full width at half maximum of the peak and it is depending on the cavity spacing:

$$\Delta\lambda_{FWHM} = \Delta\lambda_{FSR}/F \tag{6.9}$$

A finesse beyond 15 yielding a resolution of $< 0.5$ pm was determined by analyzing the He-Ne laser interferogram.

**Determination of the translational temperature** If it is assumed that the broadening of the spectral line is caused only by thermal motion, then the line profile has a Gaussian shape with Doppler width given as [56]:

$$\Delta\lambda_D = (\lambda_0/c)\sqrt{2kT/M} \tag{6.10}$$

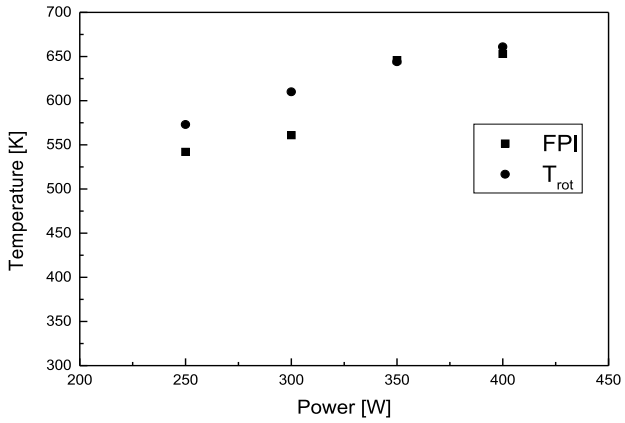


Figure 6.11: The results of temperature obtained by FPI and the rotational temperature at 15 Pa with different power.

$$\Delta\lambda_{FWHM} = 2\sqrt{ln2}(\lambda_0/c)\sqrt{2kT/M} \tag{6.11}$$

Then the required translational temperature is expressed as:

$$T = \frac{M}{2ln2\ k}(\frac{c\,\Delta\lambda_{FWHM}}{2\lambda_0})^2 \tag{6.12}$$

An FPI ring system of the Fulcher-$\alpha$ Q[1] (v = 2) line is shown in Fig. (6.10). The FWHM is calculated from the first ring in order to get the temperature results. The translational temperatures of $H_2$ measured with this system are displayed in Fig. 6.11 as a function of the input power at a pressure of 15 Pa. The results are compared with the measurements from the analyses of the rotational Fulcher-$\alpha$ bands. For both cases it is assumed that the temperatures reflect the gas temperature. Within the H-mode the temperature rises linearly from about 550 K to more than 650 K for input powers between 250 and 400 W. The rotational temperatures are slightly higher than the translational ones at low power, what might be attributed to the temperature deviation as explained above. Both methods yield comparable results as demonstrated in the figure. For the interferometry we estimate the statistical error range to be below 50 K.

From these measurements we conclude that temperature analyses from the

rotational bands yield result that reflect the real gas temperature for our discharge.

### 6.1.3 Application to side-on measured Fulcher band intensities:

In order to obtain time resolved temperatures with axial and radial space resolution, the procedure was applied: The radius of the discharge was scanned with the stepper-motor controlled mirror over 12 measurement positions starting at the center of the discharge. With the help of a stepper-motor controlled mirror our measurement is in principle based on an angular displacement as mentioned before in Chapter 3, section 3.3. We took account of this by transforming the angle $\alpha$ for the known distance between mirror axis and discharge axis into the lateral distance $y$ of a line-of-sight while preparing the numerical integration applied for Abel inversion with the Fourier method [71, 72]. At each angular position the spectrum of the ($v = 2$) Q-branch Fulcher-$\alpha$ rotational lines was recorded simultaneously in 25 time windows covering the complete excitation cycle. At each angular and each time position, the axial intensity profile - on the second dimension of the CCD-camera - is subdivided into 24 equidistant axial positions to keep the amount of data manageable. To further reduce the data the intensities of each of the five analysed Q-branch lines are extracted from the spectrum and stored into separate files. Finally the time and space (2-dimensions) resolved intensities of the five Fulcher lines are stored in sets of 12 (radial positions) x 5 (spectral lines) files for further analysis - each of the files containing a matrix of 25 time windows and 24 axial positions. Abel inversion (Fourier method) routines are then applied to each set of axial and temporal intensity measurements of the five Fulcher lines. The radial emissivity results are stored in another set of 12 separate files with the same dimensioning as original for each line. For each of these temporal, axial and radial positions the rotational temperature routine is applied to the five Q-branch emissivities to yield the respective rotational temperatures at each spatial and temporal position.

### 6.1.4 Radial gas temperature results

Since the temporal variations of the rotational temperatures are below 20 K and close to the noise level we will neglect time dependencies in the analysis of the radially and axially resolved measurements. Fig. (6.12) displays the time integrated radially resolved rotational temperature profile at 250 Watt and 15 Pa measured

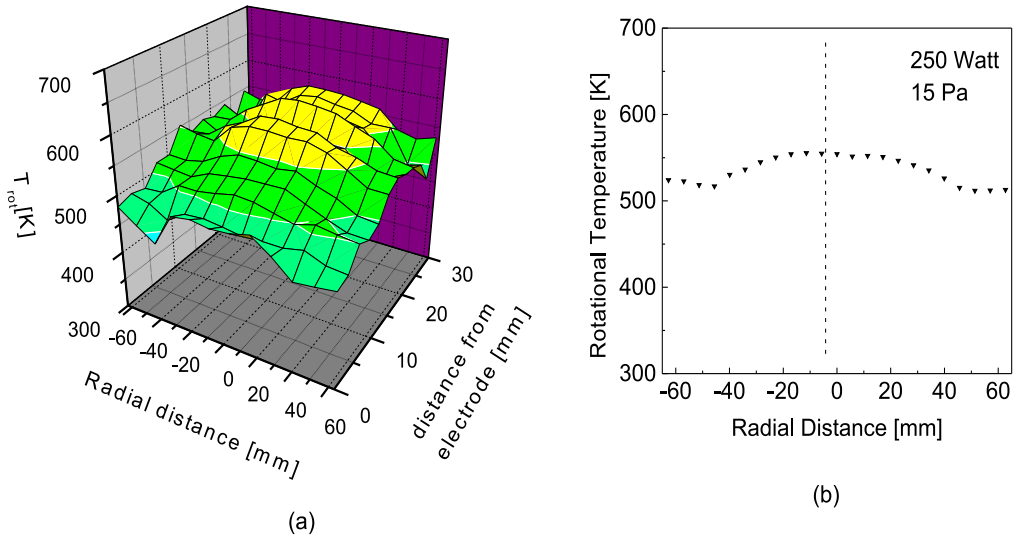


Figure 6.12: The time and space integrated rotational 'temperature' of the whole discharge at 250 Watt and 15 Pa (a) as a function of radial and axial distances from electrode and (b) in the center plane as a function of radial distance.

in the central plane of the discharge. For this experiment one complete radial scan through the whole discharge was performed and analysed separately for both sides from the discharge axis with the Abel algorithm as described. The symmetric property of the rotational temperature around the center of the discharge is clearly observable so that radial symmetry as the most important prerequisite to applicability of the Abel inversion is fulfilled. The behaviour of two-dimensional axial and radial rotational temperature profiles as a function of input power is shown in Fig. (6.13). In a plateau region of about 35 mm radius a constant temperature is observed. For the H-mode measurements this 'bulk' region of constant temperature expands with increasing power further towards the electrode. In this 'bulk" the rotational temperature shows a maximum value of about 400, 575 and 650 K at powers of 150, 250 and 350 Watt, respectively. The temperature decreases for each power towards the grounded electrode. For the transition mode the temperature reaches about 350 K very close to the electrode. At 250 W the

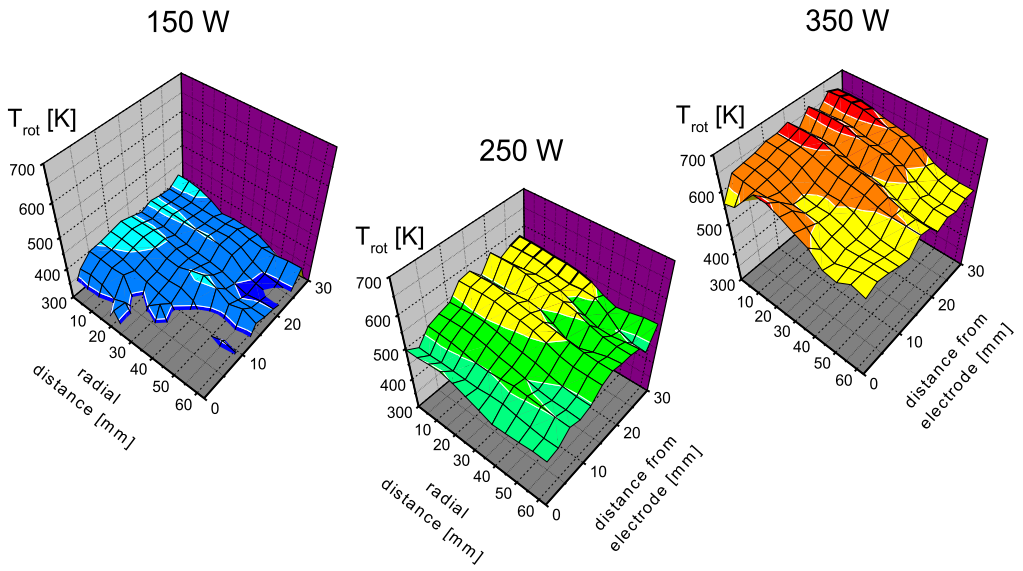


Figure 6.13: Time integrated Abel inverted rotational temperature fields as a function of radial and axial distances at different power (a) 150Watt, (b) 250 Watt and (c) 350 Watt at a pressure of 15 Pa.

temperature falls off within about 10 mm from the plateau value to 450 K near the electrode. At 350 W this reduction is much less pronounced (about 50 K), so that the 'bulk' nearly fills the volume between coil and electrode. The radius of this region is clearly correlated with the outer radius of the exciting planar coil of 37 to 40 mm (depending on the spiral structure). The main power input into the discharge takes place in the volume below the coil. For higher radial distances the temperature falls off. Outside the discharge defined by the diameter of coil and electrode at about 60 mm from the axis the temperature has values of about 350, 500 and 575 K for increasing values of power. At this edge position the temperature only shows a very weak axial dependence and approaches a constant value. The variations stay within a limit of about 25 K. The temperature here is probably connected to the vessel temperature. This also rises with input power meaning that more energy is transported outside to the walls. For 150 W input power in the E-mode the axial and radial structures are very weak. Within our measuring

errors of about 25 to 50 K - depending mainly on intensities and therefore highest under these conditions - we can only state a decrease towards the electrode. Radially the discharge shows no clear dependence, so that the temperature stays at the value on the axis.

## 6.2 Determination of the Degree of Dissociation

The knowledge of the concentration of species of molecular gases such as the atomic fraction of $H_2$ is of great interest in a variety of applications, including the deposition processes of functional thin films such as hydrogenated microcrystalline silicon and diamond. Absolute H atom is essential for understanding the mechanism of the process going on at the surface. A diatomic molecule can undergo thermal dissociation if its internal energy exceeds the dissociation energy. It is of great importance to develop a reliable spectroscopic methods for the determination of the degree of dissociation in processing plasmas. Several spectroscopic schemes based on the existence of the corona equilibrium conditions are available to determine the degree of dissociation in hydrogen containing plasmas. Based on the corona model the population of an excited state is given in the simplest case by:

$$\frac{dn_i}{dt} = n_0 E_i - n_i A_i \tag{6.13}$$

where $n_0$ is the ground state density, $E_i$ the excitation function, $n_i$ the population of the excited state and $A_i$ the decay rate of the spontaneous emission.

The electron excitation function $E_i$ is written in the form [6, 81]:

$$E_i = n_e \int_0^\infty \sigma_{exc}(E) \sqrt{\frac{2E}{m_e}} f(E) dE \tag{6.14}$$

where $n_e$ is the electron density, $\sigma_{exc}(E)$ the electron excitation cross section, $m_e$ the electron mass, $E$ the electron energy and $f(E)$ the electron energy distribution function.

The corona model is assumed in actinometry, which means stationary conditions ($\frac{dn_i}{dt} = 0$) are applied (the spontaneous emission is balanced by electron impact excitation). In this case the population of an excited state is written as:

$$n_i = n_0 \frac{E_i}{A_i} \tag{6.15}$$

The emitted radiation of a line, i.e. the photon numbers per unit volume and time $\dot{N}_{ph,i}$ is given by the product of the population density $n_i$ of the excited state and the corresponding transition rate $A_{ik}$ [16, 48, 102]:

$$\dot{N}_{Ph,i} = A_{ik} n_i \tag{6.16}$$

This leads to:

$$\dot{N}_{Ph,i} = \frac{A_{ik}}{A_i} n_0 E_i = \frac{A_{ik}}{A_i} X_i \tag{6.17}$$

where $A_{ik}/A_i$ is the branching ratio of the specific line and $X_i$ is the excitation rate from the ground state.

### 6.2.1 Actinometry

Actinometry is an optical emission spectroscopy method used to measure the density of atoms and molecules in their ground state. The method consists in seeding the discharge medium with a small amount of a non-reactive (noble) gas acting as a trace or reference called actinometer, which has to be properly selected. In this technique an atomic emission line of the discharge gas is compared with an atomic line of the actinometer (noble gas). Intensity changes of the noble gas spectral line reflect changes in the excitation conditions. This technique was used for the first time by Coburn and Chen in 1980 in an $O_2 - CF_4$ mixture [103] in order to measure the density of fluorine atoms using argon as an actinometer. Actinometry was used by some other authors to determine the concentration of atomic species in an $O_2$, $N_2$, $Cl_2$ and $H_2$ plasma in different discharges. Now, we try to discuss the possibility of using an advanced method, we call the "two gas actinometry" for the H atom density measurements in an inductively coupled plasma discharge.

Although actinometery is a straightforward technique, certain conditions must be satisfied in order to obtain reliable measurements [104, 105, 106, 107], i.e. the actinometery method depends upon the excitation processes of the atomic species $S$ and the actinometer $R$, in the following way:

1. To perform actinometry, only a small amount of the actinometer gas should be introduced in the discharge to avoid perturbation of the plasma.

2. The emission of both the actinometer and the species of interest are produced by electron impact excitation from their ground state.

3. The cross sections of the excitation process for both species and actinometer

have similar shape and threshold.

4. The quenching processes and all the other loss processes of the excited state species should be negligible when compared with de-excitation by the radiative process.

Then, the schemes of the excitation process for both species and actinometer are:

$$e^- + S \rightarrow S^* + e^- \quad , \quad e^- + R \rightarrow R^* + e^- \tag{6.18}$$

and the corresponding de-excitation schemes are:

$$S^* \rightarrow S + h\nu \tag{6.19}$$

$$R^* \rightarrow R + h\nu^- \tag{6.20}$$

### 6.2.2 Direct actinometric method (classical method)

A simple relation of proportionality between the concentrations ratio of the atomic ground state species and actinometer $(n_0^S/n_0^R)$ to the corresponding emission intensities $(I_{meas}^S/I_{meas}^R)$ is given as follows: For a gas like hydrogen $H$ with an actinometer $R$, the excitation rate $X_i$ from the ground state can be determined as the product of the ground state density $n_0$ and the excitation function $E_i$:

$$X_i = n_0 E_i \tag{6.21}$$

i.e.

$$n_0^H = \frac{X_i^H}{E_i^H} \qquad\qquad n_0^R = \frac{X_i^R}{E_i^R} \tag{6.22}$$

The density ratio of the atomic hydrogen and the reference gas can be expressed as:

$$\frac{n_0^H}{n_0^R} = (\frac{E_i^R X_i^H}{E_i^H X_i^R}) \tag{6.23}$$

The actinometry conditions are fulfilled in such case that the excitation cross section for both the spieces (atomic hydrogen) and the actinometer has the same shape and threshold energies. In this case the electron energy distribution function

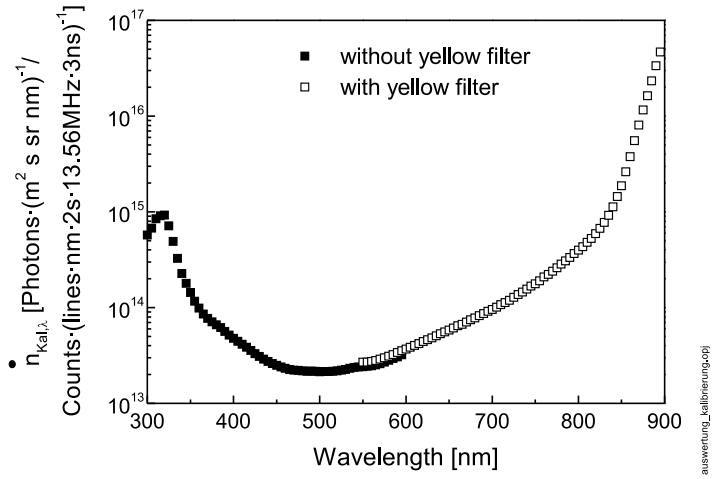


Figure 6.14: Absolute calibration of the detection system.

(EEDF) has no influence on the atomic line intensities ratio. These EEDFs are canceled each other for both the spieces and the actinometer, hence the ratio of the cross-sections can be used instead of the excitation functions.

Then the atomic density ratio of hydrogen and actinometer can be written as:

$$\frac{n_0^H}{n_0^R} = (\frac{\sigma_i^R X_i^H}{\sigma_i^H X_i^R}) \tag{6.24}$$

The emitted photon numbers per unit volume and time can be determined as:

$$\dot{N}_{ph,i} \propto N_{cal,i} I_{meas} \tag{6.25}$$

with $I_{meas}$ and $N_{cal,i}$ are the measured intensity value of the line and the absolute calibration value of the detection system at the wavelength of the corresponding line respectively.

The optical detection system was absolutely calibrated by means of a tungsten ribbon lamp (OSRAM WI 17/G) in the wavelength range 300 - 900 nm and the results are shown in Fig. (6.14).

The excitation $X_i$ from the ground state is given by:

$$X_i \propto \frac{A_i}{A_{ik}} N_{cal,i} I_{meas} \tag{6.26}$$

Since the constants of proportionality in this equation are the solid angle and the plasma length which are equal for all measured lines, eq. (6.24) can be written as:

$$\frac{n_0^H}{n_0^R} = \left(\frac{\sigma_i^R A_i^H A_{ik}^R N_{cal,i}^H I_{meas}^H}{\sigma_i^H A_{ik}^H A_i^R N_{cal,i}^R I_{meas}^R}\right) \tag{6.27}$$

This is the simple relation of proportionality between the densities $(n_0^H/n_0^R)$ and the corresponding emission intensities $(I_{meas}^H/I_{meas}^R)$ of the atomic ground state species and actinometer, from which we can easily determine the atomic density of the species, i.e. hydrogen in our discharge.

The original (filling) density of the actinometer and of any other mixing gases is given from the gas equation as:

$$PV_x = n_x k_B T \tag{6.28}$$

where $P$ is the gas pressure, $V_x$ is the volume of the $x$ gas of density $n_x$, $k_B$ and $T$ are Boltzmann constant and the gas temperature respectively.

The degree of dissociation is calculated from the ground states of the atomic and molecular hydrogen densities using the relation [108]:

$$k = \frac{n_0^H}{n_0^H + 2n_0^{H_2}} \tag{6.29}$$

The classical actinometric method does not take into account the dissociative excitation of species, which is considered in the following section.

### 6.2.3 Actinometry with consideration of dissociative excitation

In molecular plasmas such as hydrogen, there are two main neutral constituents: $H_2$ and $H$, which are expected to modify the plasma behavior [10]. In low-temperature hydrogen plasmas the dissociative excitation processes must also be taken into account which yields often a very important contribution [48]. Taking into account the dissociative excitation, the excitation $X_i^H$ of the atomic hydrogen can be written as:

$$X_i^H = n_0^H E_i^H + n_0^{H_2} E_i^{H_2} \tag{6.30}$$

$$n_0^H = \frac{X_i^H}{E_i^H} - \frac{E_i^{H_2}}{E_i^H} n_0^{H_2} \qquad and \qquad n_0^R = \frac{X_i^R}{E_i^R} \tag{6.31}$$

Leading to:

$$\frac{n_0^H}{n_0^R} = (\frac{E_i^R X_i^H}{E_i^H X_i^R}) - \frac{n_0^{H_2}}{n_0^R} \frac{E_i^{H_2}}{E_i^H} \tag{6.32}$$

Hence, the atomic hydrogen density is given by:

$$n_0^H = n_0^R (\frac{E_i^R X_i^H}{E_i^H X_i^R}) - \frac{E_i^{H_2}}{E_i^H} n_0^{H_2} \tag{6.33}$$

The first term is the same as in equation (6.24) in case of the classical actinometry. It does not depend on the electron energy distribution function due to the selection of the actinometer, i.e. the definition of the cross-section can be applied. In contrast, the second term contains the ratio of the excitation functions of both the direct and the dissociative excitation of hydrogen. This term is depending on the electron energy distribution function, because both the direct and dissociative excitation processes have cross-sections of different shape and threshold.

Then, taking into account the cross-section values instead of the excitation functions and the system calibration in case of the direct excitation channel, we have:

$$n_0^H = n_0^R (\frac{\sigma_i^R A_i^H A_{ik}^R N_{cal,i}^H I_{meas}^H}{\sigma_i^H A_{ik}^H A_i^R N_{cal,i}^R I_{meas}^R}) - \frac{E_i^{H_2}}{E_i^H} n_0^{H_2} \tag{6.34}$$

The problem in this second term is connected to the determination of the excitation functions of the direct and the dissociative channel of species. These excitation functions can be determined in two different ways, either by using the probe measurements or by our new advanced "two gas actinometry" method as follows:

#### 6.2.3.1 Probe method

The EEDF can be determined by the probe measurements. We can calculate directly the excitation function ratio $E_i^{H_2}/E_i^H$ of the dissociative and the direct contributions from the probe measurements within the energy limits by the probe:

$$\frac{E_i^{H_2}}{E_i^H} = \frac{\int_0^\infty \sqrt{E}\sigma_{exc}^{H_2}(E)f(E)dE}{\int_0^\infty \sqrt{E}\sigma_{exc}^{H}(E)f(E)dE} \tag{6.35}$$

#### 6.2.3.2 Advanced "two gas actinometry"

In this advanced actinometry method, we take into account the direct and dissociative excitation of hydrogen by comparing them with two different atomic actinometers. The first term in eq. (6.34) contains the direct excitation ($H$), which can be compared with its convenient atomic actinometer line ($R$). The dissociative excitation ($H_2$) in the second term will be compared with another atomic actinometer line ($R_T$), which has the same cross section characteristics as follows:

$$X_i^R = n_0^R E_i^R \qquad and \qquad X_i^{R_T} = n_0^{R_T} E_i^{R_T} \tag{6.36}$$

i.e.

$$E_i^H = \frac{\sigma_i^H}{\sigma_i^R} E_i^R \qquad and \qquad E_i^{H_2} = \frac{\sigma_i^{H_2}}{\sigma_i^{R_T}} E_i^{R_T} \tag{6.37}$$

$$E_i^H = \frac{\sigma_i^H X_i^R}{\sigma_i^R n_0^R} \qquad and \qquad E_i^{H_2} = \frac{\sigma_i^{H_2} X_i^{R_T}}{\sigma_i^{R_T} n_0^{R_T}} \tag{6.38}$$

Substituting into eq. (6.34) we get:

$$n_0^H = n_0^R\left(\frac{\sigma_i^R A_i^H A_{ik}^R N_{cal,i}^H I_{meas}^H}{\sigma_i^H A_{ik}^H A_i^R N_{cal,i}^R I_{meas}^R}\right) - n_0^R \frac{n_0^{H_2}}{n_0^{R_d}}\left(\frac{\sigma_i^R \sigma_i^{H_2} A_i^{R_T} A_{ik}^R N_{cal,i}^{R_T} I_{meas}^{R_T}}{\sigma_i^H \sigma_i^{R_T} A_{ik}^{R_T} A_i^R N_{cal,i}^R I_{meas}^R}\right) \tag{6.39}$$

**Choice of the actinometers lines:** Although the emission intensity of the $H$-Balmer-$\alpha$ line is much higher than that of the $H$-Balmer-$\beta$ emission line, it is preferable to use the latter in discharges with high electric fields to determine the degree of dissociation [16]. The basic idea of the advanced "two gas actinometry" is that both of the direct excitation of the $H$-Balmer-$\beta$ (486.1 nm, $E_{th} = 12.7$ eV ) and the krypton $^2p_2$ (826.3 nm, $E_{th} = 12.2$ eV) lines have similar thresholds $E_{th}$

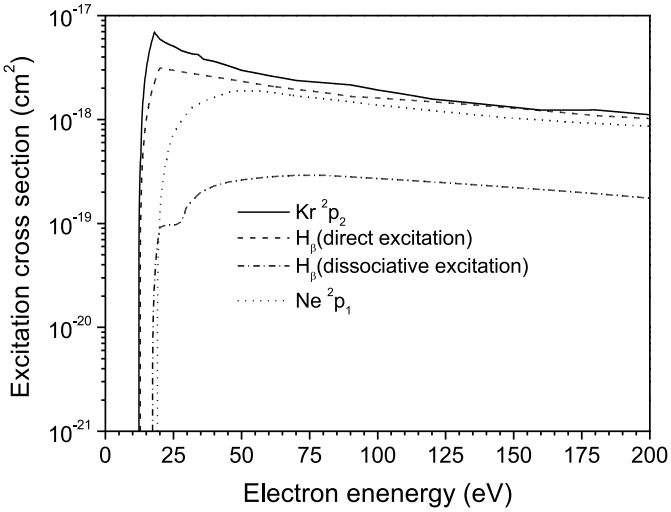


Figure 6.15: Cross sections of the direct [109] and dissociative excitation [110] of the $H$-Balmer-$\beta$ emission line of and the corresponding Kr $^2p_2$ [111] and Ne $^2p_1$ [112] actinometer gases.

and cross section shapes as shown in Fig. (6.15). The dissociative excitation of the $H$-Balmer-$\beta$ (486.1 nm, $E_{th}$=17.2 eV ) line can be compared with the neon $^2p_1$ (585.2 nm, $E_{th}$=19 eV ) line taking into account the same arguments of excitation threshold and the cross section shape. The conditions to apply actinometry are safely fulfilled, for both the direct and the dissociative excitation by comparing the former with the Kr $^2p_2$ and the latter with the Ne $^2p_1$ line.

Then, substituting $R$ and $R_T$ in eq. (6.39) by the direct and the dissociative actinometer lines, i.e. Ne and Kr lines respectively , we obtain the atomic hydrogen density:

$$n_0^H = n_0^{kr}\left(\frac{\sigma_i^{kr} A_i^H A_{ik}^{kr} N_{cal,i}^H I_{meas}^H}{\sigma_i^H A_{ik}^H A_i^{kr} N_{cal,i}^{kr} I_{meas}^{kr}}\right) - n_0^{kr}\frac{n_0^{H_2}}{n_0^{Ne}}\left(\frac{\sigma_i^{kr}\sigma_i^{H_2} A_i^{Ne} A_{ik}^{kr} N_{cal,i}^{Ne} I_{meas}^{Ne}}{\sigma_i^H \sigma_i^{Ne} A_{ik}^{Ne} A_i^{kr} N_{cal,i}^{kr} I_{meas}^{kr}}\right) \tag{6.40}$$

**Effect of quenching:** In gas discharges at elevated pressure (exceeding 10 Pa) radiation-less collisional de-excitation (quenching) can have a strong influence on the population of excited states [80]. The natural lifetime and the quenching

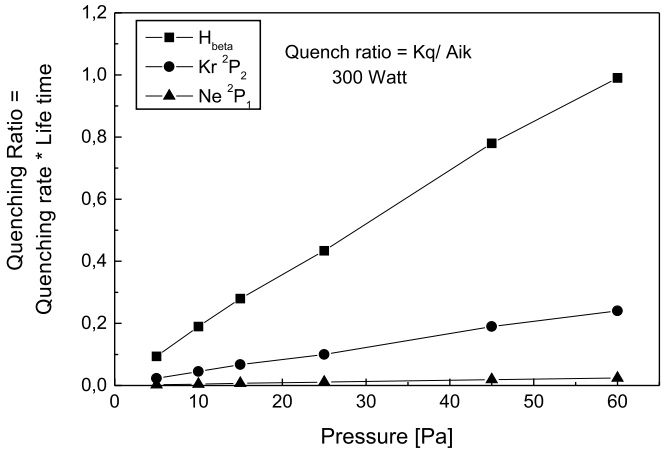


Figure 6.16: The quenching ratio of $H_\beta$, Kr $^2p_2$ and Ne $^2p_1$ lines as a function of pressure at 300 W.

| Excited state | $\lambda\,(nm)$[114] | $E_{Th}\,(eV)$[114] | $\tau_i\,(ns)$ | $k_{H_2}(10^{-10}\,cm^3s^{-1})$ |
|---|---|---|---|---|
| $Kr\,^2p_2$ | 826.3 | 12.2 | 34.1[64, 114] | 9.7[64] |
| $Ne\,^2p_1$ | 585.2 | 19 | 14.5[114] | 2.3[16] |

Table 6.1: The required data of the Kr $^2p_2$ and Ne $^2p_1$ actinometer lines.

coefficient of the Balmer-$\beta$ (n=4) at a gas temperature of 400 K are $\tau_{H_\beta}$= 57.5 ns and $k_{H_2} = 24 \times 10^{-10} cm^3 s^{-1}$ [113]. The wavelength, excitation threshold, life time and the quenching rate of the considered actinometer lines are shown in Table (6.1). The calculated quenching ratio $k_q n_0^{H_2} \times \tau_q$ for the $H_\beta$, Kr $^2p_2$ and Ne $^2p_1$ lines at different power and pressure values are shown in Fig. (6.16).

The quenching ratio has its maximum values at higher pressure and the highest values are obtained for $H_\beta$ followed by the Kr $^2p_2$ values. The minimum quenching values are obtained for the Ne $^2p_1$ line. The quenching rate is already included for all power and pressure variations within our calculations of the degree of dissociation.

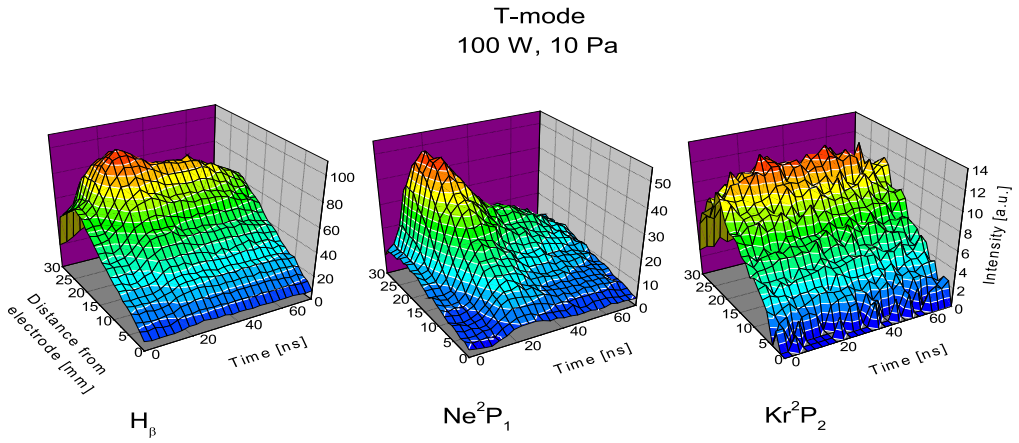


Figure 6.17: Time and space resolved emission intensity of $H_\beta$, Kr $^2p_2$ and Ne $^2p_1$ lines in the transition mode at 100 W and 10 Pa.

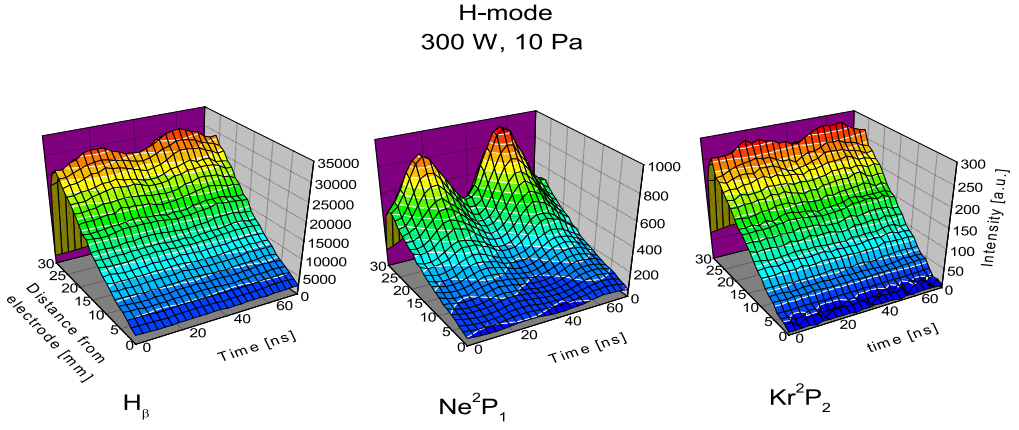


Figure 6.18: Time and space resolved emission intensity of $H_\beta$, Kr $^2p_2$ and Ne $^2p_1$ lines in the inductive mode at 300 W and 10 Pa.

The measured emission intensities of the $H_\beta$, Kr $^2p_2$ and Ne $^2p_1$ lines, which are used for the determination of the degree of dissociation in both the transition T-mode (100 W, 10 Pa) and the inductive H-mode (300 W, 10 Pa) are shown in Fig. (6.17) and Fig. (6.18) respectively. Here, we have to mention that the time behavior of the Ne $^2p_1$ line is much stronger than that of $H_\beta$ and the Kr $^2p_2$. The emission intensity ratios ( $H_\beta$: Ne $^2p_1$: Kr $^2p_2$) at time and position of maximum emission are about (1 : 0.5 : 0.15) and (1 : 0.03 : 0.009) in the T- and H- mode respectively.

The lower emission intensity of the Kr $^2p_2$ line referrers to its lower amount in the working gas. An excess of the added Kr $^2p_2$ gas easily changes the characteristic of the discharge.

**Drawback of the present method:** As mentioned before, the excitation cross-section of the dissociative excitation of the $H_\beta$ line has a threshold of $E_{th}$=17.2 eV, which is still a little bit different from the excitation threshold of the corresponding Ne $^2p_1$ actinometer line with a threshold energy $E_{th}$=19 eV. Hence there is a difference (about 1.8 eV) in the excitation thresholds of both of them. This means that there is a small amount of the dissociative excitation is not considered with our assumption.

### 6.2.4 Dissociation degree measurements

The three mentioned methods used for the determination of the degree of dissociation are summarized as follows:

1. Classical method, which takes into account the Kr $^2p_2$ line as an actinometer for the direct contribution ($\sigma_i^{Kr}/\sigma_i^H$).

2. Probe method, since we used the measured EEDF for calculation of the excitation function ratio of the dissociative and direct contribution ($E_i^{H_2}/E_i^H$) within the valid energy range of the Langmuir probe data.

3. Advanced "two gas actinometry" method, which takes into account the Kr $^2p_2$ actinometer line for the direct contribution ($\sigma_i^{Kr}/\sigma_i^H$) and the Ne $^2p_1$ actinometer line for the dissociative contribution ($\sigma_i^{H_2}/\sigma_i^{Ne}$).

The atomic hydrogen density and the degree of dissociation as a function of power at 10 Pa for the direct, advaned "two gas actinometry" and the probe methods

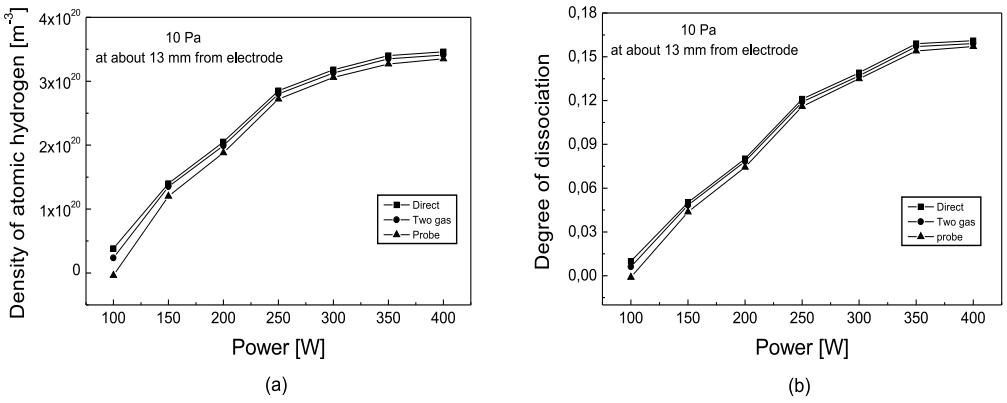


Figure 6.19: Density and Degree of dissociation of different actinometric methods at 10 Pa as a function of power at the probe position.

are shown in Fig. (6.19). The EEDF probe measurements at a position of about 13 mm from the grounded electrode are used to calculate for the second term of eq.(6.34).

First of all we have to remember that at 10 Pa and 100 W the discharge is ignited in the transition mode, then it switches directly to the inductive mode. As shown from figure, it is valid to use both the direct and the advanced "two gas actinometry" methods for determination of atomic hydrogen density (i.e. the degree of dissociation) within the whole energy range. The probe method at this low power (100 W) gives nonphysical results in calculation of the atomic hydrogen density, hence in results of the degree of dissociation. It must be mentioned here that the cross section values used to calculate eq. (6.40) are the maximum values for Kr $^2p_2$, $H_\beta$ (direct excitation) and Ne $^2p_1$, but for $H_\beta$ (dissociative excitation) the cross section value corresponding to an electron energy of 26 eV is taken into account during the calculations. If the cross section of $H_\beta$ (dissociative excitation) is chosen to take its maximum value like other lines (i.e. value corresponding to an electron energy of about 60 eV), the advanced "two gas actinometry" gives also nonphysical results as the probe method.

The density derived by the different methods rises with increasing the applied

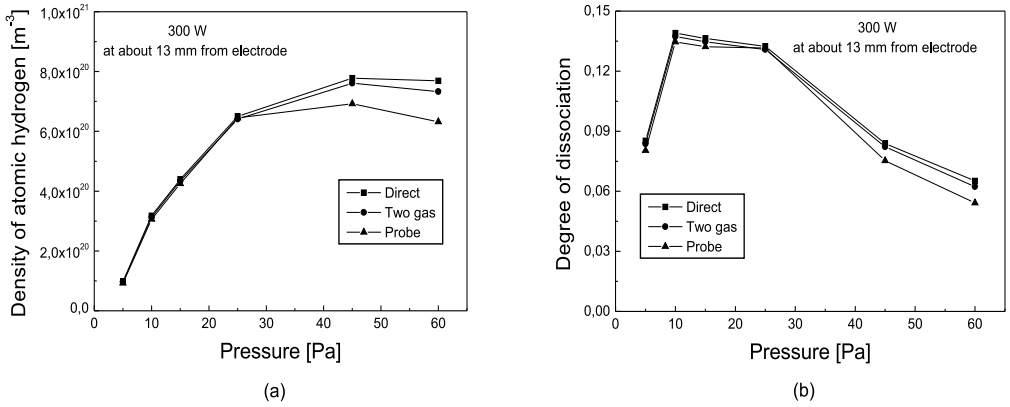


Figure 6.20: Density and Degree of dissociation of different actinometric methods at 300 W as a function of pressure at the probe position.

power. A rapid increase of the atomic density is observed with increasing of power up to 250 W. For powers more than 250 W, a slow increase in the density is obtained. Maximum density of about $3.5 \times 10^{20}\, m^{-3}$ is calculated for 400 W at pressure of 10 Pa. The direct method normally gives the highest density values, since it is based only on the calculations of the first term of eq. (6.40). Moreover, a degree of dissociation of about 1 % is obtained for the direct method at 100 W. Degree of dissociation of about 12 % is obtained at 250 W for the "two gas actinometry". Higher values of more than 15 % are obtained at higher power. The atomic hydrogen density and dissociation degree values obtained by the advanced "two gas actinometry" method are always intermediate between both results of the direct and the probe methods.

The results of the atomic density and degree of dissociation for the three methods at 300 W with different pressures are shown in Fig. (6.20 a and b). The pressure dependence of the density and degree of dissociation is somehow different from the power dependence. In case of density, we can say that the results of the three actinometric methods coincide at low pressure range (5 - 25 Pa). At high pressures (more than 25 Pa) the density calculated by the probe method deviates from other methods. At 45 and 60 Pa a density of about $8 \times 10^{20}\, m^{-3}$

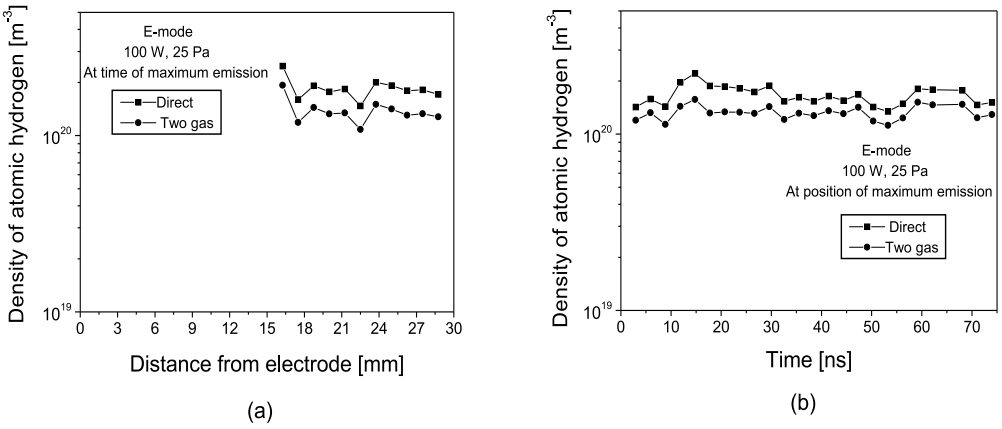


Figure 6.21: Axial and time behavior of the atomic hydrogen density obtained by the direct and advanced actinometry methods in the capacitive E-mode at 100 W, 25 Pa.

is obtained using the direct method. A little smaller densities are calculated using the advanced "two gas actinometry" method at these pressures. The density obtained by the probe method has value within the range of $6 \times 10^{20}\, m^{-3}$ at 60 Pa. The degree of dissociation shown in Fig. (6.20 b) reveals value of about 8 % at 5 Pa for the direct and the advanced "two gas actinometry" methods. Higher values of about 13 % are obtained within the pressure range from 10 Pa to 25 Pa. The degree of dissociation calculated by the three methods is decreased rapidly by rising the pressure to reach its minimum value about 6 % at 60 Pa. The degree of dissociation obtained by the probe has a slightly lower value especially at higher pressure as a result of the lower calculated atomic density.

The conclusion of this first part of the dissociation measurements is focused on the validity of the probe measurements for the calculation of the degree of dissociation. Although the probe results are always comparable with our advanced "two gas actinometry" method, it has drawback points:

1. First of all the probe as mentioned in chapter 2 is an intrusive method, i.e. a massive object is inserted inside the plasma vessel. This might influence the plasma.

2. The probe has a limitation in the electron temperature. It can not measure properly above this limit, i.e. the electron energy will be limited for a range of values, that could be in some cases below the cross-section threshold of our lines of interest.

3. The probe gives localized and time integrated results, so it is not possible to perform such axial and time dependence, which is guaranteed by the direct and the advanced two gas methods.

4. The probe gives nonphysical results in low density modes (i.e. in both the capacitive E-mode and the transition T-mode).

For these reasons, the probe method is not the best method in calculating atomic density and the degree of dissociation. In the following, we will concentrate on the axial and time dependencies of the atomic hydrogen density and degree of dissociation.

As a result of lower emission intensity measured in the capacitive mode, the calculations of the atomic hydrogen density by both the direct and the advanced "two gas actinometry" methods is only avaailable 15 mm above the electrode as shown in Fig. (6.21 a). There is no pronounced time behaviour within the RF cycle as shown in Fig. (6.21 b). The difference between the calculated density by the direct and the advanced method is less than $0.5 \times 10^{21} m^{-3}$.

Fig. (6.22 a and b) shows the axial behavior of the atomic hydrogen density and degree of dissociation calculated by the direct and advaned "two gas actinometry" methods in the T- and H-mode. Here it is clear that calculations of the density and the degree of dissociation is available at about 8 mm above the electrode. There is a big different between the density obtained by the direct and the advanced "two gas actinometry" methods in the transition mode in comparision with results in the H-mode. The density obtained by the direct and the advanced methods in the inductive mode coincides (note log. scale) with each other giving atomic density value of about $6 \times 10^{21} m^{-3}$.

The degree of dissociation obtained by the advanced "two gas actinometry" method in the T-mode shows values of about 2 %, meanwhile the direct method yields values of about 2.5 %. In the H-mode the degree of dissociation has values between 10 and 11 % with a much less difference between the two methods than in the E-mode. There is no pronounced axial dependence in the atomic hydrogen density either in the T- or H-mode.

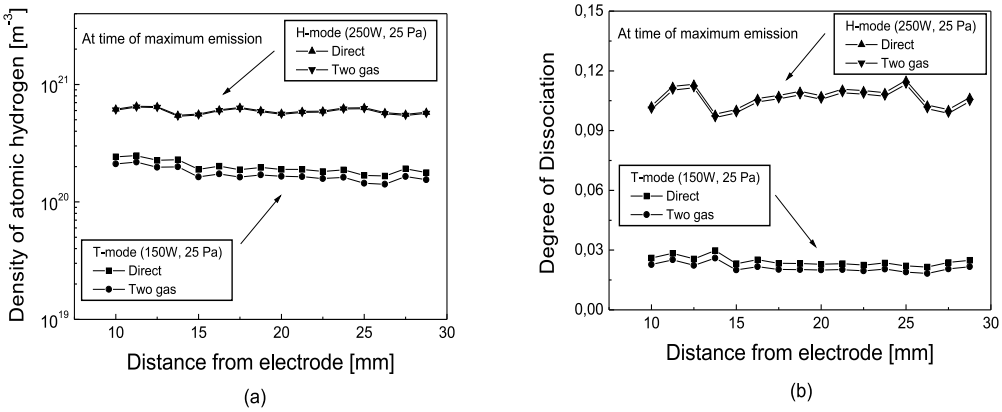


Figure 6.22: Axial behavior of (a) the atomic hydrogen density and (b) the degree of dissociation obtained by the direct and advanced actinometry methods in the T- and H-mode.

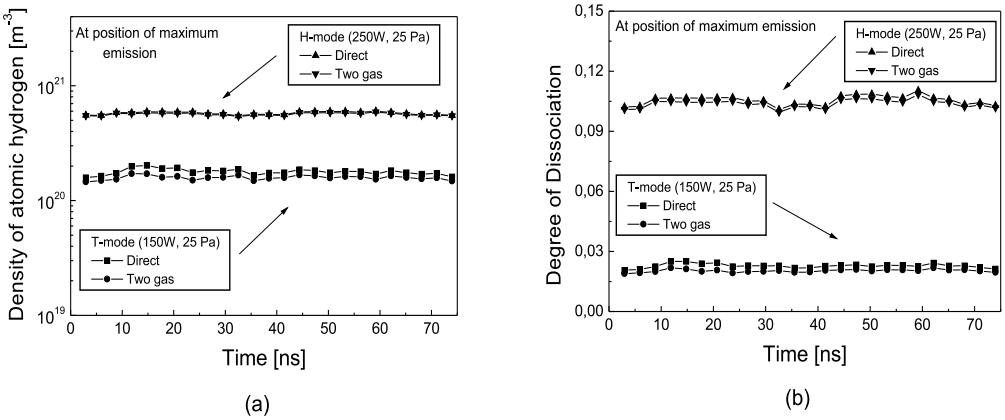


Figure 6.23: Time behavior of (a) the atomic hydrogen density and (b) the degree of dissociation using both of the direct and advaned actinometry methods in the T- and H-mode.

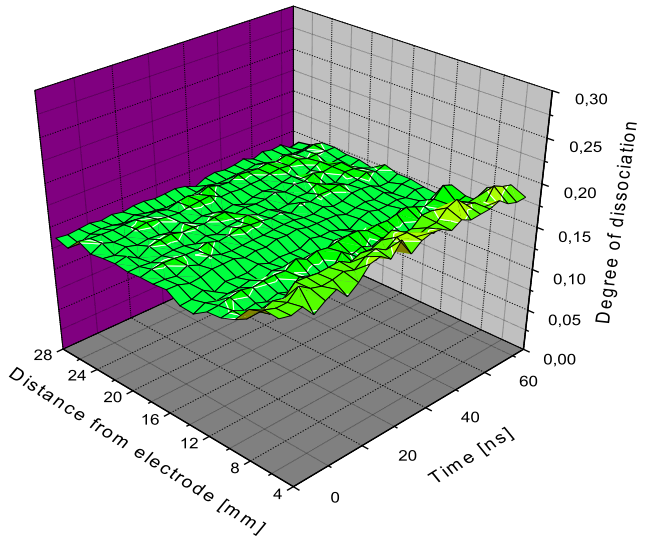


Figure 6.24: Time and axial dependence of the degree of dissociation obtained with the advaned two gas actinometry method at 300 W and 10 Pa.

The time behavior of the atomic hydrogen density and the degree of dissociation in the transition and in the inductive modes obtained by the direct and the advanced methods is shown in Fig. (6.23 a and b). Although there is a time dependencies in the emission intensities of the lines used in these calculations of the atomic densities in different discharge modes (E-, T-, H-mode). Here it is clear that in both the T- and H-mode there is no change in the density and dissociation degree within the time scale of the RF cycle as in case of the capacitive mode shown in Fig. (6.21).

As a conclusion of these actinometry measurements, the advanced "two gas actinometry" method is considered to be a good improvement of the compared ones in determination of the atomic hydrogen density and dissociation degree since:

- It has much less assumptions by considering the dissociative excitation contribution, which is not included by the direct (classical) actinometric method.
- It gives line-of-sight integrated values.

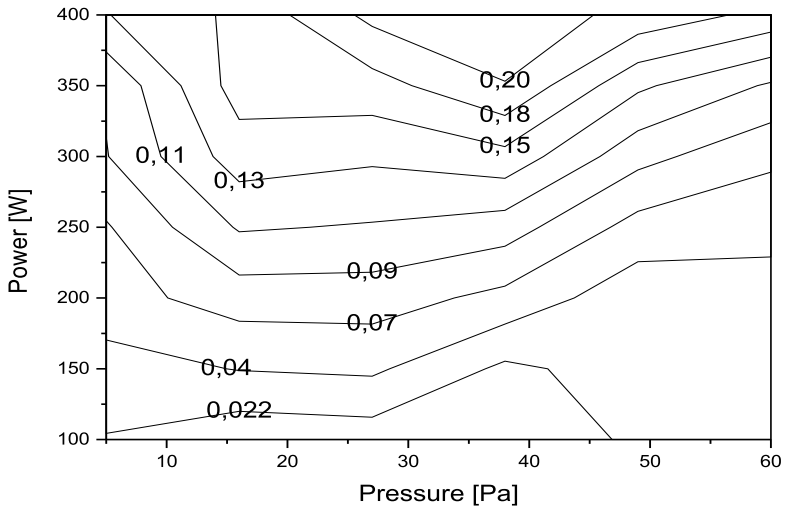


Figure 6.25: The power and pressure dependence of the degree of dissociation calculated by the advanced "two gas actinometry" method.

- It is a non-intrusive method, i.e. there is no disturbance of the plasma under consideration.
- It is not restricted to a finite energy range like the probe method but it covers the whole energy range with the given cross-section data.

The time and space resolved dissociation degree calculated by the advanced "two gas actinometry" method in the H-mode at 300 W and 10 Pa is shown in Fig. (6.24). The dissociation degree has a constant value "within the range of 15 %" except near the electrode, where it increases to reach about 17 % at 5 mm distance from the electrode.

The effect of power and pressure on the degree of dissociation measured by "two gas actinometry" is shown in Fig. (6.25). Here it is clear that the lowest dissociation degree is obtained at lower power (below 150 W). We know that with this power the discharge is ignited in the E-mode with dissociation degree less than 3 %. The degree of dissociation is increased dramatically by rising the power for the whole pressure range. In the intermediate pressure, the dissociation degree is increased more rapidly than on both pressure sides. A maximum dissociation degree of about 20 % is obtained at pressure of 45 Pa and 400 W, although a very

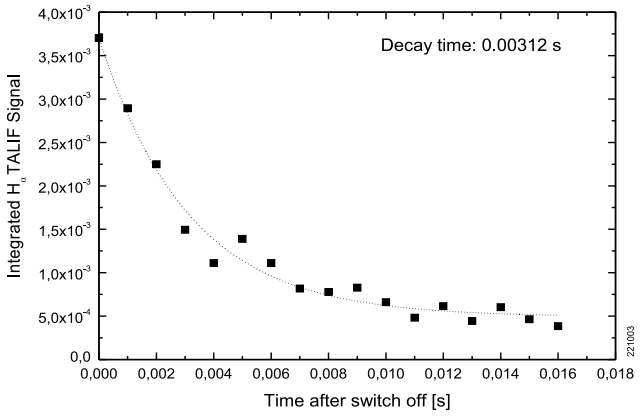


Figure 6.26: The time behaviour of the H atom density after switch of the plasma.

low dissociation degree is obtained at the same pressure at low power.

### 6.2.5 Comparison with TALIF measurements

An independent measurement by two-photon laser induced fluorescence (TALIF) is performed to determine the ground-state densities of the atomic hydrogen in order to compare the actinometry results with TALIF results. The well-known two-photon resonance of atomic hydrogen has a corresponding transition in krypton; both transitions are investigated in order to calculate the required atomic hydrogen density. In this study, two-photons of the laser ($\lambda = 2 \times 205.1\,nm$) radiation are simultaneously absorbed to pump the $1s\,^2S_{1/2} - 3d\,^2D_{3/2,5/2}$ transition of the hydrogen atom, which is calibrated with the selected $1p^6S_0^1 - 5p^{'}[3/2]_2$ transition in Krypton ($\lambda = 2 \times 204.2\,nm$). The fluorescence radiation of the $3d\,^2D_{3/2,5/2} - 2p\,^2P_{1/2,3/2}$ hydrogen transition at $\lambda = 656\,nm$ and the $5p^{'}[3/2]_2 - 5s^{'}[1/2]_1$ krypton transition at $\lambda = 826.3\,nm$ depopulate the excited levels.

The measurement is done at 250 W and 25 Pa, in order to measure the $H_\alpha$ signal. The $H_\alpha$ TALIF signal as a function of time after switch off the plasma is shown in Fig. (6.26). An exponential decay time ($\tau$) of about 0.00312 s is obtained.

Calibration is done by using the krypton gas at a pressure of 5 Pa without

igniting the plasma (and without gas flowing). The krypton density in this case at room temperature is calculated according to the gas equation as:

$$n_{Kr} = \frac{P}{kT} \tag{6.41}$$

A krypton density of about $1.2 \times 10^{21}\, m^{-3}$ corresponds to 5 Pa Kr.

The hydrogen atomic density is calculated from the following equation:

$$n_H = \gamma(\frac{\sigma_{Kr} a_{ik}^{kr} H_{signal}}{\sigma_H a_{ik}^{H} Kr_{signal}})\, n_{Kr} \tag{6.42}$$

where $\gamma$ is the detection sensitivity, which depends on the quantum efficiency of the used photomultiplier tube (PMT) and the filter transmission and is given by:

$$\gamma = \frac{T_{Kr}\eta_{Kr}}{T_H \eta_H} \tag{6.43}$$

where $T_H$ and $T_{Kr}$ are the transmission of the $H_\alpha$ and Kr filters (50 % and 80 % respectively), The Hamamatsu R995 PMT has quantum efficiency ratio $\frac{\eta_H}{\eta_{Kr}} = 2.5$ [115].

The cross-section ratio $\frac{\sigma_{Kr}}{\sigma_H}$ has the value of 0.84 and the optical branching ratio of both the $H_\alpha$ and Kr lines are given by $a_{ik}^H = 0.88$ and $a_{ik}^{kr} = 0.95$ [115].

The results of the measured $H_\alpha$ and Kr signal 0.001 s after switch off the plasma as a function of square of the laser pulse energy are shown in Fig. (6.27). From the linear relation of the $H_\alpha$ and the Kr signal we can calculate the slope of these two lines to get the ratio $\frac{H_{signal}}{Kr_{signal}} = \frac{0.01885}{0.05826}$. The density of the $H_\alpha$ line 0.001 s after switch off the plasma is then calculated to be about $2.25 \times 10^{20} m^{-3}$. The density directly after switch off the plasma (t = 0 s) is given by:

$$n_H(t) = n_H(0) exp(-t/\tau) \tag{6.44}$$

The degree of dissociation is calculated from eq. (6.29) and it has a value of about 4.85 % with a factor of two deviation from the actinometry results. The same factor is obtained in determination of the degree of dissociation in a CCRF discharge between emission spectroscopy and TALIF measurements [16, 115]. The reason might be related to the line-of-sight OES measurements in comparision to the local TALIF measurements.

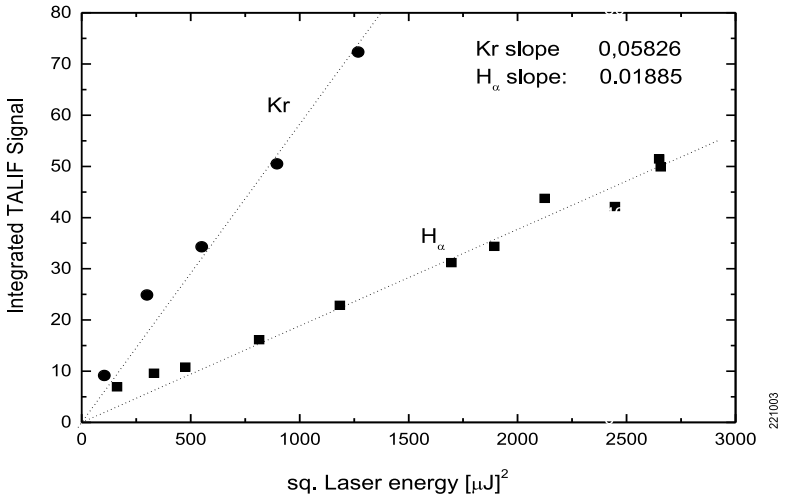


Figure 6.27: The $H_\alpha$ and Kr TALIF signals as a function of the square of the laser pulse energy.

### 6.2.6 Determination of electron temperature by OES

Determination of the electron temperature by trace-rare gases optical emission spectroscopy (TRG-OES) method using Ar, Kr and Xe lines is reported [116, 117, 118, 119, 120]. In these publications, the electron temperature was obtained as an adjustable parameter in a model that computes the measured emission intensities of Ar, Kr and Xe lines and finds the best match to the experimental measurements. The possibility to calculate the electron temperature from the ratio of two rare-gas line intensities was also mentioned. Since we use the two actinometer lines Kr $^2p_2$ (826.3 nm) and Ne $^2p_1$ (585.2 nm) with excitation cross section thresholds of 12.2 eV and 19 eV respectively, we have the possibility to calculate the electron energy. This calculation will be valid for the corresponding energy range (12.2 to 19 eV). The electron temperature is calculated as a fit parameter in comparing the two emission intensities of the actinometer lines assuming a Maxwellian EEDF. The calculated ratio of the excitation rate coefficients of the Ne $^2p_1$ and Kr $^2p_2$ lines as a function electron energy is shown in Fig. (6.28). Except at low electron energy (less than 2 eV) a linear dependence is obtained. The way for calculating the electron energy is summarized as follows:

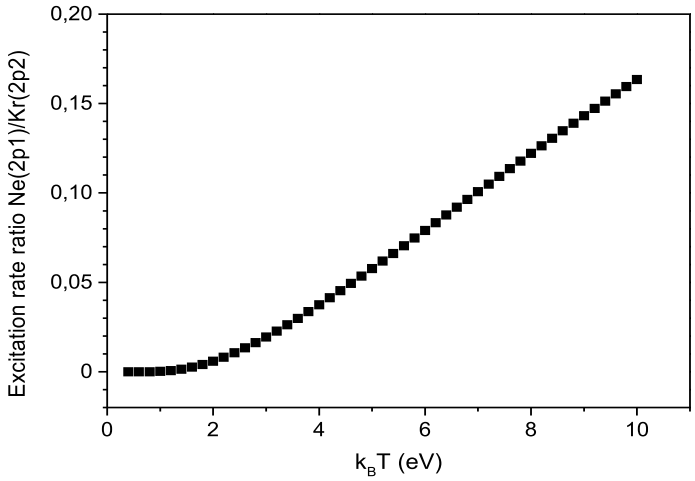


Figure 6.28: The dependence of the excitation rate coefficient ratio of Ne $^2p_1$ and Kr $^2p_2$ lines on the electron energy.

The population $n_i$ in an excited state under stationary conditions is given as mentioned before as:

$$n_i = n_0 \frac{E_i}{A_i} \tag{6.45}$$

where $E_i$ is the excitation function, given as:

$$E_i = n_e \int_0^\infty \sigma_{exc}(E) \sqrt{\frac{2E}{m_e}} f(E) dE \tag{6.46}$$

with $E$ the electron energy and $f(E)dE$ is the electron energy distribution function, which in case of a Maxwellian distribution can be written as:

$$f(E) = 2\sqrt{\frac{E}{\pi (k_B T_e)^3}} exp[-\frac{E}{k_B T_e}] \tag{6.47}$$

Now we can express the excitation function:

$$E_i = n_e \sqrt{\frac{8}{\pi m_e (k_B T_e)^3}} \int_0^\infty E \sigma_{exc}(E) exp[-\frac{E}{k_B T_e}] dE \tag{6.48}$$

This leads to:

$$n_i = \frac{n_e n_0}{A_i}\sqrt{\frac{8}{\pi m_e (k_B T_e)^3}}\int_0^\infty E\sigma_{exc}(E)exp[-\frac{E}{k_B T_e}]dE \tag{6.49}$$

The measured emission intensity of a transition can be written as:

$$I_{ij} \propto n_i A_{ij} N_{cal} \tag{6.50}$$

where $I_{ij}$, $N_{cal}$ and $A_{ij}$ are the measured intensity, the calibration factor of the detection system and the transition probability of the investigated line respectively.

This leads to:

$$I_{ij} \propto n_e n_0 \frac{A_{ij}}{A_i} N_{cal}\sqrt{\frac{8}{\pi m_e (k_B T_e)^3}}\int_0^\infty E\sigma_{exc}(E)exp[-\frac{E}{k_B T_e}]dE \tag{6.51}$$

The electron temperature in our case can be obtained by comparing the measured Ne and Kr actinometer line intensities:

$$\frac{I_{ij}^{Ne}}{I_{ij}^{Kr}} = (\frac{n_0^{Ne}(\frac{A_{ij}}{A_i})^{Ne} N_{cal}^{Ne}}{n_0^{Kr}(\frac{A_{ij}}{A_i})^{Kr} N_{cal}^{Kr}}).(\frac{\int_0^\infty E^{Ne}\sigma_{exc}^{Ne}(E)exp[-\frac{E^{Ne}}{k_B T_e}]dE}{\int_0^\infty E^{Kr}\sigma_{exc}^{Kr}(E)exp[-\frac{E^{Kr}}{k_B T_e}]dE}) \tag{6.52}$$

All values included in the first term are known. The second term is the excitation rate ratio of the Ne and Kr lines. The integration is performed numerically in the given energy range. At the end we get the electron temperature as a fit parameter in equating both the measured intensity ratio (left hand side) and the calculated term (right hand side).

The results of the electron energy as a function of axial position and time of RF cycle in the T- and H-mode shown in Fig. (6.29) reveals an electron temperatures below 6 eV. Axially at time of maximum emission, the T-mode shows an electron temperatures higher than these obtained for the H-mode except close to the grounded electrodes. The disturbance near the grounded electrode in T-mode might be caused by the lower intensity of the Kr $^2p_2$ line. There is a small increase in the electron energy after 10 mm from the grounded electrode towards

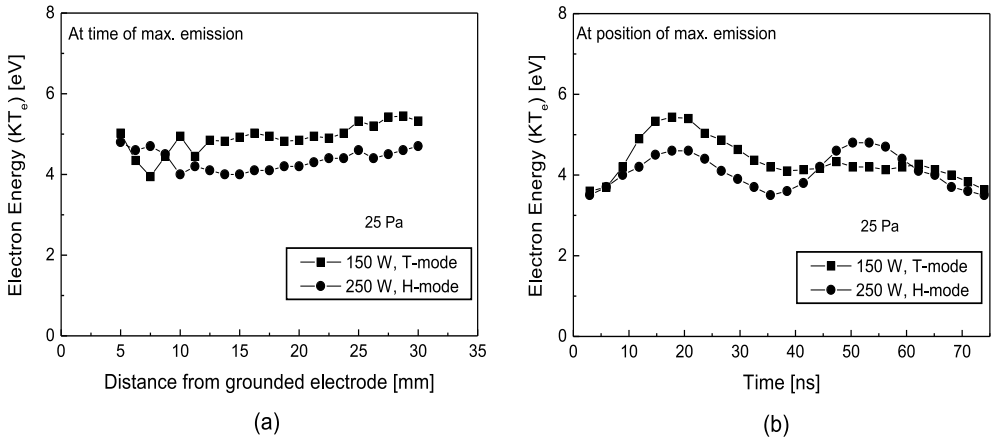


Figure 6.29: Calculated electron energy as a function of (a) distance from the grounded electrode and (b) time of RF cycle.

the coil. Above 10 mm distance from the grounded electrode, the T-mode reveals energy of more than 5 eV, wheres the H-mode has 1 eV less. Time resolved results at position of maximum emission gives the normal time behavior as the emission in discharge modes. At time of maximum emission (about 18 nm) an electron energy of about 5.5 eV is obtained in the E-mode. A very small change in the calculated energy is obtained within the time of 35 nm to 60 nm with energy of about 4 eV. A decrease in the calculated energy is obtained for the rest of the time period. On the other hand, in the inductive mode at times of maximum emission (about 18 and 53 nm) an electron energies of about 4.5 eV are obtained. Energies of about 3.5 eV are obtained at the beginning and at the end of the period, also in between the two maximum.

The power and pressure dependence of the calculated electron energy is shown in Fig. (6.30 a). It is clear that the lower electron energy values are obtained at the diagonal of the figure, in particular at low power and low pressure values as well as at high power and high pressure. Electron energy of about 5 eV is obtained at power more than 250 W within the pressure range from 10 Pa to 40 Pa. Looking at the lower part of the figure, it is clear that a steep increase in energy is obtained with decreasing power and increasing pressure. High energies of more than 7 eV

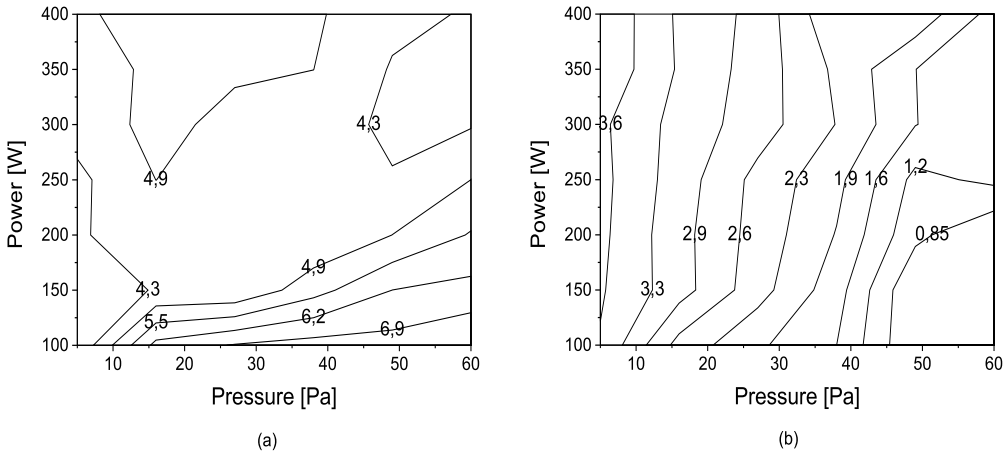


Figure 6.30: Electron energy as a function of power and pressure (a) calculated by OES (b) measured by the probe.

are obtained at the lowest power (100 W) and the highest pressure (60 Pa). In comparison with the calculated electron energy, the probe measurements of the electron temperature under the same conditions are shown in Fig. (6.30 b). The probe measurements show approximately the same values at lower pressure (up to 10 Pa) within power variation. In the range between 10 and 25 Pa at high power (more than 150 W) the probe gives about 1 eV less than the calculated ones. At low power within the same pressure range the probe results show much lower electron temperatures than the calculated energies. At pressure more than 25 Pa the probe measurements deviate completely from the spectroscopic results for all power variations. Lower temperatures of less than 1 eV are obtained at low power and at high pressure (60 Pa). From this we can say, that any power variations doesn't disturb the smart soft Langmuir probe measurements at lower pressures. At higher pressure (more than 25 Pa) the probe doesn't work properly under our conditions.

# Chapter 7

## Summary and conclusions

In this thesis spectroscopic studies of inductively coupled hydrogen plasma discharges have been presented. Different topics such as the transition phenomena and results for both the gas temperature and the degree of dissociation have been discussed. In this chapter a survey of general conclusions will be given.

**Transition phenomena:** Inductively coupled RF-discharges exhibit different distinct modes of operation: In addition to the capacitive mode (E-mode) and the inductive mode (H-mode), there is another intermediate mode we call the transition mode (T-mode). The applicability of optical emission spectroscopy (OES) technique to follow temporally and spatially the transition phenomena has been proved. The conditions required to support different discharge modes can be determined by OES.

A distinction between E-mode, T-mode or H-mode operation is possible from the temporal structure of the emission and by intensity. The E-mode is characterized by a faint optical emission and by the evolution of one emission maximum per RF-cycle ($t_{RF} = 74ns$) attributed to the fast electrons expelled by the sheath. As a result of the currents induced twice per period in the discharge, another emission maximum appears in the H-mode discharge. During the T-mode the second emission maximum starts to built up. The H-mode is about 2 orders of magnitude higher than other modes in intensity. A pronounced capacitive effect appears at low power (100 W) and high pressure (60 Pa). Structures related to sheath expansion and fast secondary electrons in case of $H_\alpha$ emission line are clearly observable. The second structure caused by fast secondary electrons does not appear in case of emission of the molecular hydrogen Fulcher Q[1] (v=2) line.

Measurements of the electron density and electron temperature in addition to the EEDF are obtained by the Smart Soft Langmuir Probe. These measurements are in a good agreement with OES measurements for various discharge modes, since a high electron density in the range of $10^{11}\,m^{-3}$ is measured for the H-mode compared to about $10^{9}\,m^{-3}$ in both the E- and T-modes. The shape of the EEDF changes in our measurements during the transition, with a switch from a Maxwellian-like distribution in the H-mode to a Druyvesteyn-like distribution in both T- and E-mode. The transition from the different discharge modes shows a hysteresis, studied by measuring the power required to sustain the plasma in the E- and H-mode at different pressures. There is no instability observed in our ICP - $H_2$ discharge under our operating conditions of powers and pressures.

**Gas temperature:** The gas temperature is determined by optical emission spectroscopy (OES) based the Q-branch transitions ($\triangle N = 0$) of the diagonal bands ($\triangle v = 0$) of the Fulcher-$\alpha$ system ($3p\,^3\Pi_u^- \rightarrow 2s\,^3\sum_g^+$electronic transition) of $H_2$. An analysis of the temperature from emission intensity measurements was performed as a function of time and position between the electrodes using the first five rotational lines.

At 45 Pa a much stronger emission modulation of about 80 % of the Q[1] Fulcher-$\alpha$ (v=2) line is obtained in the E-mode as compared to about 20 % is obtained at 10 Pa. The emission modulation obtained in the H-mode at 45 Pa is reduced to about 40 %. Under some conditions (low power, high pressure, near the cooled electrode) it was not possible to calculate a rotational temperature, because the emission was too faint as a result of the low power transfer near the electrode. In the E- and T-mode the rotational temperature assumes values in the range of about 350 to 450 K near the coil. Cooling of both the grounded electrode and the antenna coil has pronounced effects under low power conditions. In the inductive mode, the rotational temperature has higher values increasing with rising power. A temperature of about 700 K (near the coil) is reached at 300 W. At 400 W a plateau area with values of approximately 850 K near the coil is obtained. This area expands up to about 15 mm distance from the coil, afterwards a gradual decrease in the rotational temperature is noticed axially towards the grounded electrode. A temperature gradient of more than 200 K is observed axially between the antenna coil and the electrode. At high power the energy is deposited deeper into the volume between coil and electrode. At the

same time the electrode and the vessel are heated more so that the cooling by the electrode becomes less effective.

Rotational temperature measurements exhibit no time dependence within a time scale of the RF period ($\tau_{RF} = 74ns$) in either of the discharge modes at low pressure (10 Pa). At 45 Pa there is a small time dependence within the range of about 20 K near the exciting coil at time and position of maximum emission. A modulation of about 100 K is obtained in case of a CCRF discharge using the same program applying the same algorithms. The observed time modulation in the CCRF discharge was explained to be due to a change of the rotational distribution of the upper levels, which can occur by collisions of excited molecules with other molecules or by additional population of the excited rotational levels by cascading processes from higher states [11]. On the basis of a simplified numerical model the time behavior in both CCRF and ICP discharges has been explained quite well. The half-width of the excitation maxima of about 20 ns is in good agreement with the measurements. A contribution by the cascades of about 8% yields a modulation of the emission that agrees very well with the observed one for the H-mode of the ICP as well for the CCRF discharges and for different pressures. For the CCRF discharge due to the long time between excitation pulses the temperature variations are large ($\Delta T \approx 90$ K), since the relative contribution from the cascades increases because of the longer lifetime of these states. The temperature at maximum excitation is very close to the ground state temperature. Due to the higher excitation frequency in the ICP, the variation of the relative contribution to the population is reduced resulting in temperature variations of about 20 K for our conditions which is within the estimated error of our temperature measurements. There is a continuous contribution for the Fulcher states in the ICP resulting in a more pronounced deviation from the ground state temperature as compared to the CCRF discharge.

The results of the gas temperatures obtained from Fabry-Perot interferometry (FPI) are in a very good agreement with the measurements from the analyses of the rotational Fulcher-$\alpha$ (v = 2) band. Hence temperature analyses from the rotational bands yield results that reflect the real gas temperature for our discharge.

The radial homogeneity of the gas temperature within a plateau region of about 35 mm radius has been identified by application of the Abel inversion algorithm. The radius of this region is correlated with the outer radius of the exciting coil.

The main power input into the discharge takes place in the volume below the coil. For higher radial distances the temperature falls off. Outside the discharge at about 60 mm from the axis the temperature is connected to the vessel temperature which rises with input power meaning that more energy is transported outside to the walls.

**Dissociation degree:** The classical actinometric method is used to calculate the degree of dissociation during this work. This method is improved by consideration of dissociative excitation which is done by using two different methods. The first method is based on the probe. In this method the excitation functions of both the direct and the dissociative contributions have been calculated using the EEDF results from the probe measurements. The second method is based on the introduction of another actinometer gas to take account of the dissociative contribution of hydrogen. This method we called an advanced "two gas actinometry". In this advanced "two gas actinometry" method the conditions to apply actinometry were fulfilled for both the direct and the dissociative excitation of the $H$-Balmer-$\beta$ emission line taking into account the Kr $^2p_2$ line as an actinometer for the direct excitation and the Ne $^2p_1$ line as the second actinometer for the dissociative excitation. The quenching rate is included for all power and pressure variations within our calculations of the degree of dissociation.

The results of the atomic density and the degree of dissociation at a position of about 13 mm from the grounded electrode for the three methods have been compared. The direct method normally gives the highest density values (i.e. the highst degree of dissociation). Results obtained by the advanced "two gas actinometry" method are always intermediate between both results of the direct and the probe methods. As a result of lower emission intensity measured in the capacitive mode, the calculations of the atomic hydrogen density is only available 15 mm above the electrode. In comparison to other discharge modes (T- and H-mode) the calculations are available at about 8 mm above the electrode. There are no pronounced axial or time dependencies in the atomic hydrogen density and the degree of dissociation within the time scale of the RF cycle in either E-, T- or H-mode. There is a big difference between the density obtained by the direct and the advanced "two gas actinometry" methods in the transition mode in comparison with results in the H-mode. The density obtained by the direct and the advanced methods in the inductive mode coincides giving atomic

density values of about $6 \times 10^{21} m^{-3}$. The degree of dissociation obtained by the advanced "two gas actinometry" method in the T-mode shows values of about 2 %, meanwhile the direct method yields values of about 2.5 %. In the H-mode the degree of dissociation has values between 10 and 11 % with a much smaller difference between the two methods than in the T-mode. This means that the correction obtained by the advanced "two gas actinometry" has a big effect in low density modes. Hence this method will be a very convenient method in case of the CCRF discharges. Both the direct method and the probe methods are not preferred in calculations of the degree of dissociation because the first method neglects the dissociative excitation contribution. The probe method takes into account the dissociative excitation but is an intrusive method. It is restricted to a finite energy range and it gives a non-physical result in low density modes. The advanced "two gas actinometry" method is considered to be a good improvement compared to the other methods in determination of the atomic hydrogen density and dissociation degree.

An independent measurement by two-photon laser induced fluorescence (TALIF) has been performed to determine the ground state densities of the atomic hydrogen in order to compare the actinometry results with TALIF results. The degree of dissociation calculated by TALIF measurement at 300 W and 25 Pa has a value of about 4.85 % with a factor of two deviation from the actinometry results. The reason might be related to the line-of-sight OES measurements in comparison to the local TALIF measurements.

Comparing both Kr $^2p_2$ (826.3 nm) and Ne $^2p_1$ (585.2 nm) lines the electron temperature has been determined. the calculation is valid for the corresponding energy range (12.2 to 19 eV). The results are compared with the probe results. Axially at time of maximum emission, the T-mode shows electron temperatures higher than those obtained for the H-mode. High energies of more than 7 eV are obtained at the lowest power (100 W) and the highest pressure (60 Pa). The probe measurements show approximately the same electron temperature values at lower pressure (up to 10 Pa) within power variation. At higher pressure the probe does not work properly under our conditions.

**Suggested work:**

1. Determination of the gas temperature of inductively coupled hydrogen plasma discharge by the UV light using the TALIF spectroscopy.

2. Checking with different aspect ratio the radial homogeneity of RF discharges.

3. Determination of the electron temperature in inductive discharges using many lines, in order to decrease errors in the two line method.

4. Improvement of the advanced two gas actinometry method taking into account the difference in threshold energies (about 1.8 eV) in the cross section of the dissociative excitation of the $H_\beta$ line ($E_{th}$=17.2 eV) and the corresponding Ne $^2p_1$ actinometer line ($E_{th}$=19 eV). This improvement can be done by calculation of the excitation function of both species and actinometer in the missing energy range.

5. The electron energy distribution function is the most important plasma parameter, which can be determined spectroscopically using inert gases like He, Ne, Kr and Ar. The determination of the EEDF is another research topic in inductive discharges.

## Acknowledgements

I would like to express my gratitude to all the people who, have helped me during the period of this work.

First of all I am indebted to my Prof. Dr. H F Döbele for giving me the opportunity to do my Ph.D. under his supervision. Thanks for very kind care and support during the whole period of my research. My deepest appreciation to Dr. V Schulz von-der Gathen, for his help, valuable guidance and continuous supervision during this research. Although, he has lots of work to do, he find always time for discussion and improving my experimental and programming skills. My great thanks and respect to Dr. K Niemi for his valuable suggestions during the experimental work and during writing the thesis. I am grateful to Dr. T Gans (University of Bochum) for his help and encouragement during the first period of my work and for his helpful discussions especially in the degree of dissociation measurements. Thanks to Dipl. Phys. D Lacombe for his help in particularly during the TALIF measurements. Many thanks for Mr. J Leistikow and Mrs. C Fischer for their encouragement and for technical support during the progress of my work. In addition I would like to thank all other members of our work-group Dr. H.-M Katsch, Dr. T Mosbach, Dipl. Phys. S Reuter, Dipl. Phys. C Manthey, Dipl. Phys. A Wagner, Mrs. I Langner, and Mrs. Cl Besecke for their care and help.

Furthermore, I would like to thank my friends in Egypt and here in Germany, in particular Mr. G Abo-Elkasem and M.Sc. A El-Kamhawy for their help and support. I wish to acknowledge my father, my mother and all my sisters and brothers for their support and praying. My special thanks to my wife and my children Abdel-Rahman and Hazim for their patience, love and support during this work. Finally my great thanks to the Egyptian mission department for financial support during this work.

# Bibliography


[1] A Bogaerts, E Neyts, Renaat Gijbels and J van der Mullen; Spectrochimica Acta Part B 57 (2002) 609

[2] J R Roth; "Industrial Plasma Engineering" Volume 1 : principles (IOP Publishing Ltd 1995)

[3] A Grill; "Cold Plasmas in Materials Fabrication: From Fundamentals to Applications" (New York: IEEE PRESS 1994)

[4] R Hippler, S Pfau, M Schmidt, K H Schoenbach (Eds.); "Low Temperature Plasma Physics" (WILEY-VCH Verlag Berlin GmbH 2001)

[5] M B Hopkins and J F Lawler; Plasma Phys. Control. Fusion, 42 (2000) B189

[6] V Schulz-von der Gathen and H F Döbele; Plasma Chemistry and Plasma Processing 16 (4) (1996) 461

[7] M A Lieberman and A J Lichtenberg; "Principles of Plasma Discharges and Material Processing" (New York: Wiley 1994)

[8] W G Graham; Plasma Sources Sci. Technol. 4 (1995) 281

[9] L Schlapbach, A Züttel, P Gröning, O Gröning and P Aebi; Appl. Phys. A72 (2001) 245

[10] A Rousseau, A Granier, G Gousset and P Leprince; J. Phys. D: Appl. Phys. 27 (1994) 1412

[11] T Gans, V Schulz-von der Gathen and H F Döebele; Plasma Sources Sci. Technol. 10 (2001) 17

[12] B Chapman; "Glow Discharge Processes" (JOHN WILEY & SONS 1980)

[13] J T Gudmundsson; Ph.D. Thesis, University of California at Berkeley 1996

[14] H Conrads and M Schmidt; Plasma Sources Sci. Technol. 9 (2000) 441

[15] Yu P Raizer; Gas Discharge Physics (Berlin: Springer 1991)

[16] T Gans; Ph.D. Thesis, University of Essen 2001

[17] R N Franklin; J. Phys. D: Appl. Phys. 36 (2003) R309

[18] K-U Riemann; J. Phys. D: Appl. Phys. 24 (1991) 493

[19] E C Benck, A Schwabedissen, A Gates, and J R Roberts; J. Vac. Sci. Technol. A 16 (1) (1998) 306

[20] V A Godyak, R B Piejak and B M Alexandrovich; Plasma Sources Sci. Technol. 3 (1994) 169

[21] J Hopwood, C R Guarnier, S J Whitehair and J J Cuomo; J. Vac. Sci. Technol. A 11 (1993) 152

[22] E Amanatides and D Mataras; J. Appl. Phys 89(3) (2001) 1556

[23] S-H Seo, C-W Chung, J-I Hong and H-Y Chang; Phys. Rev. E 62 (5) (2000) 7155

[24] J Hopwood; Plasma Sources Sci. Technol. 1 (1992) 109

[25] M H Khater and L J Overzet; Plasma Sources Sci. Technol. 9 (2000) 545

[26] G K Vinogradov; Plasma Sources Sci. Technol. 9 (2000) 400

[27] J H Keller; Plasma Sources Sci. Technol. 5 (1996) 166

[28] V I Kolobov and D J Economou; Plasma Sources Sci. Technol. 6 (1997) 1

[29] I M El-Fayoumi and I R Jones; Plasma Sources Sci. Technol. 7 (1998) 179

[30] I M El-Fayoumi and I R Jones; Plasma Sources Sci. Technol. 6 (1997) 201

[31] R B Piejak, V A Godyak and B M Alexandrovich; Plasma Sources Sci. Technol. 1 (1992) 179

[32] M J Cooke and G Hassall; Plasma Sources Sci. Technol. 11 (2002) A74

[33] M M Turner; Plasma Sources Sci.Technol. 5 (1996) 159

[34] M M Turner; Phys. Rev. Lett. 71 (1993) 1844

[35] J T Gudmundsson and M A Lieberman; Plasma Sources Sci. Technol. 7 (1998) 83

[36] B Ramamurthi, D J Economou and I D Kaganovich; Plasma Sources Sci. Technol. 12 (2003) 170

[37] J Boeuf and A Merad; Plasma Processing of Semiconductors, Kluwer Academic Publishers, (1997) 291

[38] V A Godyak, R B Piejak and B M Alexandrovich; Phys. Rev. Lett. 80 (1998) 3264

[39] ChinWook Chung, S S Kim, and H Y Chang; Phys. Rev. Lett. 88 (9) (2002) 1

[40] N S Yoon, S S Kim, C S Chang, and D I Choi; Phys. Rev. E 54 (1996) 757

[41] C E Goedde, A J Lichtenberg, M A Liebermann; J. Appl. Phys. 64 (1988) 4375

[42] G Gozadinos, D Vender, MM Turner and M A Lieberman; Plasma Sources Sci. Technol. 10 (2001) 117

[43] A O'Keefe, J J Scherer, A L Cooksy, R Sheeks, J Heath, R J Saykally; Chem. Phys. Lett. 172 (1990) 214

[44] G Berden, R Peeters and G Meijer; Int. Reviews in Physical Chemistry 19 (4) (2000) 565

[45] M J van de Sande and J J A M van der Mullen; J. Phys. D: Appl. Phys. 35 (2002) 1381

[46] M J van de Sande R H M Deckers, F Lepkojus, W Buscher and J J A M van der Mullen; Plasma Sources Sci. Technol. 11 (2002) 466

[47] G Faure and S M Shkol'nik; J. Phys. D: Appl. Phys. 31 (1998) 1212

[48] K Behringer and U Fantz; New Journal of Physics 2 (2000) 23.1

[49] Th Welzel, I Dani and F Richter Plasma Sources Sci. Technol. 11 (2002) 351

[50] R Petit, "Electromagnetic theory of gratings" (Springer-Verlag, New York 1980)

[51] PicoStar HR Operation Manual; Copyright 1996 by LaVision

[52] H Hutchinson; "Principles of plasma diagnostics" (Cambridge University Press 1987)

[53] G Hernandez; Fabry-Perot Interferometers (Cambridge: Cambridge University Press 1986)

[54] J M Vaughan; "The Fabry-Perot Interferometer: History, Theory, Practice and Applications" (Bristol: Institute of Physics 1989)

[55] R S Longhurst; "Geometrical and Physical Optics" (Orient Longman, third edition 1973)

[56] G Vorlaufer, J Laimer and H Störi; Meas. Sci. Technol. 11 (2000) 1179

[57] J T Gudmundsson; "On smoothing of the I-V Langmuir probe characteristic" (Memorandum No. UCB/ERL M97/38, 3 June 1997)

[58] H M Mott-Smith and I Langmuir; Phys. Rev. 28 (1926) 727

[59] J G Laframboise; "theory of spherical and cylinderical Langmuir probes in a collisionless, Maxwellian plasma at rest" (UTIAS Report No. 100, University of Toronto 1966)

[60] Smart Probe; "Installation and Software Manual" (Scientific Systems Ltd. 1997)

[61] M J Druyvesteyn; Zeitschrift für Physik 64 (1930) 781

[62] J Amorim, G Baravian, and J Jolly; J. Phys. D: Appl. Phys. 33 (2000) R51

[63] J Amorim, G Baravian, M Touzeau, and J Jolly; J. Appl. Phys. 76 (3) (1994) 1487

[64] K Niemi, V Schulz-von der Gathen and H F Döbele; J. Phys. D: Appl. Phys. 34 (2001) 2330

[65] A Goehlich, T Kawetzki and H F Döbele; J. Chem. Phys. 108 (1998) 9362

[66] F Debal, M Wautelet, J P Dauchot and M Hecq; Meas. Sci. Technol. 8 (1997) 618

[67] K T Walsh, J Fielding, and M B. Long; Optics Letters 25 (7) (2000) 457

[68] E Keren, E Bar-Ziv, I Glatt and O Kafri; Appl. Opt. 20 (1981) 4264

[69] M W Blades; Appl. Spectrosc. 37 (4) (1983) 371

[70] M Hipp and P Reiterer; User Manual for IDEA 1.5 (Software for Interferometrical Data Evaluation) September (1999) 58

[71] G Pretzler; Z. Naturforsch. 46a (1991) 639

[72] G Pretzler, H Jäger, T Neger, H Philipp and J Woisetschläger; Z. Naturforsch. 47a (1992) 955

[73] C S Corr, P G Steem and W G Graham; Plasma Sources Sci. Technol. 12 (2003) 265

[74] I M El-Fayoumi, I R Jones and MM Turner; J. Phys. D: Appl. Phys. 31 (1998) 3082

[75] G Cunge, B Crowley, D Vender and MM Turner; Plasma Sources Sci. Technol. 8 (1999) 576

[76] K Suzuki, K Nakamura, H Ohkubo and H Sugai; Plasma Sources Sci. Technol. 7 (1998) 13

[77] U Kortshagen, N D Gibson and J E Lawler; J.Phys. D: Appl. Phys. 29 (1996) 1224

[78] Y Miyoshi, Zoran Lj Petrovic' and Toshiaki Makabe; J. Phys. D: Appl. Phys. 35 (2002) 454

[79] K Suzuki, K Konishi, K Nakamura and H Sugai; Plasma Sources Sci. Technol. 9 (2000) 199

[80] T Gans, Chun C Lin, V Schulz-von der Gathen and H F Döbele; J. Phys. D: Appl. Phys. 34 (2001) L39

[81] K Behringer and U Fantz; J. Phys. D: Appl. Phys. 27 (1994) 2128

[82] M M Turner and M A Lieberman; Plasma Sources Sci. Technol. 8 (1999) 313

[83] M Tuszewski; J. Appl. Phys. 79 (1996) 8967

[84] M A Lieberman, A J Lichtenberg, A M Marakhtanov; Appl. Phys. Lett. 75 (1999) 3617

[85] P Chabert, A J Lichtenberg, M A Lieberman and A M Marakhtanov; Plasma Sources Sci. Technol. 10 (2001) 478

[86] R A Gottscho and T A Miller; Pure Appl. Chem. 56 (1984) 184

[87] H Abada, P Chabert, J P Booth, J Robiche and J Cartry; J. Appl. Phys. 92 (2002) 4223

[88] K Behringer and U Fantz; Contrib. Plasma Phys. 39 (1999) 411

[89] E Surrey and B Crowley; Plasma Phys. Control. Fusion 45 (2003) 1209

[90] A N Goyette, W B Jameson, L W Anderson and J E Lawler; J. Phys. D: Appl. Phys. 29 (1996) 1197

[91] B P Lavrov; Opt. Spectrosc. 48 (1980) 375

[92] A Chelouah, E Marode, G Hartmann and S Achat; J. Phys. D: Appl. Phys. 27 (1994) 940

[93] O Motret, C Hibert, S Pellerin and J M Pouvesle; J. Phys. D: Appl. Phys. 33 (2000) 1493

[94] S Stamou, D Mataras and D Rapakoulias; J. Phys. D: Appl. Phys. 31 (1998) 2513

[95] S A Astashkevich, M Käning, E Käning, N V Kokina, B P Lavrov, A Ohl and J Röpcke; J. Quant. Spectrosc. Radiat. Transfer 56 (5) (1996) 725

[96] U Fantz; Contrib. Plasma Phys. 42 (2002) 675

[97] B P Lavrov, V N Ostrovsky and V I Ustimov; Sov. Tech. Phys. 50 (1980) 2072

[98] G Herzberg; "Spectra of Diatomic Molecules" (D. Van Nostrand Company, Princeton, New Jersey 1950)

[99] B P Lavrov and M V Tyutchev; Acta Phys. Hung. 55 (1984) 411

[100] B P Lavrov, V N Ostrovsky and V I Ustimov; J. Phys. B: At. Mol. Phys. 14 (1981) 4389

[101] T Gans, V Schulz-von der Gathen and H F Döbele; Europhys. Lett. 66 (2004) 232

[102] P Scheubert, U Fantz, P Awakowicz and H Paulin; J. Appl. Phys. 90 ( 2) (2001) 587

[103] J W Coburn and M Chen; J. Appl. Phys. 51 (1980) 3134

[104] S Manolache, M Sarfaty and F Denes; Plasma Sources Sci. Technol. 9 (2000) 37

[105] D Pagnon, J Amorim, J Nahorny, M Touzeau and M Vialle; J. Phys. D: Appl. Phys. 28 (1995) 1856

[106] A Gicquel, M Chenevier, Kh Hassouni, A Tserepi and M Dubus; J. Appl. Phys. 83 (12) (1998) 7504

[107] J C Thomaz, J Amorim and C F Souza; J. Phys. D: Appl. Phys. 32 (1999) 3208

[108] W Biel, M Bröse, M David, H Kempkens and J Uhlenbusch; Plasma Phys. Control. Fusion 39 (1997) 661

[109] J D Walker Jr and R M St John; J. Chem. Phys. 61 (1974) 2394

[110] G R Möhlmann and F J DeHeer and J Los; Chem. Phys. 25 (1977) 103

[111] J E Chilton, M D Stewart Jr and C C Lin; Phys. Rev. A 62 (2000) 32714

[112] J E Chilton, M D Stewart Jr and C C Lin; Phys. Rev. A 61 (2000) 52708

[113] M L Burshtein, B P Lavrov and V N Yakovlev; Opt. Spektrosk. 62 (1987) 729

[114] NIST atomic spectra database http://physlab.nist.gov/cgi-bin/AtData/main_asd

[115] K Niemi; Ph.D. Thesis, University of Essen 2003

[116] M V Malyshev and V M Donnelly; Phys. Rev. E 60 (5) (1999) 6016

[117] NCM Fuller, M V Malyshev, V M Donnelly and Irving P Herman; Plasma Sources Sci. Technol. 9 (2000) 116

[118] NCM Fuller, V M Donnelly and I P Herman; J. Vac. Sci. Technol. A 20 (1) (2002) 170

[119] V M Donnelly, M J Schabel; J. Appl. Phys. 91 (10) (2002) 6288

[120] V M Donnelly, M V Malyshev, M J Schabel, A Kornblit, W Tai, I P Herman and NCM Fuller; Plasma Sources Sci. Technol. 11 (2002) A26